Discovery of Giant Gamma-ray Bubbles in the Milky Way

Thesis Advisor: Professor Douglas P. Finkbeiner Meng Su

Discovery of Giant Gamma-ray Bubbles in the Milky Way

Abstract

Based on data from the *Fermi Gamma-ray Space Telescope*, we have discovered two gigantic gamma-ray emitting bubble structures in our Milky Way (known as the *Fermi* bubbles), extending ∼50 degrees above and below the Galactic center with a width of ∼40 degrees in longitude. The gamma-ray emission associated with these bubbles has a significantly harder spectrum ($dN/dE \sim E^{-2}$) than the inverse Compton emission from known cosmic ray electrons in the Galactic disk, or the gamma-rays produced by decay of pions from proton-ISM collisions. There is no significant difference in the spectrum or gamma-ray luminosity between the north and south bubbles. The bubbles are spatially correlated with the hard-spectrum microwave excess known as the *WMAP* haze; we also found features in the *ROSAT* soft X-ray maps at $1.5 - 2$ keV which line up with the edges of the bubbles. The *Fermi* bubbles are most likely created by some large episode of energy injection in the Galactic center, such as past accretion events onto the central massive black hole, or a nuclear starburst in the last $\sim$ 10 Myr. Study of the origin and evolution of the bubbles has the potential to improve our understanding of recent energetic events in the inner Galaxy and cosmic ray acceleration mechanisms. Furthermore, we have recently identified a gamma-ray cocoon feature within the southern bubble, with a jet-like feature along the cocoon's axis of symmetry, and another directly opposite the Galactic center in the north. If confirmed, these jets are the first resolved gamma-ray jets ever seen.

Contents

Acknowledgments

First and foremost it is a great pleasure to thank my advisor, Douglas P. Finkbeiner, for his constant flow of ideas, support, encouragement, and all the guidance in the past couple of years. I have been thinking for a while what I should put in the acknowledgement about Doug; it turned out to be the most difficult part of this whole thesis. His sense of smell on interesting problems and ideas of both physics and astronomy, and his incredible breadth of knowledge on science and the rest of the world constantly impresses and inspires me. I have greatly benefited from his programming skill, insightful blackboard calculation, and deep understanding from particle physics to instruments and various statistical analysis. I could not forget we sat together at his home one day from the early afternoon until 3 a.m. to finish up the final modification of the discovery paper of the Fermi bubbles. He and his wife Erin invited me to their house several times for gathering and treated me with delicious food.

Doug's excellent research group has a range of diverse lines of research. I have constantly been inspired by discussing physics with other fellow group members including Greg Green, Tongyan Lin, Ann Mao, Aaron Meisner, Eddie Schlafly, Tracy Slatyer, Molly Swanson, and Mario Juric. Special thanks go to Tracy for our delightful collaboration and countless insightful discussion on astrophysics and particle physics.

It's my pleasure being at Harvard for the past five years. It was amazing experience for me. I was very lucky to have Matias Zaldarriaga as my advisor in the first two years at Harvard. He introduced me to the field of gravitational lensing

of CMB. The broad range of physics, techniques and skills I learned from the first project with him guided me towards a couple of independent following projects including non-Gaussianity of CMB, patchy reionization, and parity violation in the early universe. I'd also like to thank John Kovac, working on the BICEP experiment with him is one of the biggest challenge and most exciting experience for me. I have learned so much about CMB experiment and data analysis in depth from him over these years. I would also like to thank the whole Harvard CMB group for bringing my life so close to the South Pole!

I would like to thank Paolo Coppi, Josh Grindlay, Christine Jones, and Aneta Siemiginowska for kindly being my thesis defense committee, and Avi Loeb for being my TAC member. I also want to thank my research exam committee Josh Grindlay, Lars Hernquist, and and Matias Zaldarriaga. Special thanks go to Josh who was my academic supervisor when I first came to Harvard, and after then he has been on all my committee throughout my life at Harvard. Without professional help and advice from Aneta, neither of our XMM-Newton proposal nor my job applications would have been successful.

I also want to thank many of the faculty including Charles Alcock, Dave Charbonneau, Daniel Eisenstein, Lars Hernquist, Avi Loeb, Jim Moran, Ramesh Narayan, Dimitar Sasselov, and Irwin Shapiro for always trying to improve the department and for their care and support of the students, not limited to academic life. I really enjoyed being the TA for Robert Kirshner's amazing class, I've been astonished by all kinds of demonstrations he was able to do in class. Thanks to Edo Berger, Alicia Soderberg, and all the past Graduate Student Forum organizers, Tuesday afternoon had became the happy hour for all of us to chat about science

and enjoy beer!

I would like to thank Amit Yadav, I had learned a lot from our close collaboration. Our constant discussion/debate over the phone after you moved to IAS was the reason I switched my cell phone company from Verizon to AT&T. I hope your next marathon is coming soon!

After more than twenty conferences and workshops I have attended, I started to feel as a member of the astronomy community. Thanks all the colleagues I have met and communicated – it's impossible to write all their names here. Special thanks go to Andy Strong for his insightful discussion about gamma-ray diffuse emission and the generous support on my job application. In particular, I want to thank Bruce Winstein; I first met him during a conference in Beijing. He encouraged and supported me to pursue PhD study in US. Sadly he is no longer with us, but the book he mailed to me all the way to China about Enrico Fermi will be my most valuable treasure on my bookshelf forever.

For my past officemates Li Zeng, Sumin Tang, Heng Hao, Roman Shcherbakov, and my basketball fellows at CfA Lijun Gou, Junfeng Wang, Zhiyuan Li, Yue Shen, without them my life at Harvard would not have been the same. I would like to thank my fellow Astronomy graduate students for the supportive and friendly community they foster – please forgive my constant distraction! I especially want to thank Gurtina Besla, Claude-André Faucher-Giguère, Matt McQuinn, and Chris Hayward. We first met in a conference in Melbourne, from them I saw how happy Harvard astronomy students are and they encouraged me to apply to Harvard!

I can not imagine that anyone could graduate without the hard work of Jean,

Peg, and Donna. They are bureaucratic magicians; they made all the paperwork and hassle just disappear. More importantly, they made every day better than the last and were always so welcoming. I will miss them.

CfA, particularly the Institute for Theory and Computation (ITC) is such a fantastic place, I enjoyed the schedule here with several talks/events per day, just like delicious dinner menu you can freely choose from – I could not count how many tons of free pizza/sandwiches I have eaten during the years. I have really enjoyed many stimulating conversations with postdocs and faculty members.

Much of my thesis relies on the hard work of the greater astronomical community. I want to especially thank the Fermi-LAT collaboration for publicly releasing their data to the entire community. I could not imaging without arXiv and ADS, how my work could ever be done. Checking arXiv update everyday might be the only good habit that I have kept for longer than eight years.

I want to thank my many important science mentors I have had throughout my life: Zuhui Fan for mentoring me in my first couple of real research projects and her trust and support on my dream of pursuing science, Xuelei Chen for being a great advisor, a closed friend, and my primary motivation to visit National Astronomical Observatory of China weekly for his group meeting. Special thanks go to my first cosmology course lecturer Yunqiang Yu, I took his last lectures before retirement in my last year of high school (I had to sneak into Peking University for his lecture!). I still keep telling my friends how much I loved those classes and how lucky I was. I wish I had a video recorder back to 2002. Canbin Liang not only taught me GR, but also showed me what a great teacher is. I would never forget the lecture just one

day after his wife passed away. I could feel his deep sadness mixed with the greatest enthusiasm on science he was eager to deliver to us.

Among many great teachers, Mrs. Hua Han made sigfinicant influence to my early life, her constant care on my study, life, and happiness greatly remedied the year-long period while my parents were not with me. Mrs. Jianli Yu encouraged me to compete on the Chinese National Physics Olympics during high school, the success of which brought me to Peking University without struggling on the tedious college entrance exam in China.

For all my old friends pursuing science, without them I can't believe how lonely I would be in my life. For my old PKU physics friends Yiqiao Tang and Qimin Quan, our quasi-weekly gathering is one of the most important events in my grad school. Without Qimin's regular enthusiasm on delicious food after mid-night, my cooking skill and creativity would not be so inspired and diverse. I have no doubt I wouldn't be here today without the support of Weixue Wang – I'd probably be studying math instead. Our life-long friendship will last forever. My special words are dedicated to my college mate Xiabin Sun: his impact on me will last forever – since he taught me how to use Google. Although he left this world four years ago, his belief in science would be my eternal power to pursue science, not just for what we have said and what we have dreamed. Even in his last days fighting with cancer, he was reading papers about quantum information and cosmology. I will never forget his last words to me: I would like to leave something about science to this world. He made me feel that science is our destiny, is the home of our soul.

Finally, I want to thank my parents for all of the love and support they have

given me. I'm the only child for my parents, my happiness and successful growth seems the only thing what can make them truly happy. I hope they can be proud of me even I'm not (and probably won't be) very rich to enjoy certain kind of life that many young people in my generation are dreaming for. My father taught me that the way to enjoy science is the way to enjoy life, you are not targeting a product, the reason to try and learn is simply following the your heart, your desire and the nature of human beings – the curiosity. My mother is my model of personality and character, she taught me to love this world, and I will forever love her. Astronomy makes me love the university, my parents make me love the world. Also, I want to save a few words for my wife Yuqi Qin. Meeting her at Harvard is another gift this amazing university brought to my life. Getting married with her is worth another degree to celebrate, although the story between us probably needs more than a PhD thesis to write. And the story will not never end.

For My Mom Aimei Wang

and My Dad Chunsheng Su

Preface

Simplicity - the root of the substance. The fundamental law underlying everything in the universe is utterly plain and simple, no matter how abstruse or complex some things may appear to be.

Variability - the use of the substance. Everything in the universe is continually changing. By comprehending this one may realize the importance of flexibility in life and may thus cultivate the proper attitude for dealing with a multiplicity of diverse situations.

Persistency - the essence of the substance. While everything in the universe seems to be changing, among the changing tides there is a persistent principle, a central rule, which does not vary with space and time.

–I Ching (The Book of Change), 3rd to the 2nd millennium BC [1]

The first chapter of this thesis provides a brief summary of the evidence of past activity towards the inner Galaxy and the motivation of this thesis work. This chapter is by no means intended to be a comprehensive treatise on either diffuse gamma-ray emission or the *Fermi* Gamma-ray Space Telescope. The whole task of reviewing Galactic gamma-ray emission and the decades of study of the Galactic center is beyond the scope of a 200 some page dissertation. Chapter 2 describes in detail our data analysis pipeline and the revealed *Fermi* bubble properties based on the discovery paper Su et al. (2010). Chapter 2.1 attempts to provide an introduction to the *Fermi*-LAT and detailed procedure of our data analysis. Specialists on *Fermi* data analysis are advised to skip Chapter 2.1. Chapter 2.2 describes generic properties we found about *Fermi* bubbles , along with necessary

[1] Zheng Xuan, Commentary on I Ching, Eastern Han Dynasty.

background for readers to be able to follow the other chapters. In the third chapter, we compare the gamma-ray bubbles with large scale features at other wavelengths, particularly in X-ray and microwave. Proposed models and explanations of the *Fermi* bubbles , along with discussions on related topics are provided in Chapter 4. Chapter 5 describes the evidence for a pair of kpc-scale Galactic gamma-ray jets recently revealed in the three year *Fermi* data. In Chapter 6, we revisit detailed properties of the *Fermi* bubbles based on a factor of two longer exposure time of *Fermi* on the bubbles, along with improved analysis techniques. And finally we conclude in Chapter 7.

During my graduate studies here at Harvard, I also did some cosmology work (Su et al. 2009; Yadav et al. 2009; Su et al. 2011a,b; Yadav et al. 2010), and my continued work on BICEP – the first CMB experiment dedicated for searching primordial gravitational wave by measuring large scale B-mode polarization. These projects will not be discussed in this thesis.

Finally, a quote from Wayne Hu's thesis "Wander through its pages and perhaps you will find it of some use – if nothing else, for its soporific qualities.".

Meng Su

Harvard, Cambridge

April 2012

Chapter 1

Introduction

Galactic diffuse gamma-ray emission, as the brightest component of the high energy gamma-ray sky, is predominantly produced by interactions of cosmic ray (CR) protons with interstellar gas, and CR electrons inverse-Compton (IC) scattering on the interstellar radiation field (ISRF) and interactions with the ambient ionized gas (bremsstrahlung or free-free emission). Diffuse Galactic gamma-ray emission can be used to study CR origin and propagation in the Milky Way, which is complementary to radio surveys probing e^- CR synchrotron radiation in the presence of the Galactic magnetic field, and the direct measurements of CRs by balloons and satellites. Particularly, the revealed spatial and spectral distribution of Galactic CRs can be used to reveal past energetic processes in the Milky Way.

On the other hand, the inner Milky Way is home to a supermassive black hole (SMBH) - Sgr A*, with mass $\simeq 4 \times 10^6 \mathrm{M}_\odot$ (Schödel et al. 2002; Ghez et al. 2005, 2008). The central SMBH is surrounded by clusters of young stars and giant molecular clouds (see e.g. Morris & Serabyn 1996, for a review). The nuclear star

cluster has a half-light radius of $\sim$ 5pc. Although there are indications of past activity towards the inner Galaxy and the Soltan relation (Soltan 1982) implies that Sgr A*, as other SMBHs in the center of galaxies, gained most of its mass through luminous accretion, it is currently very dim in comparison with similar typical active galactic nucleus (AGN): its X-ray luminosity is less than $\sim 10^{-11} L_{\rm Edd}$ (where $L_{\rm Edd} \sim$ a few $\times 10^{44}$ erg s^{-1} is its Eddington luminosity) (see e.g. Baganoff et al. 2003). The unusual dimness of Sgr A* has stimulated development of radiatively inefficient accretion and accretion/outflow solutions (e.g., Narayan & Yi 1994; Narayan et al. 1995; Yuan et al. 2002, 2003).

However, Fe Kα X-ray reflection echoes from molecular clouds around Sgr A* have been understood as relics of past activity, which suggest that Sgr A* might have been much brighter with a luminosity of a few $\times 10^{39}$ erg s^{-1} in the past few hundred years (Sunyaev et al. 1993; Koyama et al. 1996; Revnivtsev et al. 2004; Ponti et al. 2010). The variability of X-ray reflection nebulae may reflect accretion events from a few pc-scale molecular gas reservoirs (Morris et al. 1999) or the wind capture rate from the young massive stars near Sgr A* that feed it presently (Cuadra et al. 2008). On a longer timescale, one might expect relics of past activity in high energy CRs and hot gas, perhaps far off the disk. The most obvious observable would be e^- CR (visible in inverse Compton gamma-ray and microwave synchrotron emission) and thermal emission (X-rays).

This thesis describes the discovery of a pair of newly revealed gigantic bubble structures from the diffuse gamma-ray emission in the Milky Way and its implications for the past activity towards the inner Galaxy. In this Chapter of introduction, we begin with a review on high energy Galactic diffuse emission and evidence of past

energetic events in the Milky Way.

1.1 Observations of Galactic Diffuse Emission at High Energy

Observations of diffuse gamma-ray emission go back decades to the first gamma-ray detection from the inner Galaxy by the OSO-3 satellite (Kraushaar et al. 1972). The follow-up breakthrough came with the inner Galaxy observation at $E \lesssim 1$ GeV from *COS-B* (Bignami et al. 1975; Strong 1984; Strong et al. 1987), and *SAS-2* (Fichtel et al. 1975; Kniffen & Fichtel 1981) (see Bloemen 1989, for a review). Later data from the *EGRET* experiment aboard the *Compton Gamma-ray Observatory* extended to the high-energy side of the π^0 bump with the energy range 1 MeV to 10 GeV with higher-quality data covering the entire sky (Smialkowski et al. 1997; Dixon et al. 1998). However, *EGRET* lacked the sensitivity and angular resolution to reveal the detailed structure of gamma-ray emission toward the inner Galaxy. More recently, the SPI instrument aboard the *International Gamma-Ray Astrophysics Laboratory (INTEGRAL)* observatory has extended the observations of soft gamma-ray of CR-induced diffuse emissions into the hard X-ray range (Bouchet et al. 2008, 2011). The *Fermi Gamma-ray Space Telescope* (*Fermi*) launched in 2008 provides greatly improved data up to $\sim 100\,\mathrm{GeV}$, with sufficient angular resolution to map out interesting structures (see Strong et al. 2007, for a recent pre-*Fermi* review of the subject)[1]. The Large Area Telescope (LAT) aboard *Fermi* provides an

[1]See `http://fermi.gsfc.nasa.gov/ssc/data/`

evolutionary view of the full sky in the gamma-ray range of 30 MeV to ∼300 GeV with a sensitivity surpassing *EGRET* by more than an order of magnitude.

1.2 Past Activity Towards the Galactic Center

On the other hand, evidence for past activity towards the inner Galaxy have been found in other wavelength. The *Midcourse Space Experiment* combined with *IRAS* data confirms the existence of a limb-brightened bipolar structure, the so called Galactic center lobe (GCL), with origin at the GC on the *degree* scale (see e.g. Law 2010, for a summary of multiwavelength observations of GCL). The inferred energy injection of both these bipolar structures, despite their different scales, is $\sim 10^{54-55}$ ergs, with an estimated age of $\sim 10^6$ yr for the GCL and $\sim 10^7$ yr for the superwind bubble (SWB). These features are claimed to originate from one or more episodes of rapid energy release. More evidence of past Galactic center activity has been found in X-ray. Fe Kα echoes from molecular clouds around Sgr A* suggest that the accretion rate of the central SMBH had increased by orders of magnitude in the past few hundred years (Sunyaev et al. 1993; Koyama et al. 1996). At lower energies, the *ROSAT* All-Sky Survey at 1.5 keV (Snowden et al. 1997) revealed a biconical X-ray structure over the inner tens of degrees around the Galactic center (GC), later interpreted as a SWB with energetics of the order of 10^{54-55} ergs (Sofue 2000a; Bland-Hawthorn & Cohen 2003a).

1.3 Microwave Excess: the *WMAP* Haze

Beyond direct evidence of shell structures, microwave observations provide intriguing indications of energy release toward the GC.

At tens of GHz, the *Wilkinson Microwave Anisotropy Probe* (*WMAP*) [2] provides sensitive degree resolution full sky maps of diffuse microwave emission. By subtracting templates including Galactic Hα, Haslam 408 MHz soft synchrotron, and thermal dust emission to remove the different known emission mechanisms in these maps, a microwave residual excess (named "the microwave haze") with spherical (non-disklike) morphology about ~ 4 kpc in radius toward the GC (visible up to at least $|b| \approx 30°$) has been recognized (Finkbeiner 2004a). It has a spectrum of about $I_\nu \sim \nu^{-0.5}$, harder than typical synchrotron, but softer than free-free. The microwave haze was later interpreted as synchrotron emission from a hard spectrum of e^- CRs. Other hypotheses such as free-free, spinning dust, or thermal dust have failed to explain its morphology, spectrum, or both (Finkbeiner 2004b; Dobler & Finkbeiner 2008). In this thesis, we will assume the emission mechanism of *WMAP* microwave haze is synchrotron and consider the implications.

1.4 A Hard Electron CR Spectrum

A simple model, in which the electron CRs that form the haze have diffused from supernova shocks in the disk, cannot fully explain the data for standard diffusion

[2] `http://map.gsfc.nasa.gov/`

assumptions. The $23 - 33$ GHz spectrum of the haze synchrotron is as hard as that generated from shocks, and it seems extremely unlikely that these electrons can diffuse several kpc from the disk without significant softening of the spectrum. The synchrotron cooling timescale for cosmic ray electrons emitting at frequency ν is $\tau_{\rm syn} \approx 10^6 \; B_{100}^{-3/2} \, \nu_{\rm GHz}^{-1/2}$ yr, where $B_{100} = B/100\mu G$ (Thompson et al. 2006). Besides the hard spectrum, it is difficult to form the distinctly non-disklike morphology of the haze with any population of sources concentrated in the disk (as is believed to be true of supernovae).

The presence of a distinct component of diffuse hard e^- CR far off the plane is intriguing in itself, and has motivated proposals where the haze is generated by pulsars, other astrophysical processes, or the annihilation of dark matter (Hooper et al. 2007; Cholis et al. 2009a; Zhang et al. 2009; Harding & Abazajian 2010; Kaplinghat et al. 2009; McQuinn & Zaldarriaga 2010; Malyshev et al. 2010). Other indications of excess electronic activity in the Milky Way may be found in recent measurements of local electron and positron CRs. The *ATIC*, *Fermi* and *H.E.S.S* experiments have observed a hardening in the $e^+ + e^-$ spectrum at $20 - 1000$ GeV (Chang et al. 2008; Aharonian et al. 2009; Abdo et al. 2009b), with an apparent steepening at ~ 1 TeV, and the PAMELA experiment has measured a rising positron fraction above 10 GeV. Taken together, these measurements imply a new source of hard electrons and positrons, which may be related to the *WMAP* haze. The coexistence of *ROSAT* X-ray bipolar features and the *WMAP* haze toward the inner Galaxy also suggests the interesting possibility of a common physical origin for these signals.

1.5 Inverse Compton Excess from *Fermi*-LAT

Fortunately, if the *WMAP* haze is synchrotron radiation from a hard electron population located around the GC, the same CRs would also produce IC scattered gammas, allowing an independent probe of the CR population. IC photons provide valuable complementary information about the spatial distribution of the e^- CR (given a model for the ISRF), which in turn can constrain hypotheses about their origin. The unprecedented angular resolution and sensitivity of *Fermi*-LAT allows us to probe the gamma-ray counterpart to the microwave haze in detail for the first time.

In this thesis, we show that the *Fermi*-LAT sky maps constructed from 1.6 yr data (600 days) reveal two large gamma-ray lobes, extending 50 degrees above and below the GC, with a width of about 40 degrees in longitude. These two bubble-like structures (named *Fermi* bubbles) have relatively sharp edges and are symmetric with respect to the galactic plane and the minor axis of the galactic disk (instead of a haze-like morphology suggested by Dobler et al. 2010). The gamma-ray signal reveals similar morphology to the *WMAP* haze, and is also suggestive of a common origin with features in the *ROSAT* X-ray maps at 1.5 keV towards the GC.

As we will discuss, the sharp edges, bilobular shape, and apparent centering on the GC of these structures suggest that they were created by some large episode of energy injection in the GC, such as a past accretion onto the central black hole, or a nuclear starburst in the last $\sim$10 Myr. It is well known that the GC hosts a massive black hole and massive clusters of recently formed stars (Paumard et al. 2006). Either of these could potentially provide the necessary energy injection by

driving large-scale galactic winds or producing energetic jets; we will outline some of the advantages and disadvantages of each scenario.

1.6 Structure of This Thesis

In Chapter 2 we briefly review the *Fermi* telescope, particularly the LAT instrument, and our data analysis procedure. We show that the 1.6 yr *Fermi* data maps reveal the *Fermi* bubble features and we show that they are robust when different models for the expected Galactic diffuse emission are subtracted. We characterize the morphology of the bubbles in some detail and employ regression template fitting to reveal a hard, spatially uniform spectrum for the gamma-ray emission associated with the bubbles. In Chapter 3, we show that features in the *ROSAT* soft X-rays and the *WMAP* microwave haze are spatially correlated with the *Fermi* bubbles, and the *WMAP* haze and *Fermi* bubbles are consistent with being produced from the same electron CR population (by synchrotron and IC respectively). Chapter 4 presents possible scenarios to produce the *Fermi* gamma-ray bubbles, the origin of the CRs filling the bubbles and the challenges in explaining the spectral and spatial profiles of the gamma-ray emission from the bubbles. We also discuss the implications of the *Fermi* bubbles for several topics of interest. In Chapter 5, we show a gamma-ray cocoon feature within the southern bubble, with a jet-like feature along the cocoon's axis of symmetry, and another directly opposite the Galactic center in the north. If confirmed, these jets are the first resolved gamma-ray jets ever seen. In Chapter 6, we revisit the *Fermi* bubbles with the three year *Fermi*-LAT data and significantly improved analysis techniques. Chapter 7 presents the discussion and conclusion and

suggest the planned future work.

Chapter 2

Fermi Bubbles in the Milky Way

2.1 Fermi Data and Map Making

The Large Area Telescope (LAT; see Gehrels & Michelson 1999; Atwood et al. 2009; as well as the *Fermi* homepage[1]) is the principal scientific instrument on-board the *Fermi Gamma-ray Space Telescope*, which was launched on 2008 June 11, and starting the nominal mission since 2008 August 4. The LAT is a pair-conversion gamma-ray telescope to distinguish gamma-rays in the energy ranging from 20 MeV to more than 300 GeV. It consists of in total 16 modules of tungsten and silicon-strip trackers (4×4 modular array, 12 layers of 3% radiation length (*Front* or thin section)

[1] `http://fermi.gsfc.nasa.gov/`

Uniform	SFD	bubble	north bubble	south bubble	inner bubble	outer bubble	disk	loop I	$0.5 - 1.0$ GeV - SFD
1.0	0.084	1.0	1.0	1.0	1.0	1.0	0.292	1.0	1.198

Table 2.1: Normalization factors for different templates.

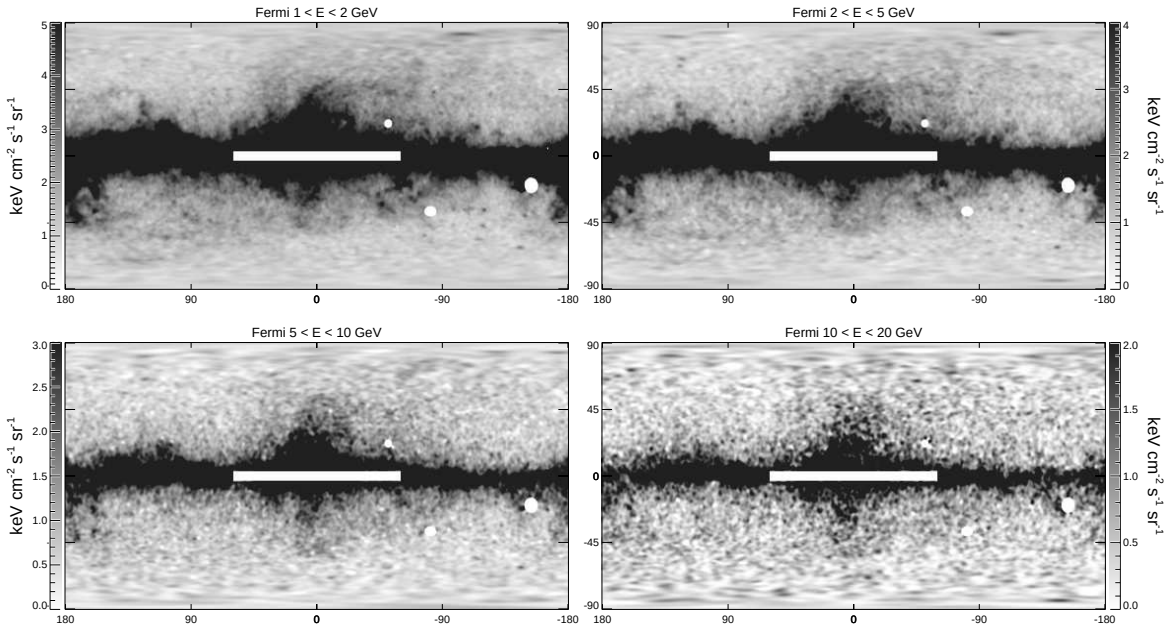

Figure 2.1.— All-sky *Fermi*-LAT 1.6 year maps in 4 energy bins. Point sources have been subtracted, and large sources, including the inner disk ($-2^\circ < b < 2^\circ, -60^\circ < \ell < 60^\circ$), have been masked.

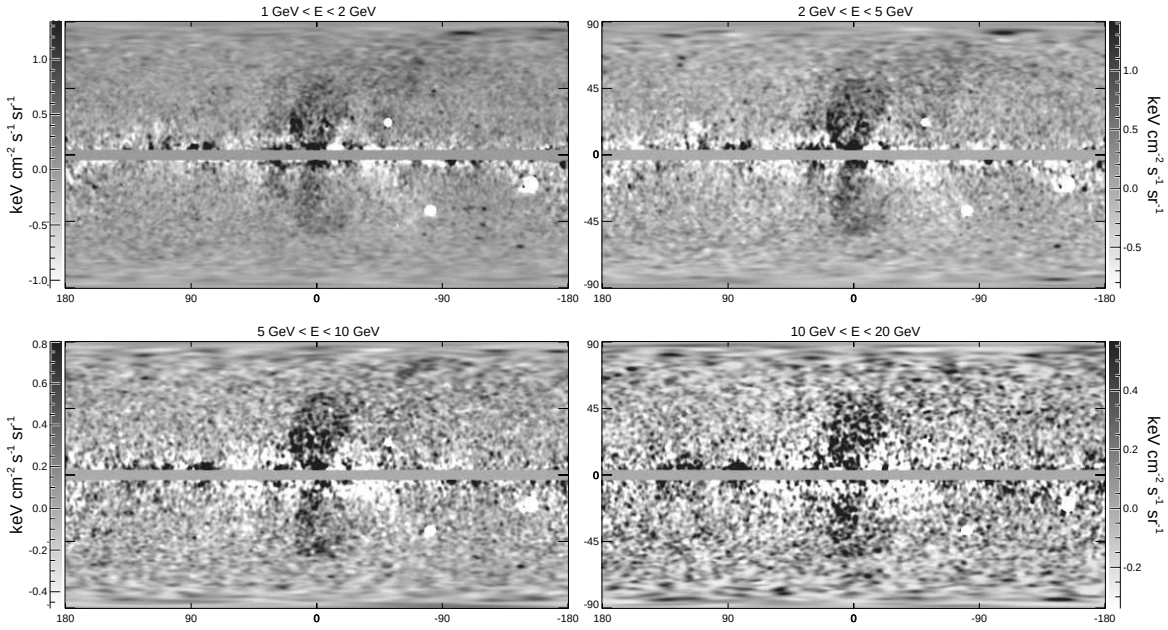

Figure 2.2.— All-sky residual maps after subtracting the *Fermi* diffuse Galactic model from the LAT 1.6 year maps in 4 energy bins (see §2.2.1). Two bubble structures extending to $|b| \sim 50^\circ$ appear above and below the GC, symmetric about the Galactic plane.

on top of 4 layers of 18% radiation length converters (*Back* or thick section)) where high energy gamma rays predominantly convert into electron-positron pairs, and the energy deposition is accurately measured in each crystal to reconstruct the energy of the indicent photon. The tracker/converter system is on top of a calorimeter which contains 96 CsI(Tl) scintillating crystals which are 8.6 radiation lengths deep. LAT is surrounded by an anti-coincidence detector that covers the tracker array to distinguish gamma-rays from intense background of energetic CRs, and a programmable trigger and data acquisition system.

The *Fermi* observatory operates primarily in an all-sky scanning survey mode.

The spacecraft has a low Earth orbit (altitude of 565 km) with an inclination of 25.6°. The LAT provides a wide field-of-view of ∼2.4 sr, a large effective area of ∼6500 cm^2 at 1 GeV, and a point spread function (PSF) about 0.8° for 68% containment at 1 GeV with a variation as a function of energy as $E^{-0.8}$ (asymptoting at $\sim 0.2°$ at high energy). The field of view is so wide that the entire sky may be covered in two orbits by rocking the spacecraft north of zenith on one orbit and south of zenith on the next. Such an observation strategy provides 30 minutes of livetime on each point in the sky every two orbits in only three hours. This scan strategy maximizes observing time while maintaining excellent uniformity. We make use of only events designated "Class 3" (P6_V3 diffuse class) by the LAT pipeline with a zenith angle cut of 105°.

The events are binned into a full sky map using HEALPix, a convenient iso-latitude equal-area full-sky pixelization widely used in the CMB community.[2] Spherical harmonic smoothing is straightforward in this pixelization, and we smooth each map by the appropriate kernel to obtain a Gaussian PSF of 2° FWHM. Because the PSF of the initial map must be smaller than this, at energies below 1 GeV we use only front-converting events (which have a smaller PSF). A larger smoothing scale would help improve S/N, but a relatively small smoothing scale is necessary to see sharp features (such as the bubble edges). Furthermore, for the comparisons and linear combination analysis described in e.g. §2.2.1. it is necessary to smooth the maps at each energy to a common PSF. We generate maps with a smoothing scale

[2]HEALPix software and documentation can be found at `http://healpix.jpl.nasa.gov`, and the IDL routines used in this analysis are available as part of the IDLUTILS product at `http://sdss3data.lbl.gov/software/idlutils`.

with FWHM from $1 - 4^\circ$, and find that a FWHM of 2° works well for our purposes. See Dobler et al. (2010) for details on map construction, smoothing, masking, and for instructions on how to download the maps.

In the discovery paper of *Fermi* bubbles (Su et al. 2010), the gamma-ray maps we used (v2_3) were constructed from about 1.6 year *Fermi* data with greater signal/noise compared to the previously released v1_0 maps. They contain photon events about 606 days or 1.66 years of Fermi-LAT data. We refer to these as the "1.6 year maps." As in Dobler et al. (2010), we construct maps of front-converting and back-converting events separately, smooth to a common PSF, and then combine them. The point source subtraction has improved: instead of interpolating over every source in the 3-month catalog, we use the 1-year catalog,[3] and subtract each point source from the maps in each energy bin, using estimates of the PSF from the *Fermi* science tools.[4] For the 200 brightest and 200 most variable sources, the subtraction is noticeably imperfect, so we interpolate over the core of the PSF after subtracting the best estimate. We take care to expand the mask for very bright sources (Geminga, 3C 454.3, and LAT PSR J1836+5925). The resulting map is appropriate for diffuse work at $|b| > 3^\circ$. At $|b| < 3^\circ$ the maps are severely compromised by the poor subtraction and interpolation over a large number of point sources. Further details of the map processing may be found in Appendix B of Dobler et al. (2010). The v2_3 maps used in this chapter and color versions of the

[3]Available from `http://fermi.gsfc.nasa.gov/ssc/data`

[4]See `http://fermi.gsfc.nasa.gov/ssc/data/analysis/documentation/`

maps are available for download.[5]

2.2 *FERMI* bubbles

2.2.1 Diffuse Galactic Emission Models

At low ($\sim$1 GeV) energies, and close to the Galactic plane, the gamma-rays observed by *Fermi* are dominated by photons from the decay of π^0 particles, produced by the collisions of CR *protons* with ambient ionized gas and dust in the ISM. Collisions of high energy CR *electrons* with the ISM (primarily protons, but also heavier nuclei) produce bremsstrahlung radiation. The *Fermi* all-sky gamma-ray maps in different energy bands are shown in Figure 2.1. In order to uncover the *Fermi* bubble features better, significant π^0 emission, bremsstrahlung, and IC emission from the Galactic disk must be removed. We take three approaches for the foreground removal. One is to use the *Fermi* Diffuse Galactic Model provided by the *Fermi* team[6](§2.2.1). The second approach employs a linear combination of templates of known emission mechanisms (§2.2.1), using existing maps from multiwavelength observations and/or constructed geometric templates. The third approach is taking advantage of the lower energy band $0.5 - 1.0$ GeV *Fermi* map to form a template of a diffuse emission model (§2.2.1).

[5]Available at `http://fermi.skymaps.info`

[6]See `http://fermi.gsfc.nasa.gov/ssc/data/access/lat/BackgroundModels.html`

Fermi Diffuse Galactic Model

The *Fermi* diffuse Galactic model[7] is a comprehensive model of Galactic gamma-ray emission from the ISM, and serves as a background estimate for point source removal. This model is based on template fits to the gamma-ray data, and includes an IC component generated by the `GALPROP` cosmic ray propagation code. `GALPROP` calculates the steady state solution to the diffusion-energy-loss equation, given the 3D gas distribution, interstellar radiation field, B-field model, CR diffusion assumptions, and many other input parameters (Strong & Moskalenko 1999; Strong et al. 2009, 2007). The model is constrained by gamma-ray and microwave observations, locally measured CR spectra, etc. By using a well motivated physical model, one can solve for the spectral and spatial dependence of the injection function, i.e. the e^- and p CR primary source spectra, as a function of position and energy. The diffuse model is the key connection between the input assumptions and the observables, and is essential for interpretation of the *Fermi*-LAT data. It is important to make it as complete as possible.

In this model, the π^0 emission is modeled with maps of interstellar gas: H I from the Leiden/Argentine/Bonn (LAB) Galactic Survey (Kalberla et al. 2005) and CO from the CfA composite CO survey (Dame et al. 2001). Because the π^0 emission is a function of both the gas density and the proton CR density, which varies with Galactocentric radius, it is desirable to allow the emissivity of the gas to vary. Both the H I and CO surveys contain velocity information, which allows separation into six Galactocentric annuli (rings) with boundaries at 4.0, 5.5, 7.0, 10.0, 16.5, and 50

[7]Available from `http://fermi.gsfc.nasa.gov/ssc/data`.

kpc. The spectrum of each is allowed to float, with the constraint that the sum of the rings along each line of sight approximates the observed signal. This freedom also allows for varying amounts of bremsstrahlung (with varying spectrum) which also scales with the ISM density. The contribution from IC is modeled with GALPROP as described above, and included in the ring fit[8].

This procedure provides a diffuse model that faithfully reproduces most of the features of the diffuse Galactic emission. One shortcoming is the existence of "dark gas" (Grenier et al. 2005), clouds with gamma-ray emission that do not appear in the H I and CO surveys. These features are seen in dust maps (Schlegel et al. 1998) and may simply be molecular HI clouds underabundant in CO.

The Fermi diffuse model is primarily intended as a background for point source detection, and comes with a number of caveats. However these caveats apply mainly near the Galactic plane, and at $E > 50\,\mathrm{GeV}$. It is nevertheless useful for qualitatively revealing features in the diffuse emission at high latitude. In Figure 2.2, we show the residual maps after subtracting the *Fermi* diffuse Galactic model in different energy bins. A double-lobed bubble structure is clearly revealed, with similar morphology in the different energy bins. We note that the bubble is neither limb brightened nor centrally brightened, consistent with a flat *projected* intensity distribution.

Simple Template-Based Diffuse Galactic Model

Since the dominant foreground gamma-rays originate from π^0 gammas produced by CR protons interacting with the ISM, the resulting gamma-ray distribution should

[8] http://fermi.gsfc.nasa.gov/ssc/data/access/lat/ring_for_FSSC_final4.pdf

North bubble	South bubble	North arc (outer)	North arc (inner)	Loop I	Donut (outer)	Donut (inner)
(ℓ, b) [deg]	(ℓ, b) [deg]	(ℓ, b) [deg]	(ℓ, b) [deg]	(ℓ, b) [deg]	(ℓ, b) [deg]	(ℓ, b) [deg]
(0.0, 0.0)	(5.5, -5.0)	(28.5, 5.0)	(19.5, 5.0)	(37.5, 25.0)	(31.9, -5.0)	(16.8, -7.6)
(-9.9, 5.0)	(10.7, -10.0)	(31.1, 10.0)	(23.1, 10.0)	(43.2, 30.0)	(34.9, -9.0)	(22.0, -9.4)
(-14.2, 10.0)	(12.9, -15.0)	(31.9, 15.0)	(24.9, 15.0)	(46.3, 35.0)	(37.0, -14.0)	(24.6, -14.0)
(-14.5, 15.0)	(15.0, -20.0)	(34.0, 20.0)	(26.0, 20.0)	(47.7, 40.0)	(36.3, -19.0)	(23.7, -16.5)
(-17.0, 20.0)	(16.3, -25.0)	(34.9, 25.0)	(26.9, 25.0)	(48.9, 45.0)	(33.5, -25.0)	(22.4, -18.7)
(-22.3, 25.0)	(16.0, -30.0)	(33.7, 30.0)	(23.7, 30.0)	(49.8, 50.0)	(28.7, -29.0)	(19.2, -21.2)
(-22.6, 30.0)	(15.5, -35.0)	(32.5, 35.0)	(23.5, 35.0)	(46.6, 60.0)	(11.5, -33.0)	(13.6, -19.3)
(-21.1, 35.0)	(15.0, -40.0)	(30.5, 40.0)	(20.5, 40.0)	(40.6, 65.0)	(4.8, -29.0)	(13.2, -14.3)
(-19.9, 40.0)	(15.0, -45.0)	(27.5, 45.0)	(16.5, 45.0)	(29.4, 70.0)	(-0.4, -20.0)	(13.6, -8.8)
(-13.6, 45.0)	(10.6, -50.0)	(24.7, 50.0)	(11.7, 50.0)	(12.5, 75.0)	(-1.2, -15.0)	(16.8, -7.6)
(-3.0, 50.0)	(3.7, -52.5)	(20.0, 52.5)	(6.0, 52.5)	(-5.0, 78.0)	(0.3, -10.0)	
(1.5, 50.0)	(-6.3, -53.5)	(14.3, 55.0)	(0.0, 55.0)	(-19.0, 78.0)	(5.5, -5.0)	
(8.7, 45.0)	(-13.8, -50.0)			(-33.0, 77.0)		
(12.3, 40.0)	(-21.8, -45.0)			(-49.1, 74.0)		
(15.4, 35.0)	(-25.3, -40.0)			(-61.5, 72.0)		
(17.0, 30.0)	(-26.7, -35.0)			(-69.2, 70.0)		
(18.3, 25.0)	(-26.3, -30.0)			(-75.2, 65.0)		
(18.5, 20.0)	(-25.6, -25.0)			(-77.6, 60.0)		
(18.4, 15.0)	(-23.0, -20.0)			(-78.3, 55.0)		
(16.0, 10.0)	(-18.8, -15.0)			(-77.6, 50.0)		
(12.0, 5.0)	(-13.8, -10.0)			(-75.5, 45.0)		
				(-73.5, 40.0)		
				(-68.3, 35.0)		
				(-67.0, 25.0)		

Table 2.2: Coordinates defining the features shown in Figure 2.4 and Figure 2.7

E range (GeV)	Energy	Uniform	SFD dust	simple disk	whole bubble	simple loop I
$0.3 - 0.5$	0.4	1.681 ± 0.006	1.201 ± 0.011	0.689 ± 0.027	0.035 ± 0.033	0.487 ± 0.015
$0.5 - 0.9$	0.7	1.365 ± 0.007	1.279 ± 0.012	0.608 ± 0.030	0.211 ± 0.037	0.475 ± 0.016
$0.9 - 1.7$	1.3	1.141 ± 0.008	1.179 ± 0.014	0.503 ± 0.035	0.321 ± 0.044	0.405 ± 0.019
$1.7 - 3.0$	2.2	1.034 ± 0.006	0.876 ± 0.011	0.393 ± 0.029	0.436 ± 0.036	0.376 ± 0.016
$3.0 - 5.3$	4.0	0.881 ± 0.008	0.554 ± 0.013	0.420 ± 0.034	0.353 ± 0.043	0.249 ± 0.018
$5.3 - 9.5$	7.1	0.731 ± 0.009	0.322 ± 0.014	0.282 ± 0.039	0.343 ± 0.049	0.208 ± 0.021
$9.5 - 16.9$	12.7	0.563 ± 0.010	0.193 ± 0.015	0.251 ± 0.044	0.205 ± 0.055	0.092 ± 0.023
$16.9 - 30.0$	22.5	0.507 ± 0.012	0.128 ± 0.018	0.191 ± 0.053	0.263 ± 0.068	0.125 ± 0.029
$30.0 - 53.3$	40.0	0.557 ± 0.015	0.041 ± 0.021	0.096 ± 0.064	0.217 ± 0.083	0.088 ± 0.036
$53.3 - 94.9$	71.1	0.628 ± 0.022	0.020 ± 0.030	0.183 ± 0.093	0.251 ± 0.120	-0.043 ± 0.048
$94.9 - 168.7$	126.5	0.622 ± 0.030	0.080 ± 0.043	0.012 ± 0.125	0.319 ± 0.162	-0.091 ± 0.063
$168.7 - 300.0$	225.0	0.436 ± 0.038	0.174 ± 0.061	-0.039 ± 0.158	-0.015 ± 0.194	0.083 ± 0.086

Table 2.3: Corresponding template fitting coefficients and errors in Figure 2.12

.

be morphologically correlated with other maps of spatial tracers of the ISM. A good candidate is the Schlegel, Finkbeiner, & Davis (SFD) map of Galactic dust, based on 100 μm far IR data (Schlegel et al. 1998). The π^0/bremsstrahlung gamma-ray intensity is proportional to the ISM density $\times$ the CR proton/electron density integrated along the line of sight. As long as the CR proton/electron spectrum and density are approximately spatially uniform, the ISM column density is a good tracer of π^0/bremsstrahlung emission. The dust map has some advantages over gas maps: there are no problems with self absorption, no concerns about "dark gas" (Grenier et al. 2005), and the SFD dust map has sufficient spatial resolution (SFD has spatial resolution of 6', and LAB is 36'). On the other hand, SFD contains no velocity information, so it is impossible to break the map into Galactocentric rings. Nevertheless, it is instructive to employ the SFD map to build a very simple foreground model. The goal is to remove foregrounds in a fashion that reveals the underlying structure with as few physical assumptions as possible. We will compare the resulting residuals using this simple diffuse model with those using the *Fermi* diffuse Galactic model.

As an example, we reveal the *Fermi* bubble structure from $1-5$ GeV *Fermi*-LAT 1.6 yr data in Figure 2.3. We use the SFD dust map as a template of the π^0 gamma foreground. The correlation between *Fermi* and SFD dust is striking, and the most obvious features are removed by this subtraction (*top row* in Figure 2.3). This step makes the bubbles above and below the GC easily visible. The revealed bubbles are not aligned with any structures in the dust map, and cannot plausibly be an artifact of that subtraction.

Next, a simple disk model is subtracted (Figure 2.3, *middle row*). The purpose

of this subtraction is to reveal the structure deeper into the plane, and allow a harder color stretch. The functional form is $(\csc|b|)-1$ in latitude and a Gaussian ($\sigma_\ell = 30^\circ$) in longitude. The disk model mostly removes the IC gamma-rays produced by cosmic ray electrons interacting with the ISRF including CMB, infrared, and optical photons; as discussed previously, such electrons are thought to be mostly injected into the Galactic disk by supernova shock acceleration before diffusing outward.

Finally, we fit a simple double-lobed geometric *bubble* model with flat gamma-ray intensity to the data, to remove the remaining large-scale residuals towards the GC (Figure 2.3, *bottom row*). In this model, we identify the approximate edges of the two bubble-like structures towards the GC in the *bottom left* panel (shown with *dashed green* line in *right* panels of Figure 2.4). We then fill the identified double-lobed bubble structure with uniform gamma ray intensity, as a template for the "*Fermi* bubbles" (*bottom right* panel of Figure 2.3). If the *Fermi* bubbles constitute the projection of a three dimensional two-bubble structure symmetric to the Galactic plane and the minor axis of the Galactic disk, taking the distance to the GC $R_\odot = 8.5$ kpc, the bubble centers are approximately 10 kpc away from us and 5 kpc above and below the Galactic center, extending up to roughly 10 kpc as the most distant edge from GC has $|b| \sim 50^\circ$. No structures like this appear in `GALPROP` models, and in fact `GALPROP` is often run with a box-height smaller than this. Because the structures are so well centered on the GC, they are unlikely to be local.

In Figure 2.4, we show the full sky residual maps at $1-5$ GeV and $5-50$ GeV after subtracting the SFD dust and the disk model to best reveal the *Fermi* bubble features. Although photon Poisson noise is much greater in the $5-50$ GeV map, we identify a *Fermi* bubble structure morphologically similar to the structure in the

$1-5$ GeV map, present both above and below the Galactic plane.

In Figure 2.5, we show the full sky maps at $1-5$ GeV with the zenithal equal area (ZEA) projection with respect to both north pole and south pole. We found no interesting features appear near the poles.

Low Energy Fermi Map as a Diffuse Galactic Model

In Figure 2.6, we show the $0.5-1$ GeV and $2-50$ GeV residual maps after subtracting only the SFD dust map as a template of foreground π^0 gammas. The residual maps should be dominated by IC emission from CR electrons interacting with the ISRF. We use the $0.5-1$ GeV maps as a template of IC emission from high energy electrons scattering *starlight*, and subtract the template from higher energy maps (the *lower panels* of Figure 2.6). The *Fermi* bubble structures are clearly revealed. We thus conclude that the *Fermi* bubbles are mostly from high energy electron CRs IC scattering on CMB photons, and IR photons at higher energies (see Chapter 3.5 for more discussion). By comparing the *Fermi* diffuse Galactic model subtraction (Figure 2.2) and our simple template model subtraction (Figure 2.4), we find that the bubble structures are robust to quite different foreground subtractions. It is difficult to see how such emission could arise – especially with sharp edges – as an artifact of these subtractions.

E range (GeV)	Energy	Uniform	SFD dust	simple disk	north bubble	south bubble	simple loop I
$0.3 - 0.5$	0.4	1.679 ± 0.006	1.205 ± 0.011	0.683 ± 0.027	-0.042 ± 0.050	0.069 ± 0.037	0.496 ± 0.015
$0.5 - 0.9$	0.7	1.363 ± 0.007	1.282 ± 0.012	0.603 ± 0.030	0.140 ± 0.056	0.241 ± 0.041	0.483 ± 0.017
$0.9 - 1.7$	1.3	1.138 ± 0.008	1.187 ± 0.015	0.493 ± 0.035	0.171 ± 0.065	0.385 ± 0.049	0.421 ± 0.020
$1.7 - 3.0$	2.2	1.030 ± 0.007	0.883 ± 0.012	0.384 ± 0.029	0.288 ± 0.054	0.503 ± 0.041	0.391 ± 0.016
$3.0 - 5.3$	4.0	0.881 ± 0.008	0.553 ± 0.013	0.421 ± 0.035	0.368 ± 0.064	0.346 ± 0.049	0.247 ± 0.019
$5.3 - 9.5$	7.1	0.731 ± 0.009	0.321 ± 0.014	0.283 ± 0.039	0.354 ± 0.072	0.337 ± 0.055	0.207 ± 0.022
$9.5 - 16.9$	12.7	0.562 ± 0.010	0.195 ± 0.016	0.248 ± 0.044	0.157 ± 0.078	0.230 ± 0.063	0.097 ± 0.024
$16.9 - 30.0$	22.5	0.509 ± 0.012	0.124 ± 0.018	0.196 ± 0.053	0.353 ± 0.100	0.216 ± 0.076	0.116 ± 0.030
$30.0 - 53.3$	40.0	0.556 ± 0.015	0.042 ± 0.021	0.094 ± 0.064	0.190 ± 0.117	0.232 ± 0.097	0.092 ± 0.038
$53.3 - 94.9$	71.1	0.628 ± 0.022	0.020 ± 0.030	0.184 ± 0.093	0.264 ± 0.164	0.243 ± 0.140	-0.045 ± 0.049
$94.9 - 168.7$	126.5	0.614 ± 0.030	0.091 ± 0.044	0.004 ± 0.126	0.110 ± 0.208	0.450 ± 0.195	-0.068 ± 0.067
$168.7 - 300.0$	225.0	0.429 ± 0.039	0.186 ± 0.064	-0.058 ± 0.160	-0.169 ± 0.254	0.061 ± 0.222	0.107 ± 0.092

Table 2.4: Corresponding template fitting coefficients and errors in *upper right panel* of Figure 2.16.

2.2.2 *Fermi* Bubbles: Morphology

Morphological Features

In the *right* panels of Figure 2.4, we illustrate the edges of the *Fermi* bubbles and some other features. We find that the *Fermi* bubbles have distinct sharp edges, rather than smoothly falling off as modeled in Dobler et al. (2010). Besides the two bubbles symmetric with respect to the Galactic plane, we find one giant *northern arc* that embraces half of the north bubble, that extends from the disk up to $b \sim 50^\circ$, with ℓ ranging from roughly -40° to 0°. It has a brighter and sharper outer edge in the $1-5$ GeV map. On an even larger scale, we identify a fainter structure extended up to $b \sim 80^\circ$, with ℓ ranging from roughly -80° to 50°. We will show in Chapter 3.5 that this large extended structure corresponds to the *North Polar Spur* emission associated with *Loop I* (as seen for example in the Haslam 408 MHz map Haslam et al. 1982a). We will discuss the possible relation of the *Fermi* bubble, the *northern arc*, and the *Loop I* feature in §4.3. In the $1-5$ GeV map, we also identify a "donut-like" structure in the south sky with b ranging from roughly -35° to 0° and ℓ from roughly 0° to 40°. The coordinates of the *Fermi* bubble edges, *northern arc*, *Loop I*, and the "donut" feature identified from the $1-5$ GeV map are listed in Table 2.2.

In Figure 2.7 we compare the *Fermi* bubble morphology in different energy bins. We show the difference of the $1-2$ and $2-5$ GeV residual maps in the *upper panels*; each residual map is the result of subtracting the SFD dust map and the simple disk model to best reveal the *Fermi* bubbles. The difference maps between the $1-5$ and $5-50$ GeV maps are shown in the *lower panels*. The bubble features

almost disappear in the difference maps, indicating that different parts of the *Fermi* bubbles have similar spectra.

To study the sharp edges of the bubbles at high latitude more carefully, we examine the (projected) intensity profiles along arcs of great circles passing through the estimated centers of the north and south bubbles, and intersecting the bubble edge (as defined in Figure 2.4) at $|b| > 28^\circ$. Along each such ray, we define the intersection of the arc with the bubble edge to be the origin of the coordinate system; we then perform an inverse-variance-weighted average of the intensity profile along the rays (as a function of distance from the bubble edge). We subtract a constant offset from the profile along each ray, prior to averaging the rays together, to minimize aliasing of point sources onto the averaged profile, and then add the averaged offset back in at the end. The inverse variance for each data point is obtained from the Poisson errors in the original photon data, prior to any subtraction of point sources or templates (however, the smoothing of the map is taken into account). When the rays are averaged together, the naive inverse variance in the result is multiplied by a factor of the annulus radius (for the points being averaged together) divided by $4\pi\sigma^2$, where σ is the 1σ value of the PSF, and the annulus width is taken to be 1° (the spacing between the points along the rays; this is comparable to the smoothing scale, so there may still be unaccounted-for correlations between the displayed errors); this is done to take into account that the number of independent measurements being sampled by the rays can be far less than the number of rays, especially close to the center of the bubbles. This procedure is repeated for all the stages of the template subtraction, using the simple disk template for inverse Compton scattering (ICS) for illustration (our conclusions

do not depend on this choice).

The results are shown in Figure 2.8 for the averaged $(1-2)+(2-5)$ GeV maps, and the averaged $(5-10)+(10-20)$ GeV maps. In both energy ranges the edges are clearly visible; in the south, this is true even before any templates are subtracted. The intensity profile of the north bubble is strikingly similar to the profile of the south bubble. For both of the north and south bubbles, no significant edge-brightening or limb-brightening of the bubbles is apparent from the profiles, the flux is fairly uniform inside the bubbles.

In Figure 2.9, we plot the intensity profile as a function of latitude from the south to the north pole. We construct great circle arcs perpendicular to the $l = 0$ great circle, extending 10° in each direction (east and west), and average the emission over each such arc. The flatness of the bubbles with latitude (except possibly close to the Galactic plane), and the sharp edges at high latitude, are also apparent here.

We note that the flat intensity of the bubbles is striking. As we show in Figure 2.10, if we assume that the *Fermi* bubbles are projected from spherically symmetric three-dimensional bubbles centered above and below the GC, a non-trivial emissivity distribution in the bubble interior is required to produce a flat projected intensity distribution. If the "bubbles" originate from IC scattering, this suggests a rather non-uniform density distribution for the electron CRs, which – combined with a nearly uniform spectral index – presents challenges for many models for the electron injection. In Figure 2.10, the *top left* panel shows a toy model of the *Fermi* bubbles with flat projected intensity. In this model, the volume emissivity (assuming the ISM is optically thin to gamma rays) is proportional to $(R^2 - r^2)^{-1/2}$ for $r < R$, and

zero otherwise, where R=3.5 kpc is the approximate radius of the two bubbles, and r is the distance to the center of the north or south bubble. The *top right* panel shows a bubble intensity profile for a shock generated bubble with compressed gas shells (assuming a thickness of 0.5 kpc); the electron CR density in the shell is a factor of 5 higher than in the interior of the bubbles. For this model, a limb-brightened edge of the bubbles is clearly visible, in contrast to *Fermi* observations. The *bottom left* shows an illustrative toy model for the *WMAP* haze. The haze synchrotron emissivity depends on the electron CR density and the magnetic field; here we take $B = B_0 e^{-z/z_0}$, where $z_0 = 2$ kpc, and show the line of sight integral of this B-field through bubble volume. Even though the synchrotron emissivity is not simply the product of CR density times field strength, this panel suggests that the decreasing intensity of the *WMAP* haze at high latitudes is due to the decay of the Galactic magnetic field away from the Galactic plane. And in *bottom right* panel, a toy model for the *ROSAT* X-ray features was shown. The observed soft X-rays are limb-brightened and we assume all gas is uniformly distributed within a compressed shell, with no contribution from the interior, and X-ray emission is proportional to the gas density squared.

Spectrum of Gamma-ray Emission

We now attempt to estimate the spectrum of the gamma rays associated with the *Fermi* bubbles, and the spatial variation of the spectrum. In order to reveal the hardness of the spectrum of the *Fermi* bubbles, and quantitatively study the intensity flatness of the bubble interiors, we do a careful regression template fitting. First, we maximize the Poisson likelihood of a simple diffuse emission model

E range (GeV)	Energy	Uniform	SFD dust	whole bubble	$0.5 - 1.0$ GeV - SFD
$0.3 - 0.5$	0.4	1.759 ± 0.006	0.883 ± 0.012	-0.026 ± 0.026	1.181 ± 0.017
$0.5 - 0.9$	0.7	1.446 ± 0.006	0.905 ± 0.013	0.008 ± 0.029	1.275 ± 0.018
$0.9 - 1.7$	1.3	1.208 ± 0.008	0.929 ± 0.016	0.258 ± 0.034	0.897 ± 0.020
$1.7 - 3.0$	2.2	1.088 ± 0.006	0.679 ± 0.012	0.375 ± 0.029	0.736 ± 0.017
$3.0 - 5.3$	4.0	0.921 ± 0.007	0.427 ± 0.014	0.428 ± 0.034	0.530 ± 0.019
$5.3 - 9.5$	7.1	0.759 ± 0.008	0.231 ± 0.015	0.371 ± 0.039	0.400 ± 0.021
$9.5 - 16.9$	12.7	0.580 ± 0.009	0.131 ± 0.016	0.269 ± 0.043	0.270 ± 0.023
$16.9 - 30.0$	22.5	0.522 ± 0.011	0.072 ± 0.016	0.290 ± 0.053	0.261 ± 0.020
$30.0 - 53.3$	40.0	0.565 ± 0.014	0.015 ± 0.021	0.225 ± 0.066	0.141 ± 0.034
$53.3 - 94.9$	71.1	0.631 ± 0.021	0.010 ± 0.033	0.364 ± 0.096	0.065 ± 0.053
$94.9 - 168.7$	126.5	0.615 ± 0.029	0.083 ± 0.048	0.337 ± 0.127	-0.032 ± 0.076
$168.7 - 300.0$	225.0	0.441 ± 0.037	0.149 ± 0.068	-0.104 ± 0.137	0.089 ± 0.097

Table 2.5: Corresponding template fitting coefficients and errors in Figure 2.14

.

involving 5-templates (see §2.2.1). In this model, we include the SFD dust map (Figure 2.3, *right panel* of the top row) as a tracer of π^0 emission which is dominant (or nearly so) at most energies on the disk and significant even at high latitudes, the simple disk model (Figure 2.3, *right panel* of the *second row*), the bubble template (Figure 2.3, *right panel* of the bottom row), the *Loop I* template (see e.g. Figure 2.11, *left panel* of the *top row*), and a uniform background as templates to weight the *Fermi* data properly.

The significant isotropic background is due to extra-galactic emission and charged particle contamination, including heavy nuclei at high energies. The *Fermi* collaboration has measured the extragalactic diffuse emission using additional cuts to reduce charged particle contamination (Abdo et al. 2010): below ~ 20 GeV the isotropic contribution in our fits is roughly a factor of 2 larger than the extragalactic diffuse emission, but has a similar spectral slope. At energies above ~ 20 GeV the isotropic contribution becomes much harder, which we attribute to charged particle contamination.

For each set of model parameters, we compute the Poisson log likelihood,

$$\ln \mathcal{L} = \sum_i k_i \ln \mu_i - \mu_i - \ln(k_i!), \tag{2.1}$$

where μ_i is the synthetic map (i.e., linear combination of templates) at pixel i, and k is the map of observed data. The last term is a function of only the observed maps. The 1σ Gaussian error is calculated from the likelihood by $\Delta \ln \mathcal{L} = 1/2$. The error bars are simply the square root of the diagonals of the covariance matrix. We refer to Appendix B of Dobler et al. (2010) for more details of the likelihood analysis. Maps of the models constructed from linear combinations of these five templates,

and the residual maps between the *Fermi* data and the combined templates at different energy bins, are shown in Figure 2.11. In this fit, we mask out all pixels with Galactic latitude $|b| < 30^\circ$ (the dashed black line in the residual maps). The *left* column shows the linear combination of the disk, *Loop I* (North Polar Spur), uniform, and bubble templates that provide the best fit to the *Fermi* maps after subtracting the best fit SFD dust template (shown in the *middle* column). The difference maps between the combined template and the data are shown in the *right* column. The template fitting is done for the region with $|b| > 30^\circ$ to avoid contaminations from the Galactic disk (shown with black dashed line in the *right* column residual maps). The subtraction of the model largely removes the features seen in the *Fermi* maps with $|b| > 30^\circ$. We use the same gray scale for all the panels. We find that both the disk IC template and *Loop I* features fade off with increasing energy, but the bubble template is required for all the energy bands and does not fade off with increasing energy. The oversubtraction in the residual maps, especially at lower energy bins, is due to the simple disk IC model, which is not a good template across the entire disk. However, outside the masked region, the residual maps are consistent with Poisson noise without obvious large scale features.

Template-correlated spectra for the 5-template fit are shown in Figure 2.12. The fitting is done with regions of $|b| > 30^\circ$. For a template that has units (e.g., the SFD dust map is in E_{B-V} magnitudes) the correlation spectrum has obscure units (e.g. gamma-ray emission per magnitude). In such a case we multiply the correlation spectrum by the average SFD value in the bubble region, defined by the *bottom right* panel of Figure 2.3, masking out the $|b| < 30^\circ$ region. For the uniform, *Loop I*, and bubble templates (including inner, outer, north, and south), no renormalization

is done. These templates are simply ones and zeros (smoothed to the appropriate PSF), so the outer bubble spectrum is simply the spectrum of the bubble shell template shown in Figure 2.15, *not* the mean of this template over the whole bubble region. The normalization factors for different templates are listed in Table 2.1. From Figure 2.12 we can see that the bubble component has a notably harder (consistent with flat) spectrum than the other template-correlated spectra, and the models for the various emission mechanism generated from `GALPROP`, indicating that the *Fermi* bubbles constitute a distinct component with a hard spectrum. The fitting is done over the $|b| > 30^\circ$ region. Note that these `GALPROP` "predictions" are intended only to indicate the expected spectral shape for these emission components, for reference. The correlation coefficients for the SFD map and simple disk model are multiplied by the average value of these maps in the bubble region (defined by the *bottom right* panel of Figure 2.3, with a $|b| > 30^\circ$ cut) to obtain the associated gamma-ray emission; see §2.2.2 for details, and Table 2.1 for a summary of the normalization factors.

In Figure 2.12, we show spectra for π^0 emission, bremsstrahlung and inverse Compton scattering calculated using a sample `GALPROP` model (tuned to match locally measured protons and anti-protons as well as locally measured electrons at $\sim 20 - 30$ GeV), as an indication of the expected spectral shapes. The spectra for the SFD and the simple disk template reasonably match the model expectations. The dust map mostly traces the π^0 emission, and the simple disk model resembles a combination of IC and bremsstrahlung emission. The spectrum for emission correlated with the *Fermi* bubbles is clearly significantly harder than either of these components, consistent with a *flat* spectrum in $E^2 dN/dE$. This fact coupled with

the distinct spatial morphology of the *Fermi* bubbles indicates that the IC bubbles are generated by a *separate* electron component. We also note that the spectrum of the bubble template falls off significantly at energy $\lesssim$1 GeV. This feature is robust with respect to the choice of templates. The fitting coefficients and corresponding errors of each template are listed in Table 2.3. We will discuss some implications of the falling spectrum in §3.3.

To demonstrate the robustness of the spectrum we have derived for the *Fermi* bubbles, we make use of the *Fermi* $0.5-1$ GeV residual map (after subtracting the SFD dust map to largely remove the π^0 gammas) as a template of IC emission, and perform a 4-template fit (§2.2.1). These gamma rays mostly originate from IC scattering of a relatively soft population of electrons in the disk, but might also contain gammas from IC scattering on *starlight* by a latitudinally extended electron population. We use the SFD dust map as a template for π^0 gammas as previously, and include the uniform background and the bubble template as in the previous 5-template fit. The fitting is done with regions of $|b| > 30^\circ$. For the SFD dust map and the *Fermi* $0.5-1$ GeV IC template, the correlation coefficients are weighted by the mean of each template in the "bubble" region. The resulting model and the difference maps with respect to the *Fermi* data, at different energy bands, are shown in Figure 2.13. The *left* column shows the best fit combined template including the residual $0.5-1$ GeV map, uniform, SFD dust, and bubble templates. The *middle* column shows the *Fermi*-LAT data in different energy bins. The difference maps between the combined template and the data are shown in the *right* column. The template fitting is done over the region with $|b| > 30^\circ$ (shown with black dashed line in the *right* column residual maps). We use the same grey scale for all the panels.

We find that the bubble template does not fade away with increasing energy. The 4-template fit works extremely well, at $|b| > 30^\circ$ the residual maps are consistent with Poisson noise without obvious large scale features, and there are no obvious sharp features in the data closer to the disk. The residuals are remarkably small. The spectrum is shown in Figure 2.14. The *Fermi* $0.5 - 1$ GeV IC template appears to contain a small fraction of π^0 gammas, but the spectral index is consistent with the predicted `GALPROP` IC component. The fitting coefficients and corresponding errors of each template are listed in Table 2.5.

By eye, the *Fermi* bubbles appear to possess north-south symmetry and are close to spatially uniform in intensity (with a hard cutoff at the bubble edges). To test these hypotheses more quantitatively, we split the *Fermi* bubble template into the *inner bubble* and *outer shell* templates (*upper row* of Figure 2.15), or alternatively into the *north* and *south bubble* templates (*lower row* of Figure 2.15). We then repeat the previous 5-template and 4-template fitting procedure involving either the simple disk IC template or the *Fermi* $0.5 - 1$ GeV IC template, but splitting the bubble template to either *inner bubble and outer shell* or *north and south bubble* templates. The goal is to identify variations in the intensity and spectral index between the bubble edge and interior, and the northern and southern bubbles.

The resulting fitted spectra are shown in Figure 2.16. In the *top row*, we use the simple disk model as the IC template. In the *left* panel, we split the previous bubble template into *bubble interior* and *bubble shell* templates (see Figure 2.15 for the templates). The correlation coefficients of the 6-template fit involving the two bubble templates are shown. The purple dash-dotted line and blue triple-dot-dashed

line are for the inner bubble and the outer shell template respectively. The two templates have a consistent spectrum which is significantly harder than the other templates, indicating the *bubble interior* and the *bubble shell* have the same distinct physical origin. In the *right* panel, we split the bubble template into *north* and *south* bubbles. As we include the *Loop I* template (which has a softer spectrum) in the north sky for regression fitting, the north bubble has a slightly harder spectrum than the south bubble. Again, both of the templates have harder spectra than any other components in the fit. In the *Bottom row*, we employ the *Fermi* $0.5 - 1$ GeV residual map (after subtracting the SFD dust) as a template for the *starlight* IC. In the *left* panel, we split the bubble template into *bubble interior* and *bubble shell* templates. In the *right* panel, we split the bubble template into *north bubble* and *south bubble* templates. As in Figure 2.12, the energy spectra have been normalized to a reference region; see §2.2.2 for details, and Table 2.1 for a summary of the normalization factors. And the corresponding fitting coefficients and errors of each template are listed in Table 2.6, Table 2.4, Table 2.7, and Table 2.8 respectively. In Figure 2.17, we replace the simple disk model with the Haslam 408 MHz map as the IC template, and employ the SFD map, a uniform background, the *Loop I* template, and the double-lobed bubble (*left* panel) or the *north and south bubble* (*right* panel) templates in the fitting. The Haslam map contains a bright feature associated with *Loop I* and is dominated by synchrotron emission from softer electron CRs, of energies around 1 GeV; it is not an ideal tracer of IC emission which depends on both electron and ISRF distribution. The resulting best-fit spectrum for the bubble template remains harder than the other components, but with enhanced lower energy ($\lesssim 2$ GeV) correlation coefficients compared to Figure 2.12 and Figure 2.14.

The *right* panel of Figure 2.17 is the same as the *left* panel, but with the bubble template divided into north and south bubbles. The correlation spectra have been normalized to a reference region; see §2.2.2 for details, and Table 2.1 for a summary of the normalization factors. Our conclusion is that the *Fermi* bubbles appear to be north-south symmetric and spatially and spectrally uniform, with a hard spectrum. This statement is largely independent of our choice of template for the disk IC emission.

Dobler et al. (2010) claimed that the gamma-ray emission not accounted for by the known foregrounds could be well fitted by a bivariate Gaussian with $\sigma_b = 25^\circ$, $\sigma_l = 15^\circ$. With the improved 1.6 yr data, the edges of the excess at high latitudes are seen to be quite sharp, and are not well-described by a Gaussian fall-off in intensity. The choice of the bivariate Gaussian template by Dobler et al. (2010) was intended to remove as much of the remaining gamma ray signal as possible, once the π^0 and soft IC emission had been regressed out, minimizing large-scale residuals. The fits were performed with only $|b| < 5$ masked out. In this chapter, on the other hand, we have masked out all emission with $|b| < 30^\circ$; when attempting to subtract the disk-correlated emission, and delineating the "bubbles" template, our goal has been to isolate the sharp-edged features from the more slowly spatially varying emission, not to account for all the observed emission.

This difference in approach can be seen in the non-negligible residuals around the inner Galaxy ($|b| \lesssim 20^\circ$) in many of our maps (for example, Figure 2.13). An attempt to fit all the residual emission simultaneously with a simple template may well require a template closer to that used by Dobler et al. (2010), rather than the bubble template. However, the sharp edges now visible in the data, and their

E range (GeV)	Energy	Uniform	SFD dust	simple disk	inner bubble	outer bubble	simple loop I
$0.3 - 0.5$	0.4	1.681 ± 0.006	1.201 ± 0.011	0.683 ± 0.027	0.071 ± 0.042	0.004 ± 0.040	0.490 ± 0.015
$0.5 - 0.9$	0.7	1.365 ± 0.007	1.279 ± 0.012	0.607 ± 0.030	0.215 ± 0.048	0.207 ± 0.045	0.475 ± 0.016
$0.9 - 1.7$	1.3	1.142 ± 0.008	1.179 ± 0.014	0.498 ± 0.036	0.354 ± 0.057	0.293 ± 0.053	0.407 ± 0.019
$1.7 - 3.0$	2.2	1.034 ± 0.006	0.876 ± 0.011	0.403 ± 0.029	0.370 ± 0.047	0.491 ± 0.045	0.373 ± 0.016
$3.0 - 5.3$	4.0	0.880 ± 0.008	0.554 ± 0.013	0.426 ± 0.035	0.307 ± 0.056	0.393 ± 0.054	0.247 ± 0.018
$5.3 - 9.5$	7.1	0.731 ± 0.009	0.322 ± 0.014	0.284 ± 0.039	0.330 ± 0.064	0.354 ± 0.061	0.207 ± 0.021
$9.5 - 16.9$	12.7	0.562 ± 0.010	0.193 ± 0.015	0.265 ± 0.044	0.100 ± 0.070	0.293 ± 0.069	0.087 ± 0.023
$16.9 - 30.0$	22.5	0.506 ± 0.012	0.128 ± 0.018	0.201 ± 0.054	0.182 ± 0.088	0.335 ± 0.087	0.121 ± 0.029
$30.0 - 53.3$	40.0	0.556 ± 0.015	0.041 ± 0.021	0.098 ± 0.065	0.190 ± 0.106	0.243 ± 0.107	0.087 ± 0.036
$53.3 - 94.9$	71.1	0.627 ± 0.022	0.020 ± 0.030	0.187 ± 0.093	0.206 ± 0.151	0.294 ± 0.153	-0.045 ± 0.048
$94.9 - 168.7$	126.5	0.620 ± 0.030	0.081 ± 0.043	0.037 ± 0.129	0.180 ± 0.209	0.431 ± 0.207	-0.098 ± 0.064
$168.7 - 300.0$	225.0	0.435 ± 0.038	0.179 ± 0.062	-0.065 ± 0.155	0.145 ± 0.242	-0.178 ± 0.206	0.097 ± 0.086

Table 2.6: Corresponding template fitting coefficients and errors in *upper left panel* of Figure 2.16.

alignment with the edges of the *WMAP* haze and *ROSAT* X-ray features (as we will discuss in Chapter 3), motivate us to consider the bubbles as originating from a distinct physical mechanism. While the bubbles probably do not constitute the entire "*Fermi* haze" discussed by Dobler et al. (2010), they are certainly a major component of it, dominating the signal at high latitudes.

E range (GeV)	Energy	Uniform	SFD dust	inner bubble	outer bubble	$0.5 - 1.0$ GeV - SFD
$0.3 - 0.5$	0.4	1.759 ± 0.006	0.883 ± 0.012	0.011 ± 0.035	-0.069 ± 0.037	1.180 ± 0.017
$0.5 - 0.9$	0.7	1.446 ± 0.006	0.905 ± 0.013	0.005 ± 0.039	0.012 ± 0.041	1.275 ± 0.018
$0.9 - 1.7$	1.3	1.208 ± 0.008	0.929 ± 0.016	0.284 ± 0.047	0.230 ± 0.048	0.896 ± 0.020
$1.7 - 3.0$	2.2	1.088 ± 0.006	0.680 ± 0.012	0.309 ± 0.039	0.444 ± 0.041	0.737 ± 0.017
$3.0 - 5.3$	4.0	0.921 ± 0.007	0.427 ± 0.014	0.399 ± 0.047	0.459 ± 0.049	0.530 ± 0.019
$5.3 - 9.5$	7.1	0.759 ± 0.008	0.231 ± 0.015	0.362 ± 0.053	0.382 ± 0.056	0.400 ± 0.021
$9.5 - 16.9$	12.7	0.580 ± 0.009	0.131 ± 0.016	0.195 ± 0.057	0.351 ± 0.063	0.271 ± 0.023
$16.9 - 30.0$	22.5	0.523 ± 0.011	0.069 ± 0.015	0.218 ± 0.071	0.368 ± 0.079	0.261 ± 0.018
$30.0 - 53.3$	40.0	0.565 ± 0.012	0.014 ± 0.015	0.202 ± 0.088	0.249 ± 0.096	0.144 ± 0.025
$53.3 - 94.9$	71.1	0.631 ± 0.021	0.010 ± 0.033	0.337 ± 0.128	0.394 ± 0.140	0.065 ± 0.053
$94.9 - 168.7$	126.5	0.614 ± 0.029	0.084 ± 0.048	0.232 ± 0.164	0.455 ± 0.190	-0.029 ± 0.076
$168.7 - 300.0$	225.0	0.440 ± 0.037	0.152 ± 0.069	0.021 ± 0.195	-0.262 ± 0.175	0.088 ± 0.096

Table 2.7: Corresponding template fitting coefficients and errors in *lower left panel* of Figure 2.16.

E range (GeV)	Energy	Uniform	SFD dust	north bubble	south bubble	0.5 – 1.0 GeV - SFD
0.3 – 0.5	0.4	1.759 ± 0.006	0.882 ± 0.012	-0.011 ± 0.047	-0.031 ± 0.029	1.180 ± 0.017
0.5 – 0.9	0.7	1.446 ± 0.006	0.905 ± 0.013	-0.009 ± 0.052	0.014 ± 0.032	1.276 ± 0.018
0.9 – 1.7	1.3	1.207 ± 0.008	0.931 ± 0.016	0.201 ± 0.061	0.277 ± 0.038	0.899 ± 0.020
1.7 – 3.0	2.2	1.087 ± 0.006	0.681 ± 0.013	0.331 ± 0.050	0.391 ± 0.033	0.738 ± 0.017
3.0 – 5.3	4.0	0.922 ± 0.007	0.424 ± 0.014	0.500 ± 0.060	0.399 ± 0.039	0.527 ± 0.019
5.3 – 9.5	7.1	0.760 ± 0.008	0.228 ± 0.015	0.440 ± 0.067	0.342 ± 0.045	0.397 ± 0.021
9.5 – 16.9	12.7	0.580 ± 0.009	0.132 ± 0.016	0.231 ± 0.072	0.286 ± 0.051	0.272 ± 0.023
16.9 – 30.0	22.5	0.524 ± 0.011	0.068 ± 0.015	0.406 ± 0.091	0.236 ± 0.060	0.257 ± 0.008
30.0 – 53.3	40.0	0.565 ± 0.014	0.014 ± 0.015	0.227 ± 0.105	0.222 ± 0.077	0.143 ± 0.015
53.3 – 94.9	71.1	0.631 ± 0.021	0.011 ± 0.033	0.339 ± 0.151	0.376 ± 0.115	0.067 ± 0.054
94.9 – 168.7	126.5	0.608 ± 0.029	0.091 ± 0.049	0.067 ± 0.189	0.470 ± 0.162	-0.013 ± 0.077
168.7 – 300.0	225.0	0.437 ± 0.038	0.156 ± 0.070	-0.216 ± 0.229	-0.066 ± 0.160	0.095 ± 0.098

Table 2.8: Corresponding template fitting coefficients and errors in *lower right panel* of Figure 2.16.

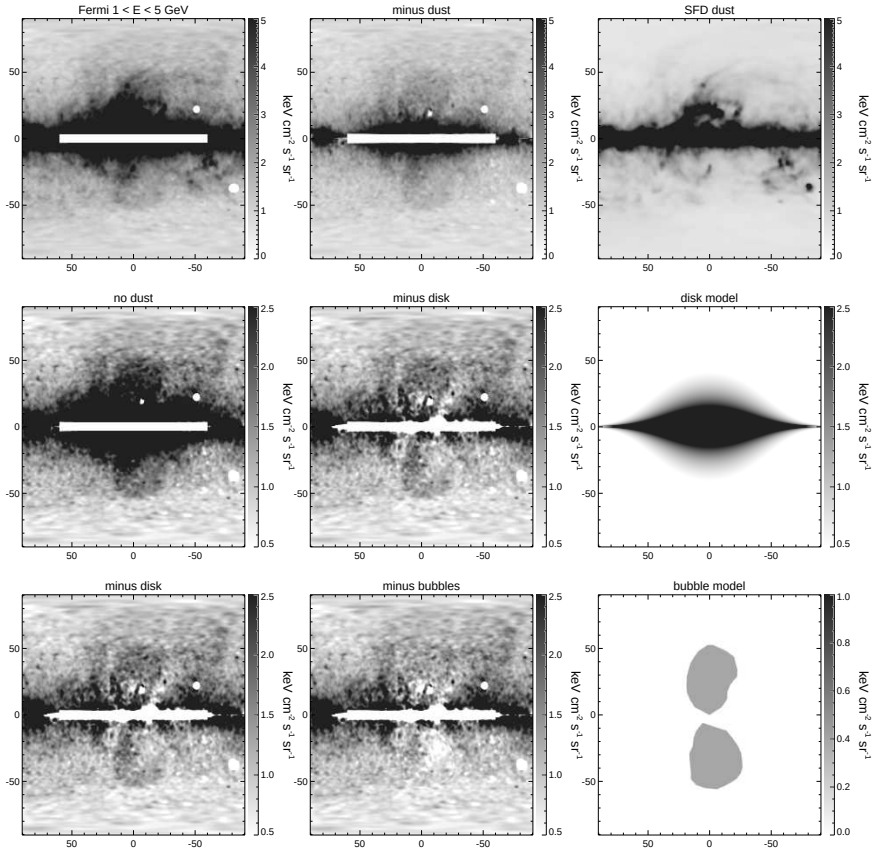

Figure 2.3.— Template decomposition of the *Fermi*-LAT 1.6 year $1-5$ GeV map (see §2.2.1). *Top left:* Point source subtracted $1-5$ GeV map, and large sources, including the inner disk ($-2^\circ < b < 2^\circ, -60^\circ < \ell < 60^\circ$), have been masked. *Top middle:* The $1-5$ GeV map minus SFD dust map (*top right* panel). *Middle row:* The *left* panel is the same as the *top middle* panel but stretched $2\times$ harder. The *middle* panel subtracts a simple geometric disk template (shown in the *right* panel). Two large bubbles are apparent (spanning $-50^\circ < b < 50^\circ$). *Bottom row:* The *left* panel is the same as the *middle* panel of the *second row*. Finally we subtract a simple bubble template (*right* panel) with uniform projected intensity. After subtracting the bubble template, the two bubbles features have nearly vanished (*bottom middle* panel), indicating a nearly flat intensity for the *Fermi* bubbles.

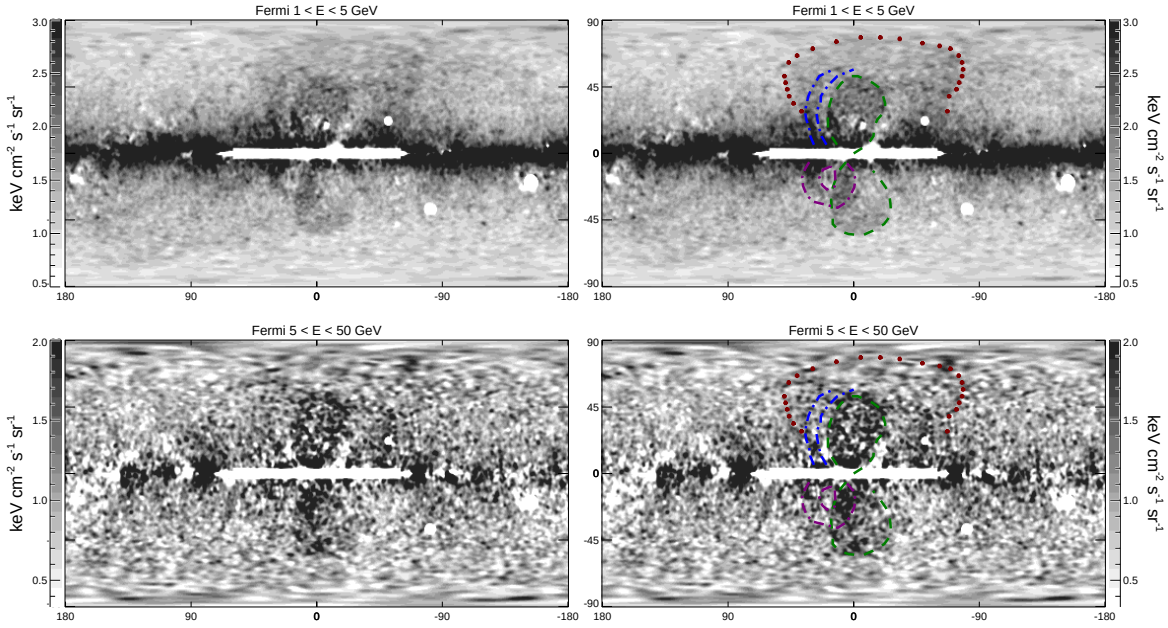

Figure 2.4.— Full sky residual maps after subtracting the SFD dust and disk templates from the *Fermi*-LAT 1.6 year gamma-ray maps in two energy bins. Point sources are subtracted, and large sources, including the inner disk ($-2^\circ < b < 2^\circ, -60^\circ < \ell < 60^\circ$), have been masked. Two large bubbles are seen (spanning $-50^\circ < b < 50^\circ$) in both cases. *Right panels:* Apparent *Fermi* bubble features marked in color lines, overplotted on the maps displayed in the *left panels*. Green dashed circles above and below the Galactic plane indicate the approximate edges of the north and south *Fermi* bubbles respectively. Two blue dashed arcs mark the inner (dimmer) and outer (brighter) edges of the *northern arc* – a feature in the northern sky outside the north bubble. The red dotted line approximately marks the edge of *Loop I*. The purple dot-dashed line indicates a tentatively identified "donut" structure.

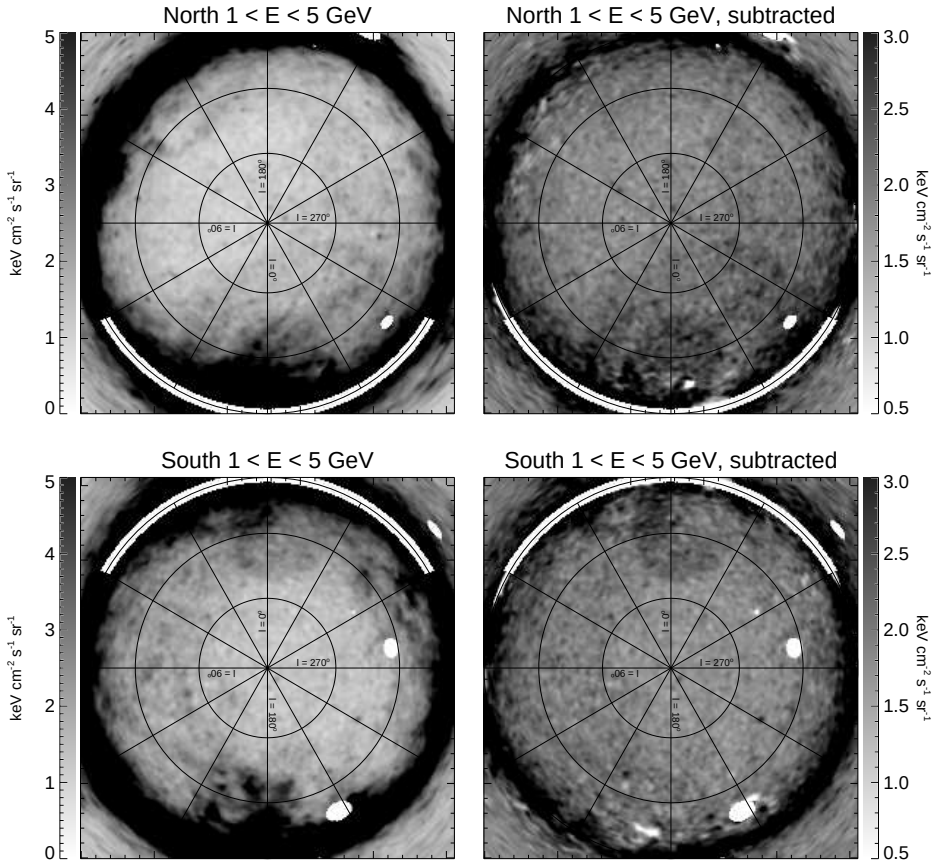

Figure 2.5.— The zenithal equal area (ZEA) projection with respect to both north pole (*upper panels*) and south pole (*lower panels*) for the $1 - 5$ GeV energy band before (*left panels*) and after (*right panels*) subtracting the SFD dust and simple disk templates to reveal the *Fermi* bubbles.

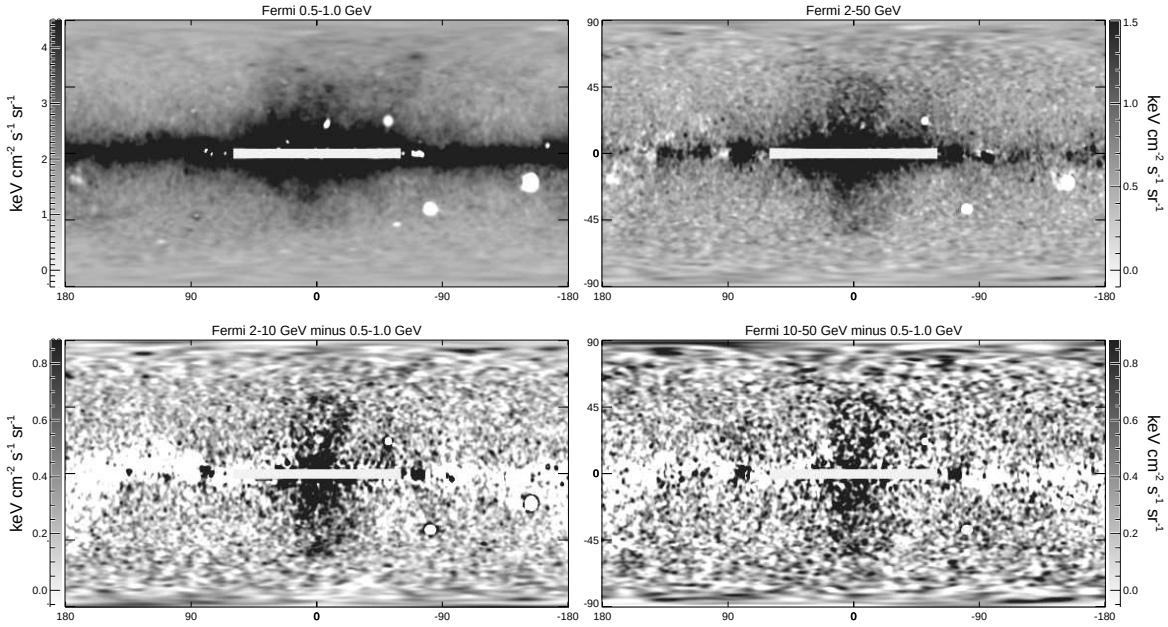

Figure 2.6.— *Top left:* Full sky *Fermi*-LAT 1.6 year $0.5-1.0$ GeV map subtracts the SFD dust map as a template of π^0 gammas. *Top right:* The same as *top left* panel, but for energy range $2-50$ GeV (note the different gray scale for the two panels). *Bottom left:* The $2-10$ GeV *Fermi* gamma-ray map subtracting the *top left* $0.5-1.0$ GeV residual map which is used as a template of ICS of *starlight*. *Bottom right:* The same as *bottom left* panel but for $10-50$ GeV map subtracting the *top left* $0.5-1.0$ GeV residual map. The *Fermi* bubble structures are better revealed after subtracting the lower energy $0.5-1.0$ GeV residual map with extended disk-like emission.

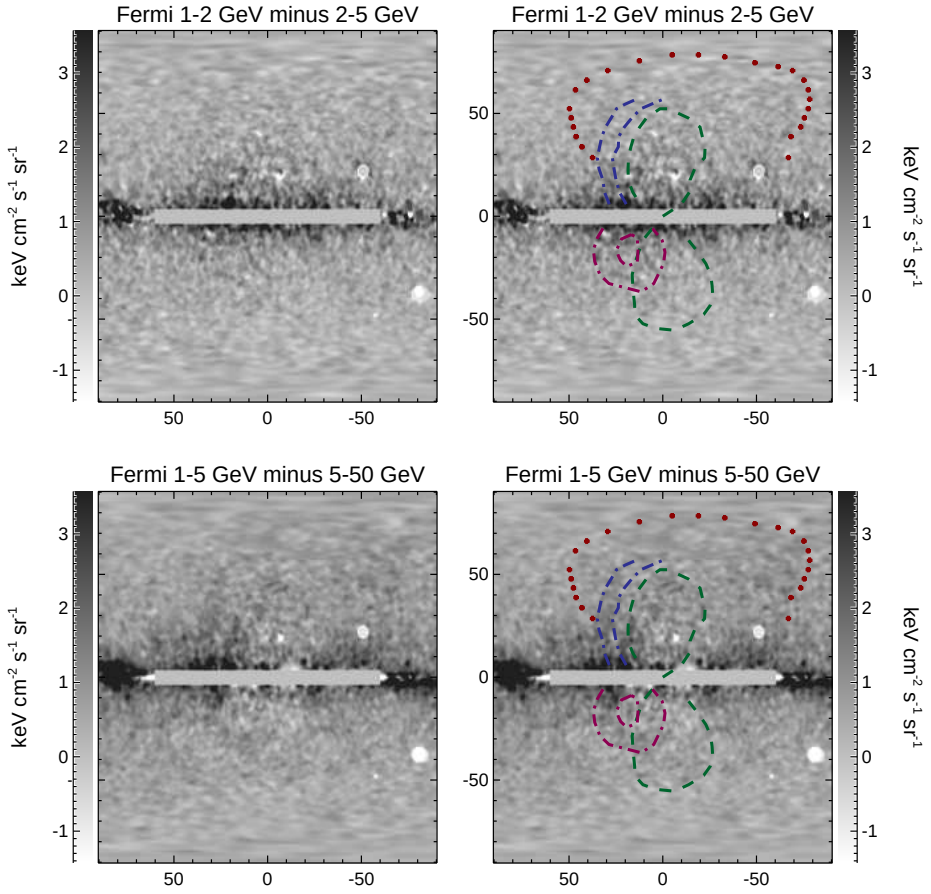

Figure 2.7.— Comparison of the *Fermi* bubbles between different energy bins. *Top left:* Subtraction of the $2-5$ GeV residual map from the $1-2$ GeV residual map; each residual map is constructed from the data by regressing out the SFD dust and disk templates to best reveal the *Fermi* bubbles. The difference map is consistent with Poisson noise away from the masked region, and the bubble features can hardly be recognized, indicating that different spatial regions of the *Fermi* bubbles have the same spectrum. *Top right:* The same map as *left* panel, but with the *Fermi* bubble features overplotted for comparison. The marked features are the same as those plotted in Figure 2.4, and are listed in Table 2.2. *Bottom row:* Same as the *upper panels*, but subtracting the $5-50$ GeV residual map from the $1-5$ GeV residual map.

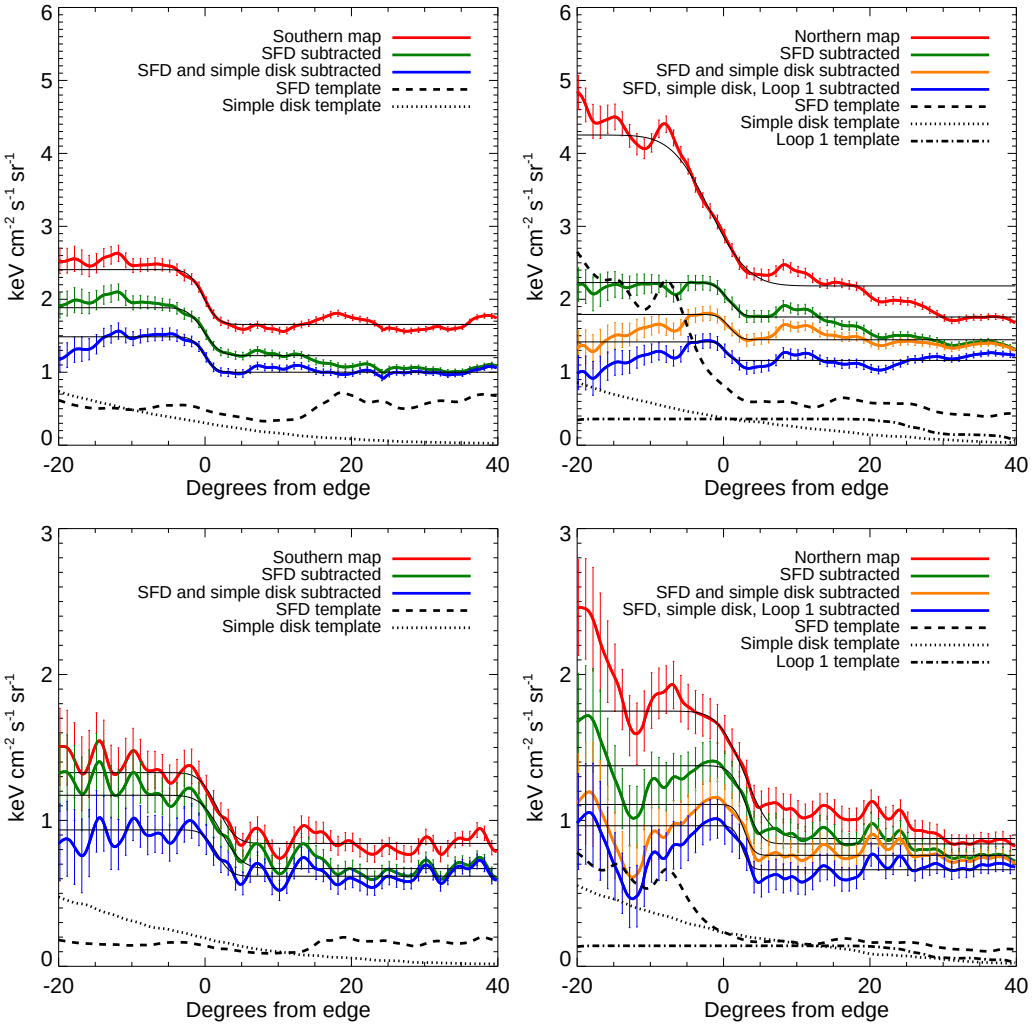

Figure 2.8.— Intensity as a function of radial distance from the bubble edge, averaged over great circle arcs intersecting the bubble center and lying at $|b| > 28°$. Results are shown for (*left*) the southern bubble, and (*right*) the northern bubble, for (*top*) the averaged $1-2$ and $2-5$ GeV maps, and (*bottom*) the averaged $5-10$ and $10-20$ GeV maps. Different lines show the results at different stages of the template regression procedure and the corresponding errors are plotted (see text for an outline of the error analysis).

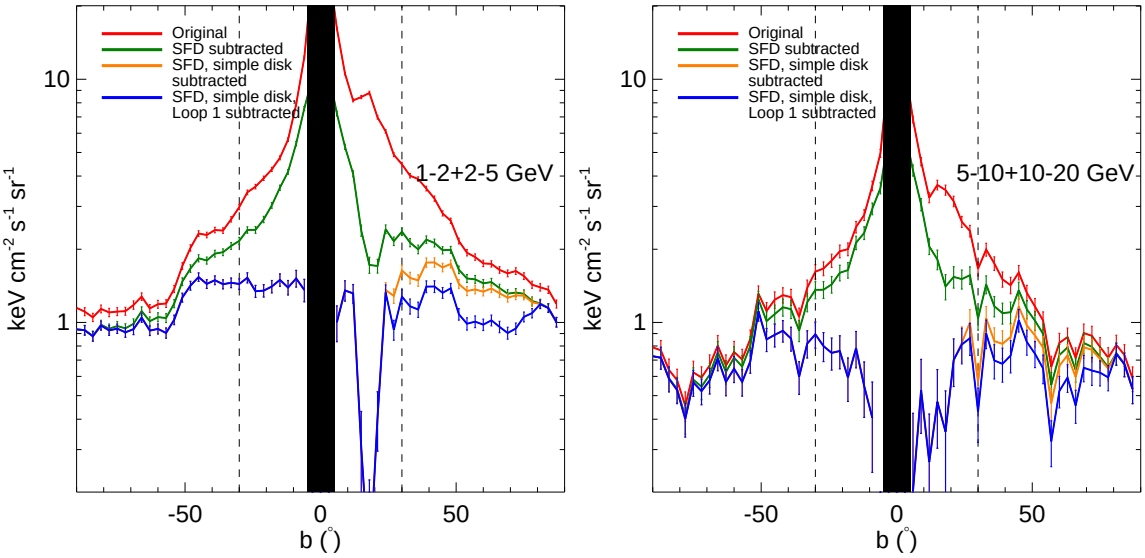

Figure 2.9.— Intensity averaged over the central 20 degrees in longitude, as a function of latitude, for (*left*) the averaged $1-2$ and $2-5$ GeV maps, and (*right*) the averaged 5-10 and 10-20 GeV maps. We construct great circle arcs perpendicular to the $l = 0$ great circle, extending 10° in each direction (east and west), and average the emission over each such arc; the "b" label corresponding to each arc, and the x-axis of the plot, refers to the value of b at $l = 0$. Different lines show the results at different stages of the template subtraction process. The large oversubtraction at $b \sim 15°$ in the north, especially pronounced in the low-energy data, is associated with a bright feature in the SFD dust map.

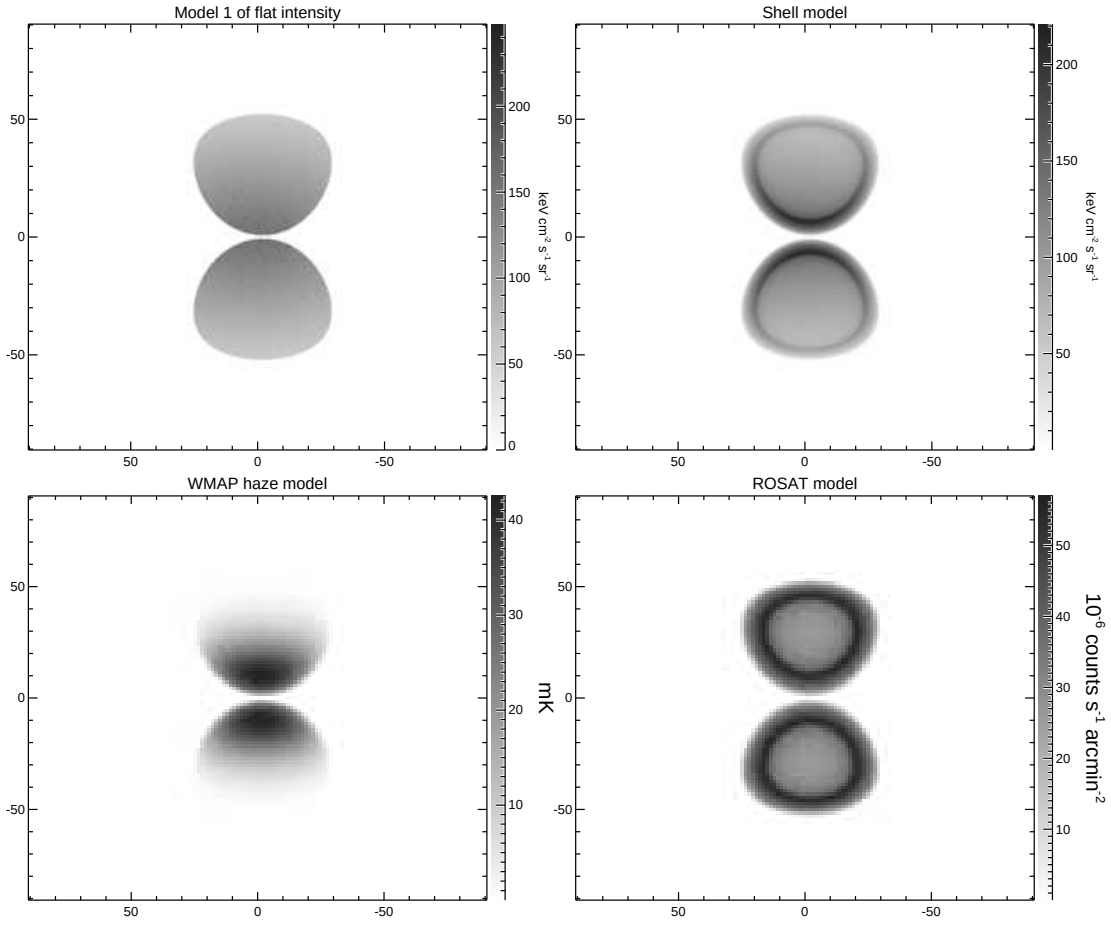

Figure 2.10.— Four different models of emissivity distributions to illustrate the qualitative features of expected projected gamma-ray, microwave, and X-ray emissions (Detailed explanations see §2.2.1).

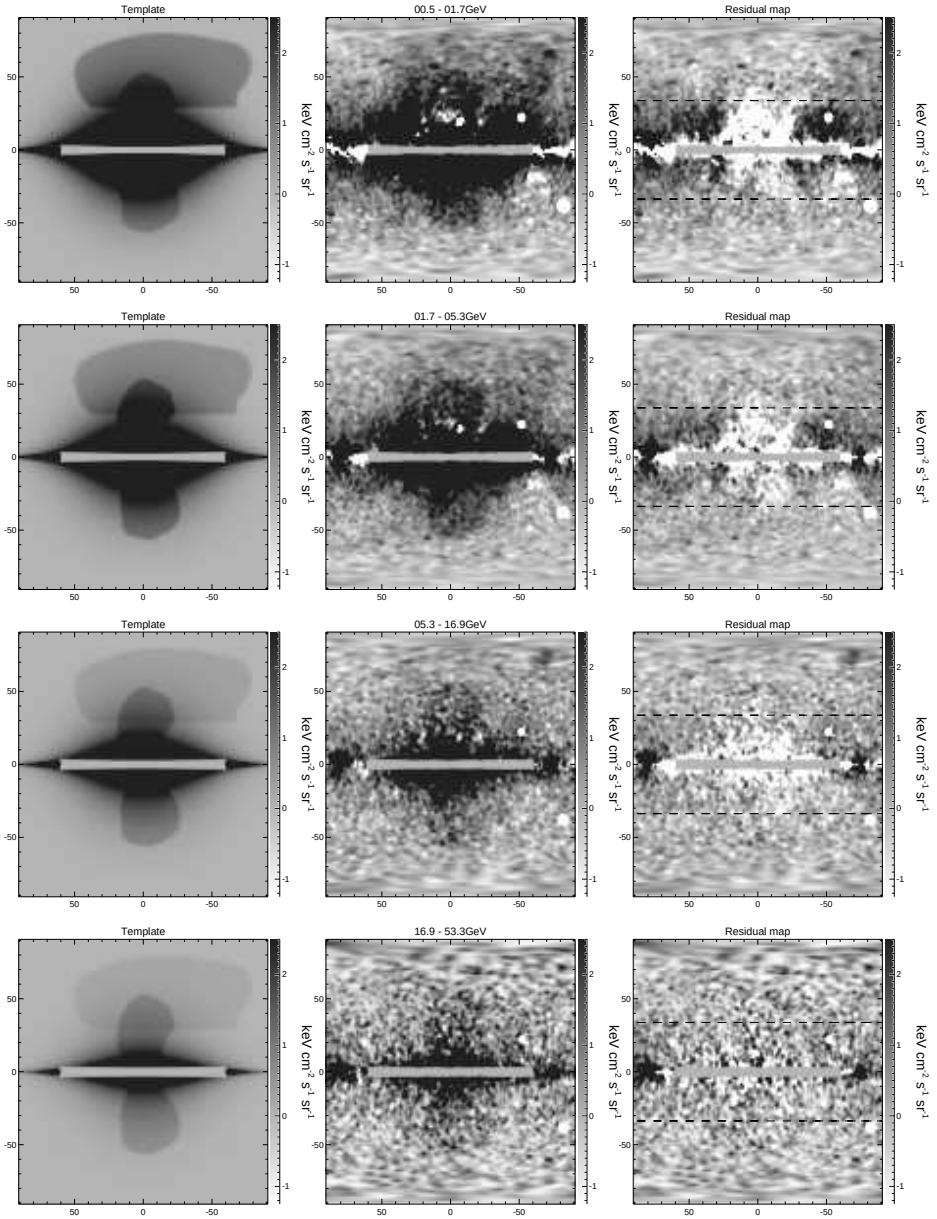

Figure 2.11.— The models obtained from the 5-template fits including the geometric disk model, SFD dust map, Loop I, uniform background, and the bubble template, compared with the *Fermi* maps, in different energy bins.

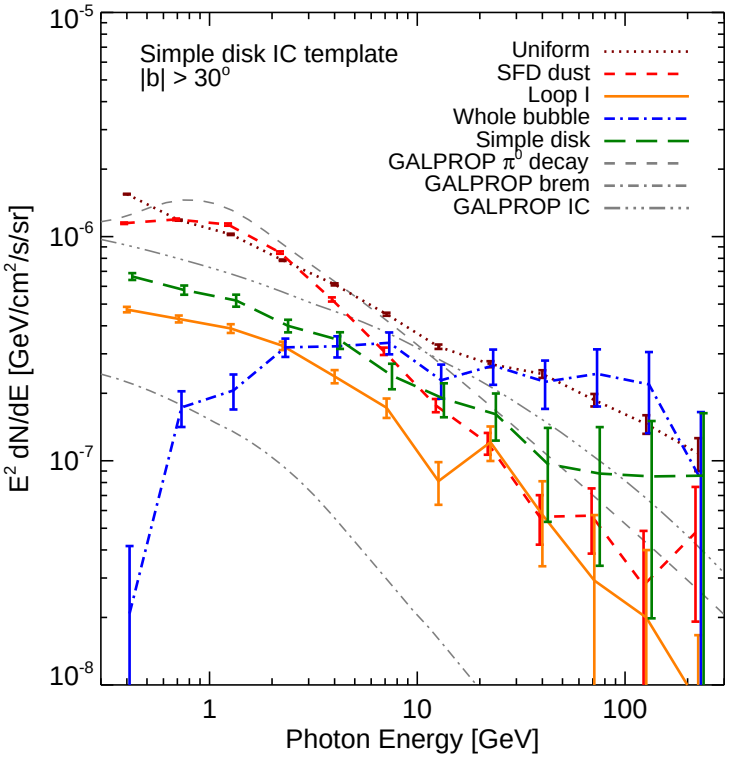

Figure 2.12.— Energy spectra for the 5-template fit employing a simple disk model for the IC (and to a lesser degree bremsstrahlung) emission from supernova-shock-accelerated electrons (see §2.2.2). The SFD-correlated spectrum is shown by the red short-dashed line which roughly traces π^0 emission (the gray dashed line indicates a `GALPROP` prediction for π^0 emission). The disk-correlated emission is shown by the green dashed line, which traces the soft IC (gray triple-dot-dashed line) and bremsstrahlung (gray dot-dashed line) component. The spectrum of the uniform emission, which traces the isotropic background (including possible cosmic-ray contamination), is shown as a dotted brown line. The solid orange line indicates the spectrum of emission correlated with *Loop I*, which has a similar spectrum to the disk-correlated emission. Finally, the blue dot-dashed line shows the spectrum correlated with the *Fermi* bubble template.

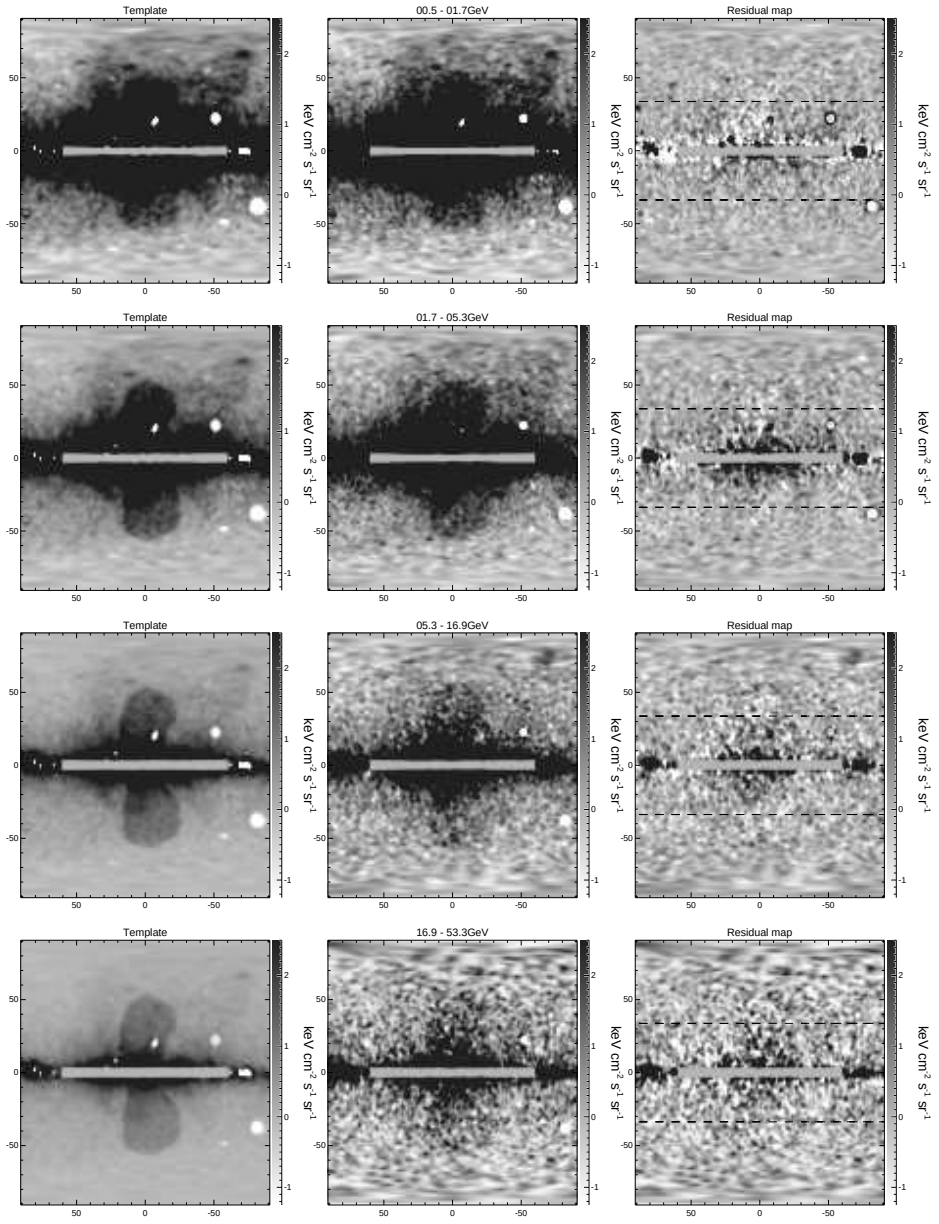

Figure 2.13.— The same as Figure 2.11, but using the *Fermi* $0.5 - 1$ GeV residual map after subtracting emission correlated with the SFD dust map (to remove the π^0 gammas) as a template for low-latitude IC emission (originating primarily from scatterings on *starlight*, and likely involving softer supernova-shock-accelerated electrons).

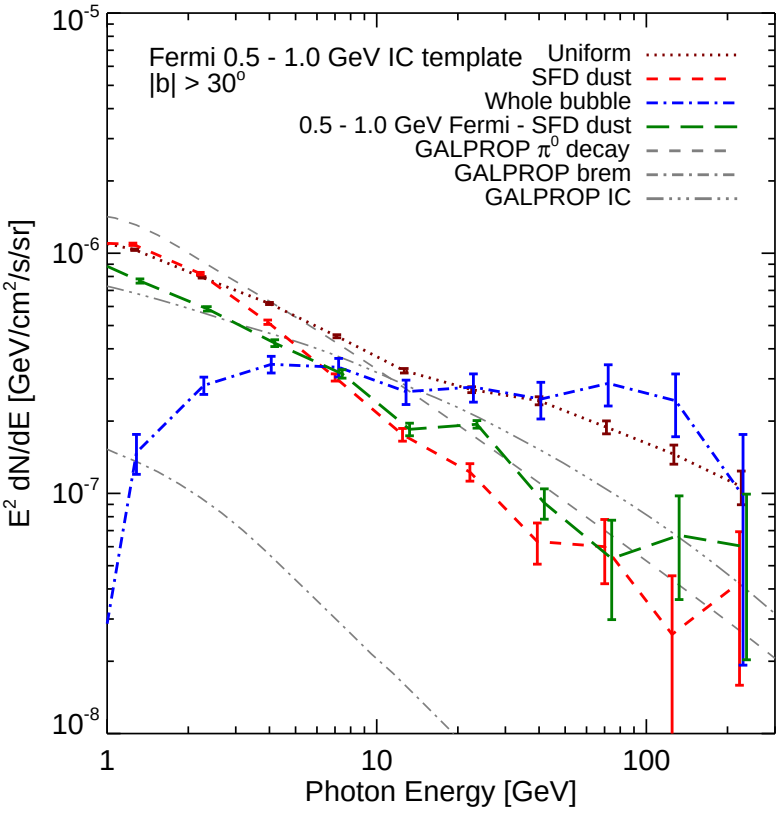

Figure 2.14.— Same as Figure 2.12, but correlation spectra for the 4-template fit employing the *Fermi* $0.5 - 1$ GeV residual map (after subtracting the SFD dust) as a template for the *starlight* IC. The line style is the same as Figure 2.12. Again, we find that the spectrum correlated with the *Fermi* bubble template (blue dot-dashed line) is harder (consistent with flat in E^2dN/dE) than the spectra correlated with the other templates, and the models for the various emission mechanism generated from `GALPROP`, indicating that the *Fermi* bubbles constitute a distinct gamma-ray component with a hard spectrum. The fitting is done for $|b| > 30°$. As in Figure 2.12, the correlation spectra have been normalized to a reference region; see §2.2.2 for details, and Table 2.1 for a summary of the normalization factors.

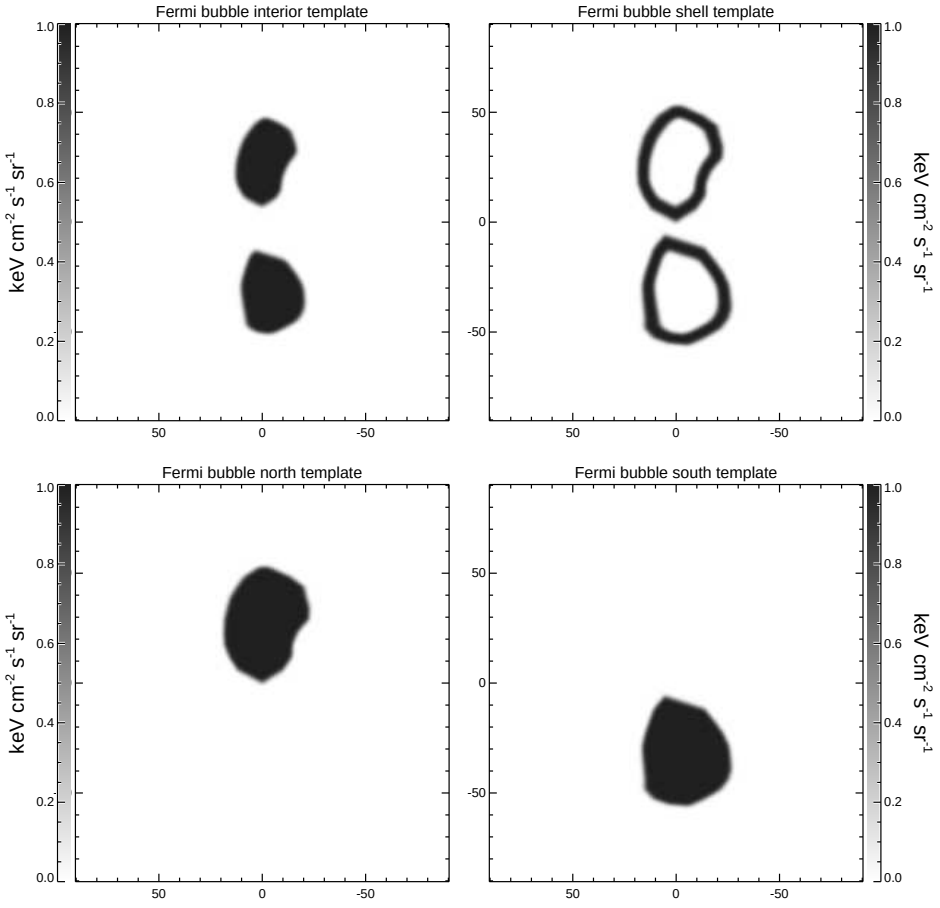

Figure 2.15.— *Top row:* We split our *Fermi* bubble template (shown in the *bottom right* panel of Figure 2.3) into two components for template fitting: an interior template (*top left*) and a shell template (*top right*) with uniform intensity, in order to reveal any potential spectrum difference with the template fitting technique. *Bottom row:* We split the *Fermi* bubble template into north bubble template (*bottom left*) and south bubble template (*bottom right*). If the two bubbles have the same origin, they should not only have similar morphologies but also consistent spectra.

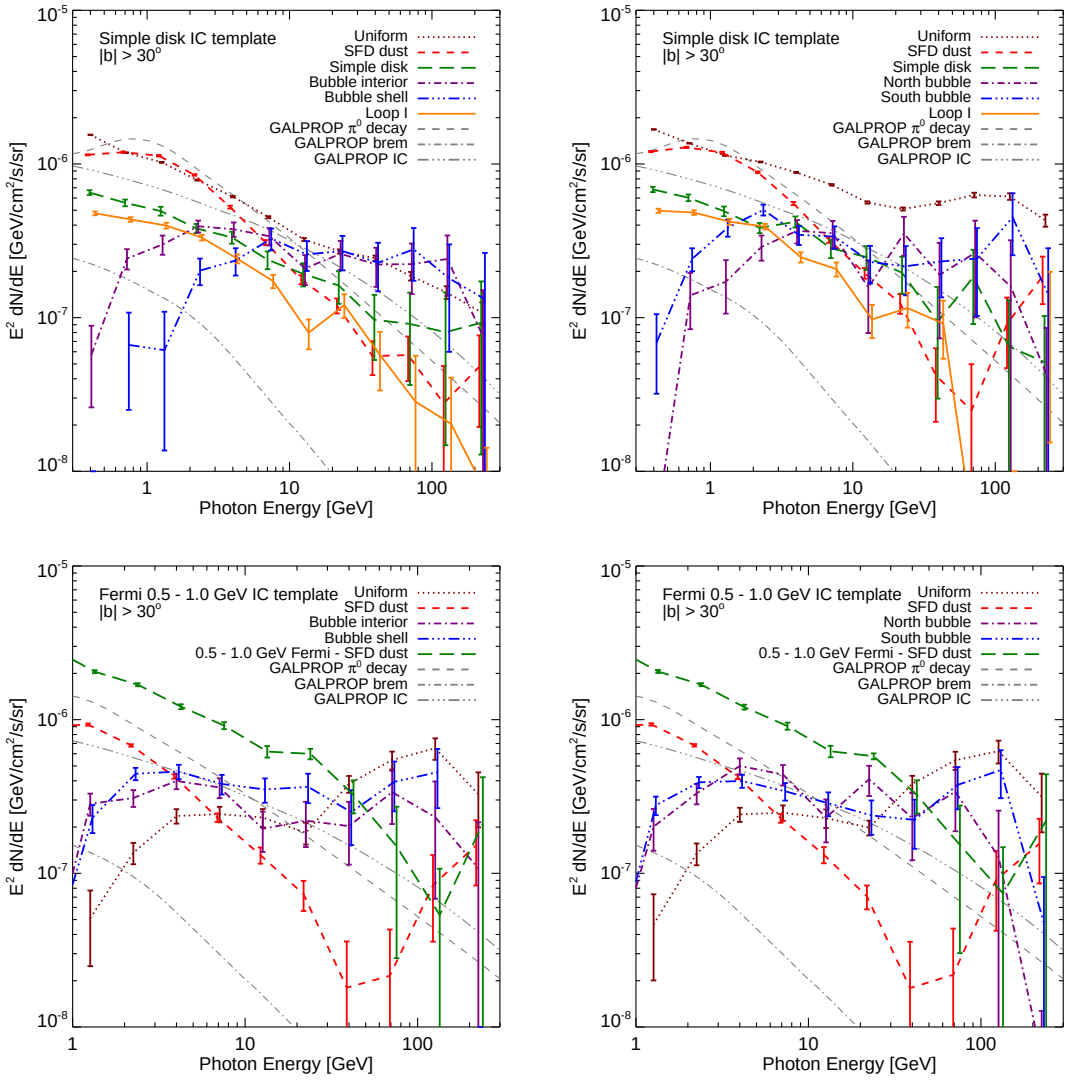

Figure 2.16.— Same as Figure 2.12 and Figure 2.14, but splitting the *Fermi* bubble template into two components for template fitting. The line styles are the same as Figure 2.12.

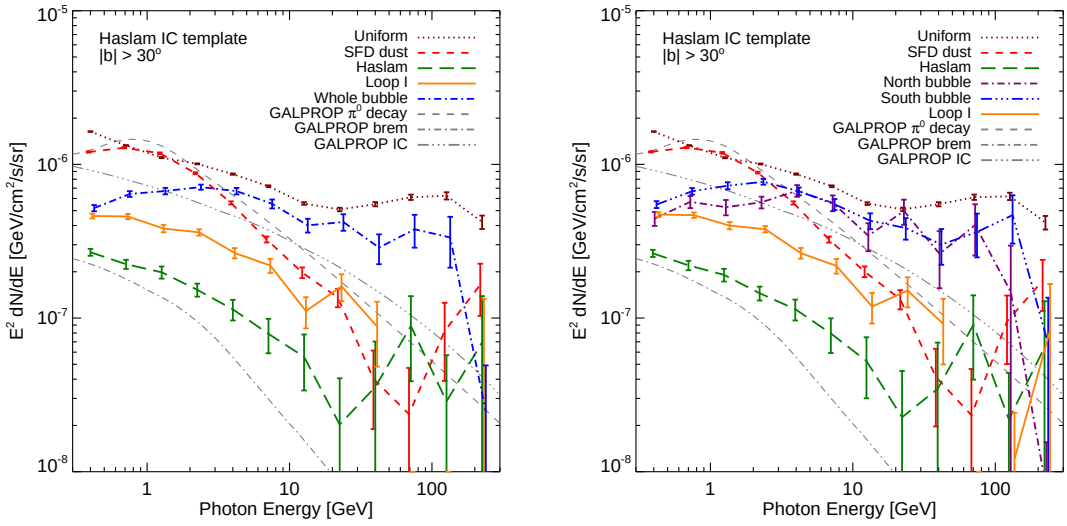

Figure 2.17.— Same as Figure 2.12, but using the Haslam 408 MHz map instead of the simple disk model as the IC template.

Chapter 3

Fermi bubbles Seen in Other Wavelengths

In this Chapter, we compare the $1-5$ GeV *Fermi* bubble with the *ROSAT* 1.5 keV soft X-ray map, the *WMAP* 23 GHz microwave haze, and the Haslam 408 MHz map. The striking similarities of several morphological features in these maps strongly suggest a common physical origin for the *Fermi* bubbles, *WMAP* haze, and X-ray edges towards the GC (Figure 3.1).

3.1 Comparison with *ROSAT* X-ray Features

The *ROSAT* all-sky survey provides full-sky images at energies from $0.5-2$ keV.[1] We compare the morphology of the X-ray features in *ROSAT* 1.5 keV map (band

[1] http://hea-www.harvard.edu/rosat/rsdc.html

R6 and R7) with the edges of the *Fermi* bubbles in detail in Figure 3.2. The limb brightened X-ray features align with the edges of both the north and south *Fermi* bubble. Hints of the whole north bubble are also visible in *ROSAT*, as well as two sharp edges in the south that trace the south *Fermi* bubble close to the disk. We show the *ROSAT* 1.5 keV map overplotted with the edges of the *Fermi* bubbles, the *northern arc*, the *"donut"* and the *Loop I* features in the *right* panels of Figure 3.2. The appearance of the X-ray edges in the *ROSAT* 1.5 keV map, coincident with the *Fermi* bubble edges, strongly supports the physical reality of these sharp edges.

In Figure 3.3, we subtract the *ROSAT* 1.0 keV soft X-ray map (band R5) from the 1.5 keV (R6 and R7) map to clean up the foreground. We find that the extended *Loop I* feature has a softer spectrum than the X-ray features associated with the bubble edges, and is largely removed in the difference map (*lower left* panel of Figure 3.3). The residual features strikingly overlap with the edges of the *Fermi* bubbles (*lower right* panel). No other noticeable large scale features appear in the residual X-ray map which do not appear in the gamma-rays.

3.2 Comparison with WMAP Microwave Haze

The *WMAP* haze is the residual remaining in *WMAP* microwave data after regressing out contributions from thermal dust, free-free, and "soft synchrotron" traced by the Haslam 408 MHz radio survey (Haslam et al. 1982a). Therefore, it is by construction harder than the Haslam-correlated emission. We will show in this section that the *WMAP* synchrotron haze appears to be associated with the *Fermi* bubbles.

Figure 3.4 shows a detailed morphological comparison of the south *Fermi* bubble at $1-5$ GeV with the southern part of the *WMAP* microwave haze at 23 GHz (K-band). The edge of the *Fermi* bubbles, marked in green dashed line in the *top right* and *lower right* panels, closely traces the edge of the *WMAP* haze. The smaller latitudinal extension of the *WMAP* haze may be due to the decay of the magnetic field strength with latitude. These striking morphological similarities between the *WMAP* microwave haze and *Fermi* gamma-ray bubble can be readily explained if the *same* electron CR population is responsible for both excesses, with the electron CRs interacting with the galactic magnetic field to produce synchrotron, and interacting with the ISRF to produce IC emission.

In Figure 3.5, we show the difference maps between the 23 GHz *WMAP* haze and the 33 GHz and 41 GHz haze maps. The difference maps contain no apparent features and indicate a common spectrum of different regions inside the *WMAP* haze, suggesting a single physical origin for the bulk of the signal. We have reached the same conclusion for the *Fermi* bubbles in Figure 2.7.

Besides the similarity of the morphology, the relatively hard spectrum of the *Fermi* bubble also motivates a common physical origin with the *WMAP* haze. We now provide a simple estimate of the microwave synchrotron and gamma-ray ICS signals from one single population of hard electrons distributed in the inner Galaxy, to demonstrate that the magnitudes and spectral indices of the two signals are consistent for reasonable parameter values.

For a highly relativistic electron scattering on low energy photons, the spectrum

of upscattered photons is given by Blumenthal & Gould (1970) (Cholis et al. 2009),

$$\begin{aligned}\frac{dN}{dE_\gamma d\epsilon dt} &= \frac{3}{4}\sigma_T c\frac{(m_e c^2)^2}{\epsilon E_e^2}\big(2q\log q + (1+2q)(1-q) \\ &\quad +0.5(1-q)(\Gamma q)^2/(1+\Gamma q)\big)n(\epsilon), \end{aligned} \tag{3.1}$$

$$\Gamma = 4\epsilon E_e/(m_e c^2)^2, \quad q = \frac{E_\gamma}{E_e}\frac{1}{\Gamma(1-E_\gamma/E_e)},$$

$$\epsilon < E_\gamma < E_e\Gamma/(1+\Gamma).$$

Here ϵ is the initial photon energy, E_e is the electron energy, E_γ is the energy of the upscattered gamma ray, and $n(\epsilon)$ describes the energy distribution of the soft photons per unit volume. Where $\Gamma \ll 1$, in the Thomson limit, the average energy of the upscattered photons is given by,

$$\langle E_\gamma \rangle = (4/3)\gamma^2\langle\epsilon\rangle, \tag{3.2}$$

where $\gamma = E_e/m_e c^2$ is the Lorentz boost of the electron. In the Klein-Nishina (KN) limit, $\Gamma \gg 1$, the spectrum instead peaks at the high energy end, and the upscattered photon carries away almost all the energy of the electron.

Given a power law steady-state electron spectrum with spectral index γ, the spectral index of the IC scattered gamma rays is $(\gamma+1)/2$ in the Thomson limit, and $\gamma+1$ in the extreme KN limit (e.g. Blumenthal & Gould 1970). Photons in the *Fermi* energy range can be produced by scattering of $\mathcal{O}(10-100)$ GeV electrons on starlight, which is (marginally) in the KN regime, or by Thomson scattering of much higher-energy electrons on IR or CMB photons. Consequently, the spectral index of gamma rays might be expected to vary with latitude even if the electron spectral index is uniform, becoming harder at higher latitudes where scatterings in the Thomson limit dominate. Closer to the disk, where much of the ISRF energy

density is in starlight, IC scatterings are in neither the extreme KN nor Thomson limits, and the spectrum needs to be computed carefully.

We consider a steady-state electron spectrum described by a power law, $dN/dE \propto E^{-\gamma}$, with energy cutoffs at 0.1 GeV and 1000 GeV. The choice of high-energy cutoff is motivated by the local measurement of the cosmic ray electron spectrum by *Fermi* (Abdo et al. 2009b). We consider a region ~ 4 kpc above the Galactic center, as an example (and since both the *WMAP* haze and *Fermi* bubbles are reasonably well measured there), and employ the model for the ISRF used in `GALPROP` version 50p (Porter & Strong 2005) at 4 kpc above the GC. We normalize the synchrotron to the approximate value measured by *WMAP* in the 23 GHz K-band (Hooper et al. 2007), $\sim 25^\circ$ below the Galactic plane, and compute the corresponding synchrotron and IC spectra. The *WMAP* haze was estimated to have a spectrum $I_\nu \propto \nu^{-\beta}$, $\beta = 0.39 - 0.67$ (Dobler & Finkbeiner 2008), corresponding approximately to an electron spectral index of $\gamma \approx 1.8 - 2.4$; Figure 3.6 shows our results for a magnetic field of 10 μG and 5 μG at 4 kpc above the GC, and electron spectral indices $\gamma = 1.8 - 3$. We find good agreement in the case of $\alpha \approx 2 - 2.5$, consistent with the spectrum of the *WMAP* haze. In this figure, the interstellar radiation field model is taken from `GALPROP` version 50p, and the magnetic field is set to be 10 μG for the *left* panel and 5 μG for the *right* panel. The data points in the upper panels show the magnitude of the bubble emission obtained from template fitting in Figure 2.12 (*brown*) and Figure 2.14 (*black*) including the "whole bubble" template, as a function of energy. The lowest and highest bins contain 3σ upper limits rather than data points with 1σ error bars, due to the large uncertainties in the haze amplitude at those energies. For reference, a rectangular cross hatch region

shows a approximate spectrum in the same place in this and subsequent figures. The data point in the lower panel shows the magnitude of the *WMAP* haze averaged over $b = -20^\circ$ to -30°, for $|\ell| < 10^\circ$, in the 23 GHz K-band (the overall normalization is chosen to fit this value), and the gray area indicates the range of synchrotron spectral indices allowed for the *WMAP* haze by Dobler & Finkbeiner (2008). The same population of hard electrons can consistently generate the *WMAP* synchrotron haze and *Fermi* ICS bubbles.

In the default `GALPROP` exponential model for the Galactic magnetic field, $|B| = |B_0|e^{-z/z_s}$ with scale height $z_s \approx 2$ kpc, this field strength would correspond to $B_0 \approx 30 - 40$ μG or even higher. This value is considerably larger than commonly used (e.g. Page et al. 2007). However, models with a non-exponential halo magnetic field, as discussed by e.g. Alvarez-Muñiz et al. (2002); Sun et al. (2008), can have $\sim$ 10 μG fields well off the plane.

We note also that the extrapolated value of B_0 required to obtain good agreement between the IC and synchrotron amplitudes, in the exponential model, is somewhat higher than found by Dobler et al. (2010), who performed the comparison at 2 kpc. This apparent discrepancy originates from the fact that in the haze latitudinal profile given by Hooper et al. (2007), the emission falls off rapidly with latitude for $0 > b > -15^\circ$, but then plateaus at $b \sim -15 - 35^\circ$, contrary to expectations based on a B-field profile exponentially falling away from $z = 0$. This suggests either that the magnetic field inside the bubble does not fall exponentially with $|z|$ inside the bubbles, or that the *WMAP* haze contains a significant free-free component at high latitude.

3.3 Evidence of a ~ 700 GeV Electron Excess?

In Figure 3.7, we calculate the gamma-ray spectrum from IC scattering, using the standard ISRF model taken from `GALPROP` – as in Figure 3.6, but with a different energy range for the electron CRs. An electron CR population with a hard low-energy cutoff at about 500 GeV can fit the *Fermi* bubble spectrum better than a single power law extending from $0.1 - 1000$ GeV, due to the downturn in the spectrum in the lowest energy bin. Even a rather hard ($dN/dE \sim E^{-2}$) power law component at $300 - 500$ GeV produces a long tail at low energies. Interestingly, this preferred $500 - 700$ GeV energy range is rather close to the peak in local $e^+ + e^-$ cosmic rays observed by *ATIC* (Chang et al. 2008)[2]. We note that although the estimated error bars of energy lower than 1 GeV mildly depend on the templates we use in the fitting procedure, the fall-off of the bubble intensity in the lowest energy bins is robust. Figure 3.6 shows the same analysis for 500-900 GeV electrons with two different templates for the disk IC emission, for the bubble interior and shell separately, and for the north and south bubbles. In all cases the same cut-off in the spectrum below 1 GeV is observed.

In this case, while the lowest energy bin in the gamma-rays is better fitted, the lack of low-energy CRs means that synchrotron can contribute to the *WMAP* haze only at the sub-percent level, unless the magnetic field in the inner galaxy is extreme (and even then the spectrum does not reproduce the observations). In this case an alternate explanation for the *WMAP* haze would need to be considered.

[2]However, note that the large peak observed by *ATIC*-2 and *ATIC*-4 appears to be in conflict with the *Fermi* measurement of the spectrum, which contains no such feature.

As suggested initially in Finkbeiner (2004a), the *WMAP* haze could originate from free-free emission (thermal bremsstrahlung), and this would explain the lack of a clear haze signal in *WMAP* polarization maps. However, the spectrum of the haze is somewhat softer than generally expected from free-free emission; the gas temperature required is also thermally unstable, requiring a significant energy injection ($\sim 10^{54-55}$ ergs) to maintain its temperature (Hooper et al. 2007; McQuinn & Zaldarriaga 2010).

3.4 Gamma-ray power and e^- cosmic ray density

In order to estimate the total gamma-ray power emitted by the bubbles, we must estimate the surface brightness integrated over energy, the solid angle subtended, and the distance (suitably averaged). From Figure 2.12 we take the intensity to be $E^2dN/dE = 3 \times 10^{-7}\,\mathrm{GeV\,cm^{-2}s^{-1}sr^{-1}}$ from $1 - 100$ GeV, integrating to $1.4{\times}10^{-6}\,\mathrm{GeV\,cm^{-2}s^{-1}sr^{-1}}$. The bubble template used in our analysis (Figure 2.3) subtends 0.808 sr, yielding a total bubble flux of $1.13{\times}10^{-6}$ $\mathrm{GeV\,cm^{-2}s^{-1}}$. To obtain an average distance for the emission, we approximate the bubbles as 2 spheres centered at $b = \pm 28^\circ$, and directly above and below the Galactic center. For a Sun-GC distance of 8.5 kpc, this implies a distance of 9.6 kpc, and a total power (both bubbles) in the $1 - 100$ GeV band of $2.5{\times}10^{40}$ GeV/s or 4.0×10^{37} erg/s, which is $\sim 5\%$ of the total Galactic gamma-ray luminosity between $0.1 - 100$ GeV (Strong et al. 2010).

The electron cosmic-ray density in the bubbles required to generate the observed gamma rays, at any given energy, depends strongly on the assumed electron

spectrum. However, typically the required values are comparable to the locally measured electron CR density. For example, for the model in the first panel of Figure 3.7 ($dN/dE \propto E^{-2}$ for 500 GeV $\leq E \leq$ 700 GeV), the inferred bubble electron density is $\sim 10\times$ greater than the local electron density (as measured by *Fermi*) at an energy of 500 GeV. For a representative model from the first panel of Figure 3.6 ($dN/dE \propto E^{-2.3}$ for 0.1 GeV $\leq E \leq$ 1000 GeV, with a 10 μG magnetic field generating the WMAP Haze via synchrotron), at 500 GeV the bubble electron density is a factor $\sim 2\times$ greater than the local density.

3.5 Interpretation

As discussed in Dobler et al. (2010), the *Fermi* bubbles seem most likely to originate from IC scattering, since the required electron CR population can also naturally generate the *WMAP* haze as a synchrotron signal. The *ROSAT* X-ray measurements suggest that the bubbles are hot and hence *underdense* regions, and thus argue against the gamma rays originating from bremsstrahlung or π^0 decay.

Even though the material in the bubbles is likely high pressure, it is also probably very hot ($\sim 10^7$ K) and has lower gas density than the ambient ISM. This would explain why the *ROSAT* 1.5 keV map shows a "cavity" of soft X-rays toward the center of the *Fermi* bubble structure, like the X-ray cavity in galaxy clusters (McNamara & Nulsen 2007), especially in the north *Fermi* bubble. Furthermore, allowing the *Fermi* bubbles to have lower density than the ambient medium means they would experience a buoyant force moving the bubble material away from the GC (see Chapter 4.1.2 for further discussion), which may help generate the

observed morphology. Because π^0 and bremsstrahlung gamma-ray emission both scale as the CR density $\times$ the gas density, an underdense region cannot be brighter unless the cosmic ray densities are greatly increased to compensate; for protons, in particular, the propagation lengths are great enough that a proton overdensity cannot reasonably explain the sharp bubble edges observed in the data, if the bubbles are in a steady state.

If the bubbles are expanding rapidly and highly accelerated protons responsible for the gamma-ray emission are trapped behind shock fronts, then sharp edges for the *Fermi* bubbles could occur naturally. However, in the presence of such a shock, electrons would also be accelerated, and would generally produce more gamma-rays than the protons via ICS (since the cooling time for electron CRs is much shorter than the cooling time for proton CRs of comparable energy).

It might be thought that the presence of a bright X-ray edge could lead to a sharp edge in the gamma-ray signal, via IC scattering of electron CRs on the X-ray photons. In the Thomson limit, the energy of IC scattered photons is of order $(\Gamma_e/2)E_e$, with $\Gamma_e = 4E_eE_\gamma/m_e^2$ (where E_γ and E_e are the initial photon and electron energies, respectively, and m_e is the electron mass), and the scattering cross section is independent of the initial electron and photon energies. Thus a higher-energy photon population, leading to a larger value of Γ_e, allows IC gamma-rays at a given energy to originate from lower-energy electrons, which are much more abundant for typical electron spectra with $dN/dE \sim E^{-\gamma}$, $\gamma \gtrsim 2$. However, in the Klein-Nishina regime where $\Gamma_e \gtrsim 1$ this picture changes: the energy of scattered photons is determined mostly by the energy of the initial electron, and the cross section scales as $1/\Gamma_e$. Scatterings of ~ 50 GeV electrons already produce ~ 10 GeV gamma rays; when

compared to the scattering of 10 GeV electrons on X-rays in the extreme KN limit, the KN suppression of the cross section in the latter case more than counteracts the greater abundance of ~ 10 GeV electrons, unless the electron spectrum is very soft (which is inconsistent with the observed signal).

Thus hard UV or X-rays in the bubbles, which might be naturally expected in a high-temperature region, would *not* make the IC spectrum harder, and IC scattering on these photons is subdominant to IC scattering on the usual ISRF for the electron energies in question, unless the X-ray photon number density is much *greater* than the starlight photon number density. Furthermore, there is no reason to think the bubbles contains more $\lesssim 1$ eV photons, at least not in a region with a well defined spatial edge. Thus the sharp edges of the *Fermi* bubbles, and the non-uniformity in the emissivity, most likely arise from the electron CR density rather than the photon density. The presence of similar sharp edges in the *WMAP* haze (at $|b| \leq 30^\circ$) supports this hypothesis, if the *WMAP* haze is attributed to synchrotron radiation from the electron CRs.

Similarly, the elongated shape of the *Fermi* bubble structures perpendicular to the Galactic plane suggests that the electron CR distribution itself is extended perpendicular to the plane. The *Fermi* bubble morphology is a strong argument against the possibility that the *WMAP* haze originates from a disk-like electron distribution with significant longitudinal variation of the magnetic field, as suggested by Kaplinghat et al. (2009).

The limb brightening of the X-rays in the *ROSAT* data (as shown in Figure 3.2), and the flat intensity profile of the *Fermi* bubbles, suggest the presence of a

shell or shock, with increased electron CR density, coinciding with a hot thermal plasma. If the ambient medium several kpc above and below the GC were neutral, then bubbles of ionized gas could produce a void in the H I map. In the *top row* of Figure 3.9, the *left* panel shows the half sky Haslam 408 MHz map (Haslam et al. 1982a) with $-90^\circ < \ell < 90^\circ$, the *middle* panel subtracts a simple geometric disk template (shown in the *bottom left* panel) to better reveal the structures deeper into the Galactic plane. The *right* panel is the same as the *middle* panel but overplotted with the *Fermi* bubbles, the *northern arc*, and the *Loop I* features identified from the $1-5$ GeV *Fermi* gamma-ray map (see Figure 2.4). The *Loop I* feature (*red dotted line*) align with the extended diffuse features in the Haslam 408 MHz synchrotron map (known as *North Polar Spur*). The inner and outer edges of the *northern arc* (*dashed blue lines*) overlap with two arcs in the Haslam synchrotron map. However, the *Fermi* bubbles have no apparent counterparts in this map. For the *second row*, it is the same as the *top row*, but for the Leiden/Argentine/Bonn (LAB) Survey of Galactic H I (Kalberla et al. 2005). The *middle* panel subtracts a simple disk template shown in the *bottom middle* panel to better reveal structures towards the GC. No apparent features have been identified that correlate with the *Fermi* bubbles and other features in $1-5$ GeV *Fermi* map (there may be some faint filaments morphologically tracing the gamma-ray features). In the *third row* we show the same as the *top row* but for the Hα map (Finkbeiner 2003). The *middle* panel subtracts a simple disk template shown in the *bottom right* panel to reveal more structures in the inner Galaxy. No corresponding features have been identified morphologically similar to the structures in the $1-5$ GeV *Fermi* gamma-ray maps (color line in the *right* panel). In summary, we see no evidence for features aligned

with the bubbles in these maps, suggesting that the H I map in this part of the sky is dominated by disk emission, and has nothing to do with the bubbles. If the bubbles are in a static state, the bubble edges should have lower temperature than the bubble interior and thus higher gas density, although shocks or MHD turbulence might lead to higher temperatures at the bubble wall. The X-rays in *ROSAT* may be thermal bremsstrahlung emission, so the emissivity is proportional to the thermal electron density $\times$ ion density. They could also arise from charge exchange reactions occurring when the high-speed gas in the bubbles collides with the denser gas at the bubble edge (see Snowden 2009, and reference therein); this mechanism could explain the pronounced limb brightening of the X-rays. As an alternative explanation, the *ROSAT* X-ray feature might be synchrotron emission from *very high* energy electron CRs. Typically, though, one needs ~ 50 TeV (~ 5 TeV) electrons with ~ 10 μG (1 mG) magnetic field to produce ~ 1 keV synchrotron photons.

The *Fermi* bubble features do *not* appear to be associated with *Loop I*, a giant radio loop spanning over 100 degrees (Large et al. 1962), which is thought to be generated from the local *Sco-Cen* OB association. Detections of *Loop I* in high-energy gamma-rays have been claimed by Bhat et al. (1985) and also recently by *Fermi* (Casandjian et al. 2009); we have also discussed its presence in Chapter 2.2.2.

The *Loop I* gamma-rays may be the IC counterpart of the synchrotron emission seen in the Haslam 408 MHz map, although some of the emission might be π^0 gammas associated with H I (Figure 3.9). We compare structures identified from the *Fermi* $1-5$ GeV maps with *Loop I* features in the Haslam 408 MHz map in the *top row* of Figure 3.1, and see that the *Fermi* bubbles are spatially distinct from the

arcs associated with *Loop I*; as we have shown in Figure 2.16, the *Loop I* correlated emission also has a softer spectrum than the *Fermi* bubble emission. The *Loop I* feature in the *ROSAT* map similarly has a softer spectrum than the limb-brightened X-ray bubble edges: as shown in Figure 3.3, when a low-energy map is subtracted from a higher-energy map in such a way that *Loop I* vanishes, the bubble edges remain bright. We also see additional shell structures which follow the *Fermi* bubble edges and the *northern arc* in the Haslam 408 MHz map (*top row* of Figure 3.9).

The *Fermi* bubbles are morphologically and spectrally distinct from both the π^0 emission and the IC and bremsstrahlung emission from the disk electrons. As we have shown in Figure 2.12 to Figure 2.17, the *Fermi* bubbles have a distinctly hard spectrum, $dN_\gamma/dE \sim E^{-2}$, with no evidence of spatial variation across the bubbles. As shown in Figure 3.6, an electron population with $dN_e/dE \sim E^{-2-2.5}$ is required to produce these gamma rays by IC scattering: this is comparable to the spectrum of electrons accelerated by supernova shocks or polar cap acceleration (Biermann et al. 2010). However, diffusive propagation and cooling would be expected to soften the spectrum, making it difficult to explain the *Fermi* bubbles by IC scattering from a steady-state population of these electrons (a single brief injection of electrons with $dN/dE \sim E^{-2}$ could generate a sufficiently hard spectrum for the bubbles *if* there was a mechanism to transport them throughout the bubble without significant cooling). The facts strongly suggest that a distinct electron component with a harder spectrum than steady-state SNR generated electrons is responsible for the *Fermi* bubbles and associated signals in the *WMAP* and *ROSAT* data.

It has been suggested that a large population of faint millisecond pulsars (MSPs) in the Milky Way halo could contribute to the *WMAP* and *Fermi* haze

signals, via both pulsed gamma-ray emission and e^+e^- production (Malyshev et al. 2010). With a halo population of 3×10^4 MSPs, roughly half of the spin-down power going into e^+e^- pairs and $\sim 10\%$ going to pulsed gamma-rays, consistency with both the *WMAP* data and the first-year *Fermi* photon data is possible; however, this model does not immediately explain either the rather sharp edge in the distribution of gamma-ray emission, or the features in the *ROSAT* X-ray data (the same can of course be said for models which generate the hazes via dark matter annihilation or decay). Other attempts to explain the *WMAP* haze with pulsars have generally employed a disk population of pulsars, either peaking in the GC or peaking at small Galactocentric radius but going to zero in the GC (Kaplinghat et al. 2009; Harding & Abazajian 2010); such models have difficulty explaining the spherical morphology of the haze. Furthermore, as pointed out by McQuinn & Zaldarriaga (2010), the regression of the 408 MHz Haslam map should remove much of the contribution from young pulsars in the *WMAP* data, since young pulsars have a similar spatial distribution to supernovae.

How could the electron CRs possess the same hard spectrum everywhere within the bubble and extend up to 10 kpc, while experiencing a steep fall-off at the bubble edge? A large population of CRs might be entrained in large scale Galactic outflows from the GC and enrich the bubbles (see more discussion in Chapter 4.1.3). CRs could be produced along with jets, or shock accelerated CRs from magnetic reconnection inside the bubble or near its surface (see more discussion in Chapter 4.2). However, it is challenging to produce a flat intensity profile for the bubble interior with a sharp edge. The ambient gas should be compressed to a higher density on the shell by shocks (probably also enhancing the magnetic field), and

brighter synchrotron emission on the shell would then be expected, but the haze emission observed in *WMAP* is not limb-brightened and shows no evidence for a shell of finite thickness (although we do see shell structure in the X-rays). A cartoon picture summarizing the morphology of the *Fermi* bubbles and associated signals at other wavelengths is shown in Figure 4.1.

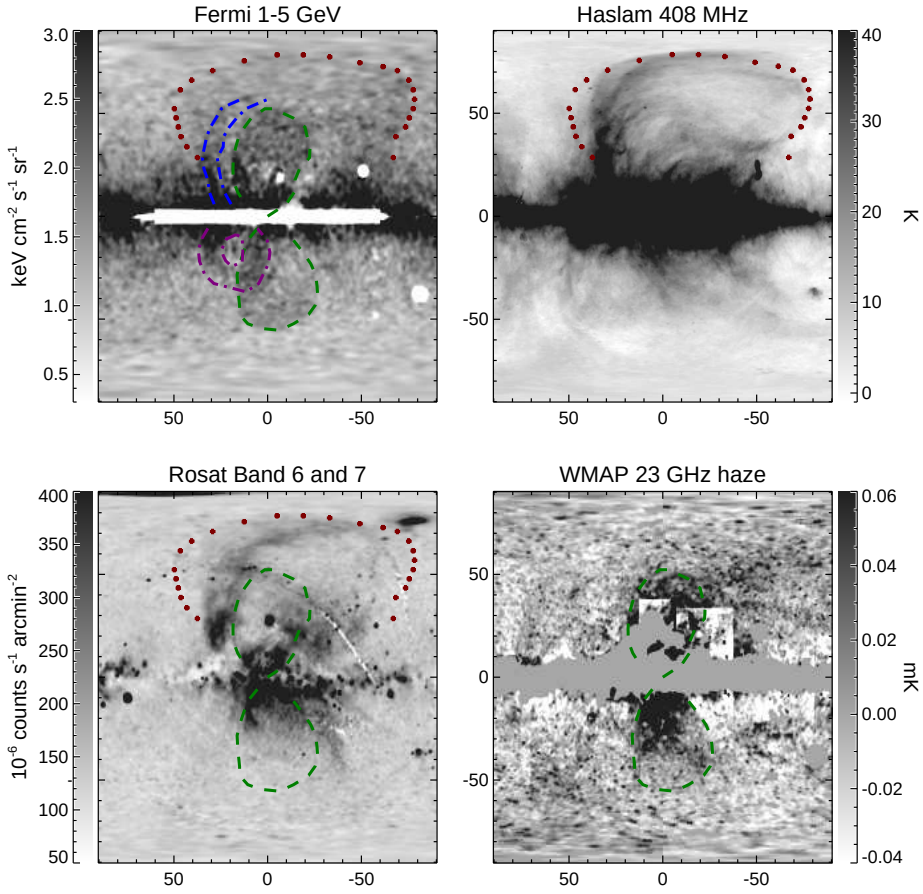

Figure 3.1.— Comparison of the *Fermi* bubbles with features in other maps. *Top left:* $1-5$ GeV *Fermi*-LAT 1.6 yr map with north and south bubble edges marked with green dashed line, and *north arc* in blue dashed line. The approximate edge of the *Loop I* feature is plotted in red dotted line, and the "donut" in purple dot-dashed line. *Top right:* The Haslam 408 MHz map overplotted with the same red dotted line as the *top left* panel. The red dotted line remarkably traces the edge of the bright *Loop I* feature in the Haslam soft synchrotron map. *Bottom left:* the *ROSAT* 1.5 keV X-ray map is shown together with the same color lines marking the prominent *Fermi* bubble features. *Bottom right: WMAP* haze at K-band overplotted with *Fermi* bubble edges.

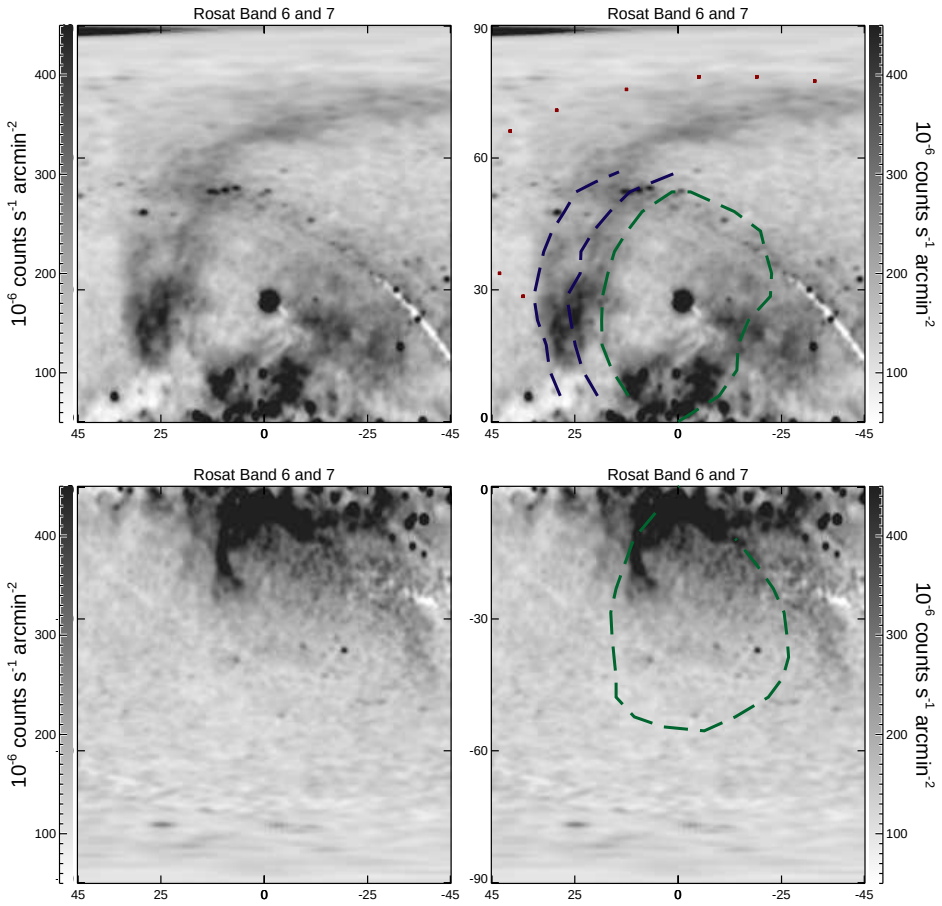

Figure 3.2.— *Top left:* The *ROSAT* X-ray haze features compared with the *Fermi* bubbles' morphology. *Top row:* The X-ray features of *ROSAT* band 6 and 7 in the north sky towards to the GC (*left* panel) compared with *Fermi* north bubble overplotted with green dashed line, *northern arc* feature in blue dashed line, and *Loop I* feature in red dotted line (*right* panel). *Bottom row:* Same as *top row* but for the south bubble features.

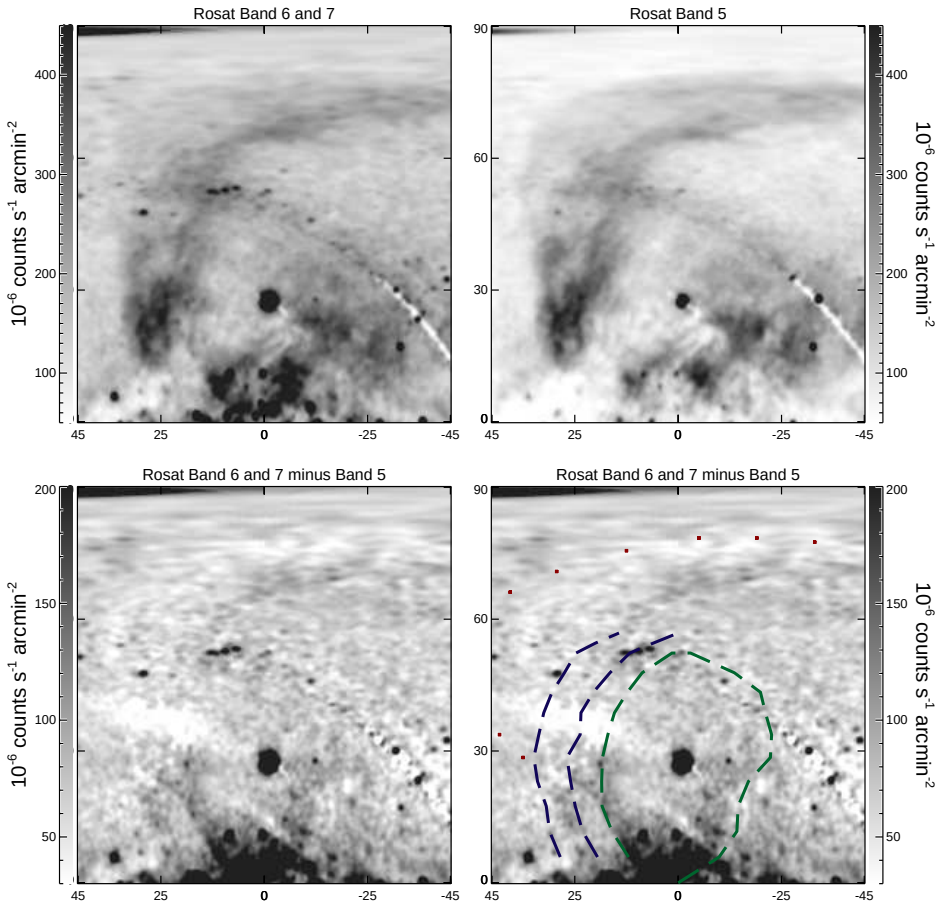

Figure 3.3.— *Top left:* The *ROSAT* X-ray features in Band 6 and 7. *Top right:* The same region as the *left* panel, but for the *ROSAT* X-ray map in band 5. *Bottom left:* The residual X-ray features after subtracting the *top right* softer Band 5 map from the *top left* harder Band 6 and 7 map. *Bottom right:* The same as the *bottom left* panel, overplotted with the *Fermi* bubble features, the *northern arc*, and *Loop I* features. The residual X-ray features with harder spectrum than the diffuse *Loop I* feature align well with the *Fermi* bubble structures.

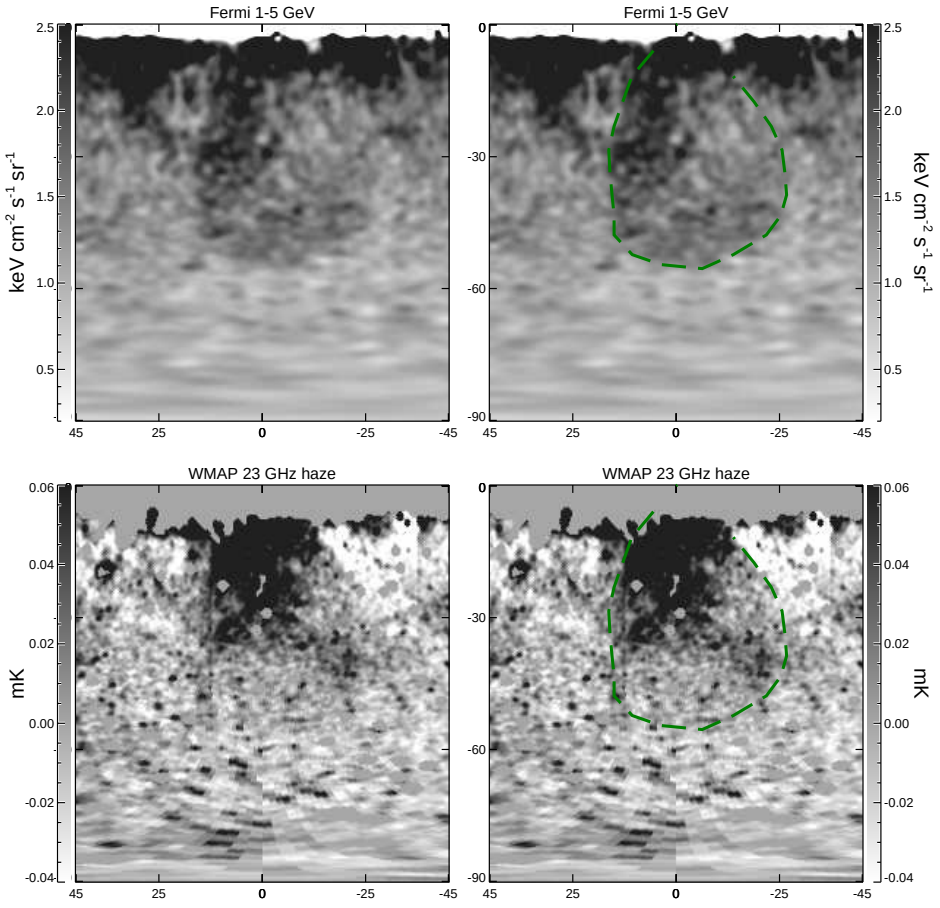

Figure 3.4.— The *Fermi* bubbles at $1-5$ GeV (the residual map obtained by subtracting the SFD dust map and the disk template) compared with the *WMAP* K-band (23 GHz) haze (Dobler & Finkbeiner 2008). *Top row:* The $1-5$ GeV map with $\ell = [-45°, 45°]$ and $b = [-90°, 0°]$ (*left* panel) with the *Fermi* south bubble edge overplotted in green dashed line (*right* panel); the same as the left column third row panel of Figure 2.3. *Bottom row:* Same sky region as *top row* but displaying the *WMAP* haze at 23 GHz (*left* panel), with the *Fermi* south bubble edge overplotted in green dashed line (*right* panel).

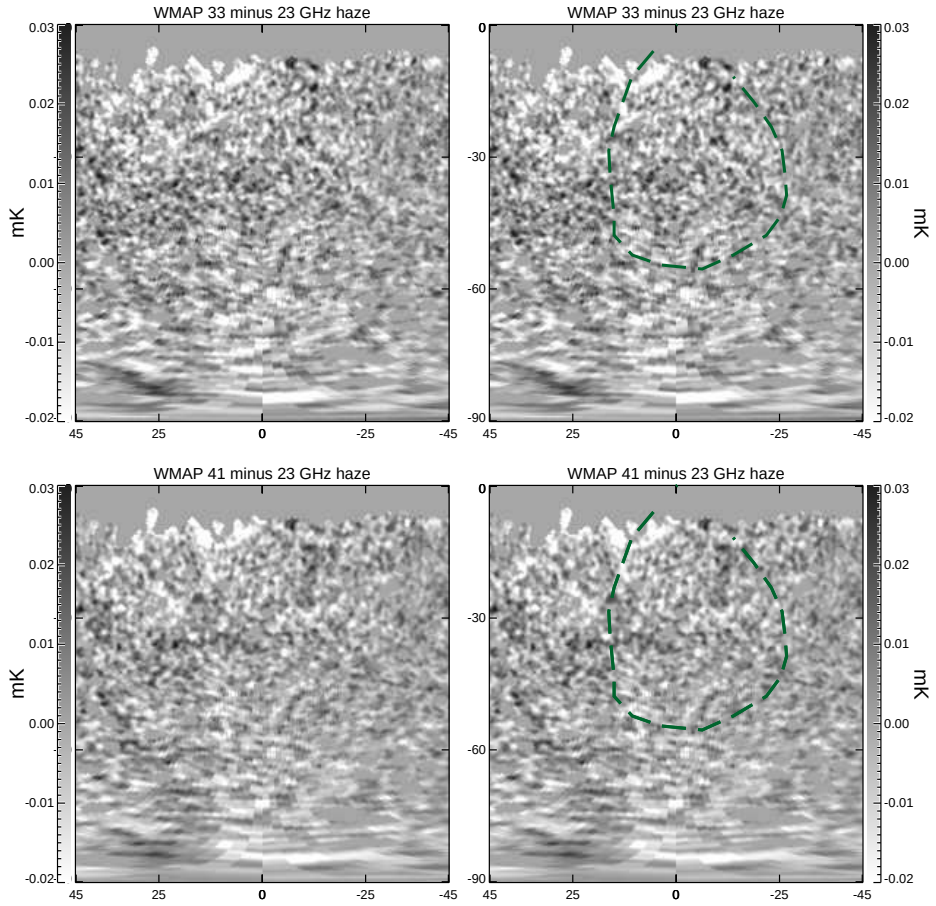

Figure 3.5.— Difference maps of the *WMAP* haze. *Top row:* The difference map between the 23 GHz *WMAP* haze and 33 GHz *WMAP* haze. The *right* panel is the same as the left but overplotted with the south *Fermi* bubble edge in green dashed line. *Bottom row:* The same as the *top row*, but showing the difference between the 41 GHz *WMAP* haze and 33 GHz *WMAP* haze. We see no apparent structure in the difference maps, indicating a consistent spectrum across different (spatial) regions of the haze.

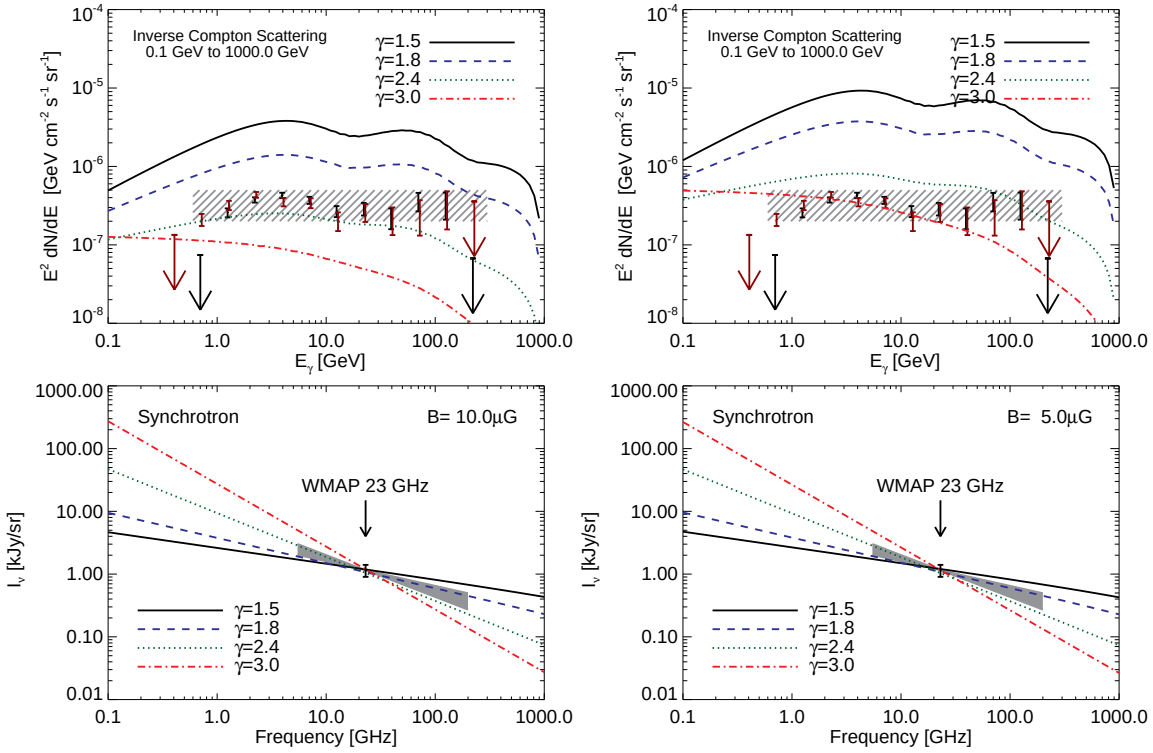

Figure 3.6.— The estimated spectrum of IC gamma rays (*upper panel*) and synchrotron radiation (*lower panel*) originating from a hard electron spectrum along a line of sight 4 kpc above the Galactic center (i.e. $b \approx 25°$). The steady-state electron spectrum is taken to be a power law, $dN/dE \propto E^{-\gamma}$, with index $\gamma = 1.5$ (*solid black*), 1.8 (*blue dashed*), 2.4 (*green dotted*), and 3.0 (*red dash-dotted*). In all cases the spectrum has a range of [0.1, 1000] GeV.

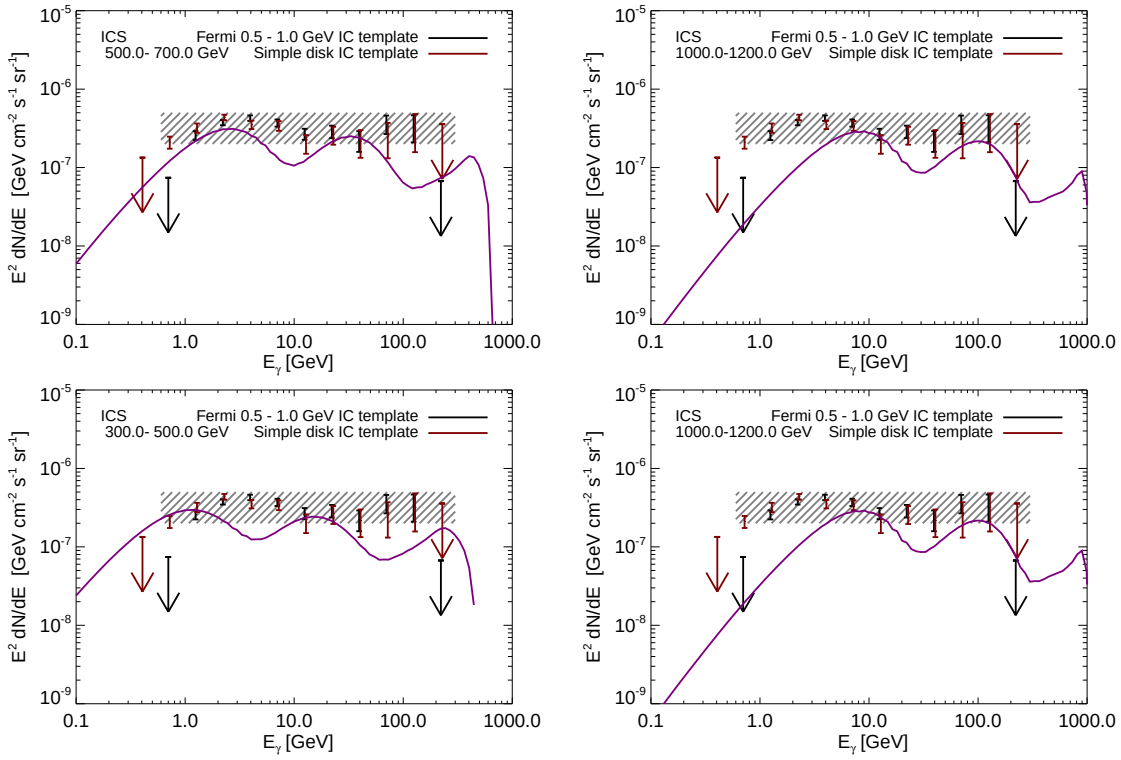

Figure 3.7.— The estimated spectrum of IC gamma rays originating from a hard electron spectrum ($dN/dE \propto E^{-2}$) with a limited energy range, as in the *top row* of Figure 3.6, but with different minimum and maximum energies. The normalization of the ICS signal is fitted to the data. The three peaks are from ICS of the CMB (left peak), FIR (middle peak), and optical/UV interstellar radiation field. The ISRF model is taken from `GALPROP` version 50p. A hard electron CR population with a low energy cutoff at about 500 GeV can fit the data better than a power law electron spectrum extending from 0.1 GeV to 1000 GeV (see Figure 3.6).

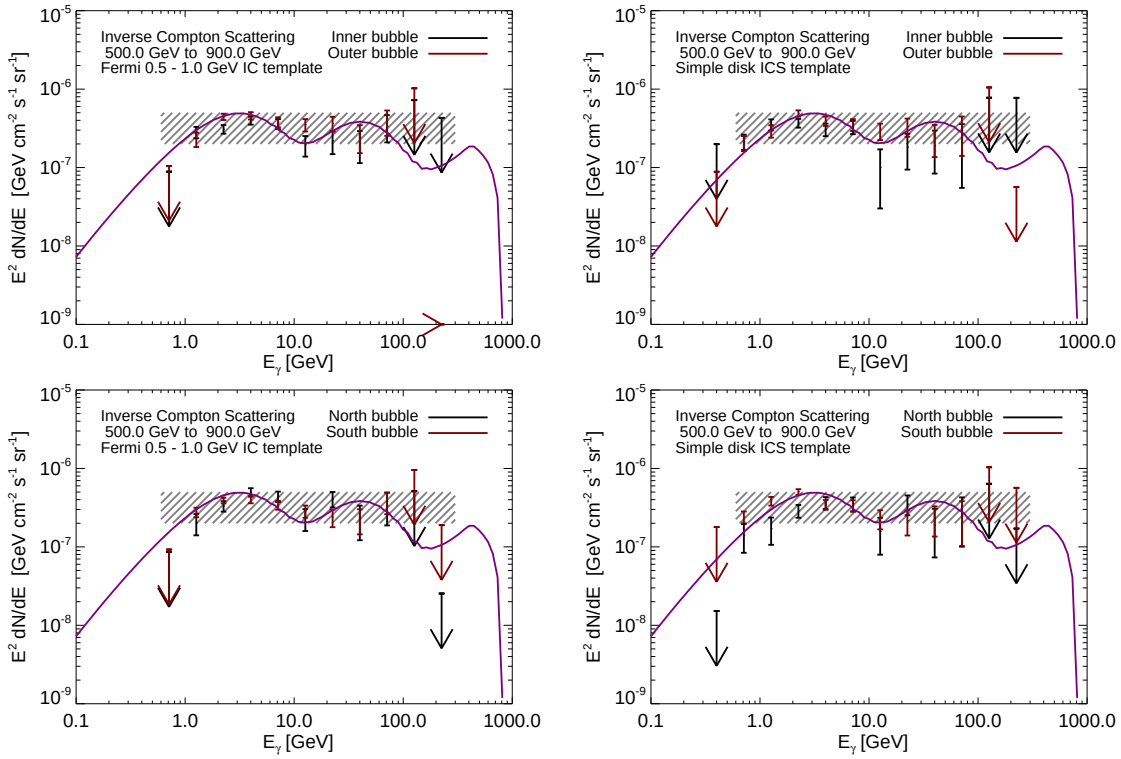

Figure 3.8.— The estimated spectrum of IC gamma rays originating from a hard electron spectrum, the same as Figure 3.7, but for the $500 - 900$ GeV energy range. *Top row:* data points show the separately fitted spectra for the bubble interior and outer shell templates (as defined in Figure 2.15), with the template for the disk IC emission given by (*left* panel) the $0.5 - 1$ GeV *Fermi* map with dust-correlated emission subtracted, and (*right* panel) the simple geometric disk model defined in Figure 2.3. *Bottom row:* as top row, but showing the separately fitted spectra for the north and south *Fermi* bubbles (as defined in Figure 2.15).

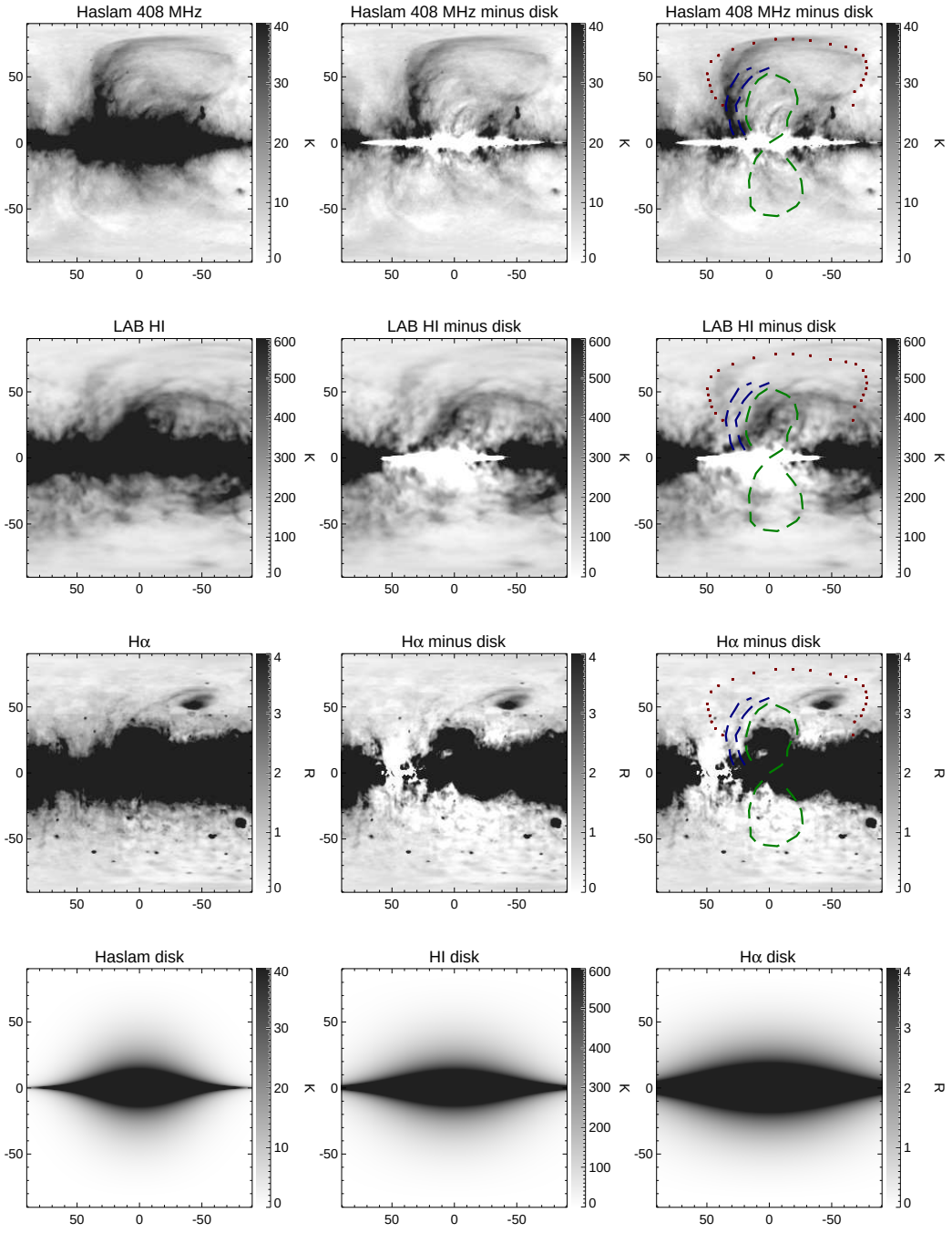

Figure 3.9.— *Fermi* bubble features in other maps.

Chapter 4

Models and Discussions

4.1 The origin of the bubble structure

As we have shown in Chapter 2.2, the bilobular *Fermi* bubble structures are apparently well centered on $\ell = 0°$, and symmetric with respect to reflection across the Galactic plane (*bottom row* in Figure 2.3). The bubbles extend down to the plane, where they appear even closer to $\ell = 0°$. This alignment and north-south symmetry are unlikely unless the bubbles originate from the GC, and motivate explanations involving Massive Black Hole (MBH) activity (Chapter 4.1.2) or recent starbursts towards the GC (Chapter 4.1.3). We note that Sco X-1 is approximately centered on the north bubble at the present, but this appears to be a coincidence. Given the similarity between the northern and southern bubbles and the absence of any similar feature in the south, we believe the *Fermi* bubbles have a GC origin.

While the origin of the *Fermi* bubbles is unknown, a rough estimate can be

made for their age and the total energy required (although the latter quantity depends linearly on the gas density in the bubbles, which is poorly constrained). From the *ROSAT* data, we envisage the bubbles as hot low density ($n \sim 10^{-3}\,\mathrm{cm}^{-3}$) cavities filled with $\sim$ 2 keV gas, with (from the *Fermi* data) height $\sim$ 10 kpc, expanding at velocity $v \lesssim 10^3$ km/s: thus we estimate the energy of the *Fermi* bubbles to be about 10^{54-55} erg, with an age of $\sim 10^7 (v/1000\,\mathrm{km/s})^{-1}$ yr.

Energetic galactic outflows are common phenomena which have been found in both nearby and high redshift galaxies (Veilleux et al. 2005). Galactic winds are believed to have significant impact on galaxy formation, morphology, and their environments. The main sources of the energy are stellar winds, supernovae, and/or active galactic nuclei (AGN); CRs and magnetic field pressure can also help drive galactic outflows (Everett et al. 2010; Socrates et al. 2008).

In this Chapter we present some ideas for past activity in the GC that could help to generate the shape of the *Fermi* gamma-ray bubbles and the associated signals at other wavelengths. §4.1.1 presents and discusses evidence of past GC activity. §4.1.2 discusses the hypothesis that outflows from a black hole accretion event, including possible AGN jets, could form the *Fermi* bubbles. §4.1.3 focuses on the possibility of a previous starburst phase of the Milky Way, with the *Fermi* bubbles being inflated by the subsequent energetic Galactic wind.

4.1.1 Observational Evidence of Previous GC Activity

Observations across the electromagnetic spectrum have provided constraints on dynamics and evolution of the central gas and stellar populations, and current and

prior accretion activity of the central MBH. We highlight some of the evidence of previous activities towards the GC, which may relate to the production of the *Fermi* bubbles.

X-ray Reflection Nebulae in the GC There are indications of previous GC activity from X-ray echoes and time variability of reflected X-ray lines from cold iron atoms in molecular clouds around Sgr A* including Sgr B1 and B2, Sgr C, and M0.11-0.11 (Sunyaev et al. 1993; Sunyaev & Churazov 1998). The changes in the intensity, spectrum, and morphology of the fluorescent iron nebulae near the GC, observed by *ASCA* and *INTEGRAL* are likely due to reflected X-ray emission from previous activity of Sgr A* with high luminosity ∼300 yr ago. The outburst luminosity has $\sim 1.5\times10^{39}$ erg s^{-1} in $2-200$ keV with a power law spectrum $dN/dE \propto E^{-\gamma}$ with γ=1.8±0.2 (Ponti et al. 2010; Revnivtsev et al. 2004; Nobukawa et al. 2008). The changes in the intensities and morphologies of hard X-ray nebulosities on parsec scales have been discovered (Muno et al. 2007).

Outflows: Galactic Center Lobe and Expanding Molecular Ring Sofue (2000b) and Bland-Hawthorn & Cohen (2003b) have previously noted the presence of the extended bipolar structure in the *ROSAT* data, and have attributed it to a large-scale bipolar wind, powered by a starburst in the GC. In this picture, overpressured bubbles rise and expand adiabatically away from the injection region in the Galactic plane, driving shocks into the surrounding gas by ram pressure. Reflection of the shocks increases the density and temperature of the post-shocked gas, which has been suggested to have $T \approx 5 \times 10^6$ K and $n \approx 0.1$ cm^{-3} at 2

kpc above the plane (Bland-Hawthorn & Cohen 2003b). Free-free emission in the resulting high-temperature plasma produces the observed X-ray signals. The Galactic Center Lobe (GCL) on *degree* scale has estimated total kinetic energy $\sim 10^{55}$ erg and a dynamical time scale of $\sim 10^6$ yr. The size, energy, and time scales are similar to those of the expanding molecular ring (EMR) around the GC (Kaifu et al. 1972; Scoville 1972; Totani 2006). Sofue (2000b) interpreted the North Polar Spur (NPS) with tens of degrees scale to be an outflow from the GC with energy scale of $\sim 10^{55-56}$ erg and time scale of $\sim 10^7$ yr. Totani (2006) suggested that all these outflows can be attributed to the past high activity of Sgr A* of a duration of $\sim 10^7$ yr, comparable to the reasonable estimation of the lifetimes of AGNs.

Diffuse X-ray Emission Muno et al. (2004) studied the diffuse X-ray emission within ~ 20 pc of the GC in detail using *Chandra* observations. The hard component plasma with $kT \sim 8$ keV is spatially uniform and correlated with a softer component with $kT \sim 0.8$ keV. Neither supernova remnants nor W-R/O stars are observed to produce thermal plasma hotter than $kT \sim 3$ keV. A $kT \sim 8$ keV plasma would be too hot to be confined to the GC and would form a plasma wind. A large amount of energy input $\sim 10^{40}$ erg/s is required to sustain such hot plasma. If the hot plasma is truly diffuse, the required power is too large to be explained by supernova explosions and the origin of this hot plasma, and might be explained as a result of shock heating by the wind or AGN activities. Similar diffuse hard X-ray emission has been detected from the starburst galaxy M82 (Strickland & Heckman 2007). However, Revnivtsev et al. (2009) have resolved ~ 80 percent of the hard diffuse gas into faint point sources.

Bipolar Hard X-ray in the GC *Chandra* observations show the morphology of hot gas with a few keV seems to be bipolar with each lobe extending to ∼10 pc (see Markoff 2010, and reference therein). Three explanations have been suggested for the origin of the lobes: thermal wind from the central cluster of massive young stars, steady outflows from Sgr A*, or repeated episodic outbursts from Sgr A*(Markoff 2010). For the collective stellar wind interpretation, it is unclear why the lobes only extend up to 10 pc which has a estimated flow time $\sim 3 \times 10^4$ yr, whereas the star cluster is $\sim$ 6 millon years old. Moreover, discrete blobs have been found within the lobes, and quasi-continuous winds are hard pressed to explain the origin of the blobs. The possibility of a transient jet-like feature is intriguing. The jets can be produced by accreting the debris of tidal disruption stars (see Chapter 4.1.2 for more discussion).

OB Stellar Disk There are two young star disks that have been identified in the central parsec of the GC (Paumard et al. 2006). *In situ* star formation from dense gas accretion disks is favored over the inspiraling star cluster scenario (see e.g. Bartko et al. 2009). The gas disks could be formed as a consequence of a large interstellar cloud captured by the central MBH, which then cooled and fragmented to form stars. Interestingly, the two star formation events happened near-simultaneously about 6 ± 2 Myr ago and the two disks are coeval to within $\sim$ 1 Myr (Paumard et al. 2006) and little activity has occurred since. The two young massive star clusters *Arches* and *Quintuplet* in the central 50 pc, with similar stellar mass, content and mass functions, were formed $\sim 10^7$ yr ago. It has been suggested in Paumard et al. (2006) that a global event may cause an increase in the rate of star formation, such

as a passing satellite galaxy that enhanced the clouds' collision frequency and may also provide the gas for active star formation.

The unique characteristics of stellar clusters towards the GC have been used to explain the origin of the magnetized nonthermal radio filaments, threads, and streaks (LaRosa et al. 2004; Yusef-Zadeh et al. 2004). Collective winds of massive W-R and OB stars within such a dense stellar environment can produce terminal shocks that accelerate relativistic particles. The abundance and characteristics of these nonthermal radio filaments within the inner 2 degrees of the GC region can be evidence of an earlier starburst (Rosner & Bodo 1996). Yusef-Zadeh & Königl (2004) propose a jet model in which the characteristics common to both protostellar and extragalactic jets are used to explain the origin of nonthermal filaments in the Galactic center region.

4.1.2 Outflow from Black Hole Accretion Events

The central MBH in our Milky Way, with an estimated mass of $M_{BH} \sim 4 \times 10^6$ $M_\odot$ (e.g. Ghez et al. 2008; Gillessen et al. 2009), is currently quiescent, radiating at about 9 orders of magnitude lower than the Eddington luminosity ($L_{Edd} \sim 10^{44}$ erg/s). The X-rays of Sgr A* is weak and thermal, in contrast to the hard nonthermal power law typically observed in most low-luminosity active galactic nuclei (LLAGN; see e.g. Ho 2008). Fast X-ray flaring of Sgr A* via nonthermal processes has been discovered by *Chandra* ACIS observation (Baganoff et al. 2003). The observed submillimeter/IR bump is seen to flare simultaneously with the X-rays. Due to the short timescale of the flares and the lack of evidence of any standard thin accretion disk emission

(Shakura & Sunyaev 1973), a magnetic origin of the flares has been suggested, either from synchrotron or synchrotron-self Compton emission (Eckart et al. 2004; Yusef-Zadeh et al. 2006; Dodds-Eden et al. 2009). Both radiative inefficient accretion flow (RIAF) models and outflow-dominated models have been invented (Falcke & Markoff 2000; Blandford & Begelman 1999; Yuan et al. 2002).

Clearly the MBH has not always been so underluminous: it may have experienced a long active state in the past few million or tens of million years through one or more accretion events, driving jets out of the disk, shocking the ambient material, producing both gamma-rays and CRs, and appearing more similar to normal low-luminosity AGN. If the MBH were radiating at the Eddington luminosity, it would take only $\sim 10^{3-4}$ years to reach the estimated energy of the *Fermi* bubbles; for a percent level Eddington accretion rate ($\sim 10^{42}$ erg/s), it would take $\sim 10^{5-6}$ yr, comparable to the estimated cooling time of the electron CRs.

Scenarios for MBH Jet Formation in the GC

Currently, the X-ray flares are the only unambiguous AGN-like activity that Sgr A* displays (Markoff 2010). However, the synchrotron radio emission is comparable to typical LLAGN with compact jets in terms of spectral characteristics. It is well known that jets associated with accretion disks surrounding black holes can efficiently generate high energy particles. BL Lacs can form relativistic jets to produce TeV gamma rays, as can microquasars. However, we know through multiwavelength observations that the central MBH in our Milky Way has an extraordinarily low bolometric luminosity of $\sim 10^{36}$ ergs/s, and so is currently in its quiescent dim state,

and no jets toward the GC have been physically resolved. Detailed examinations of the GCL have shown that the gas shell is deep into the disk, and do not support a jet origin for that structure (Law 2010). However, weak jets consistent with the spectrum of Sgr A* can be easily hidden by the blurring of their photosphere (Markoff et al. 2007).

The jets related to the energetic accretion in the GC can go in any direction along with the spin axis of the central massive black hole; they need not be aligned with the minor axis of the Galaxy. This mechanism does not obviously provide a natural explanation for the north-south symmetry of the *Fermi* bubbles, and the relatively flat gamma-ray intensity inside the bubbles. Also, there is as yet no conclusive evidence for the presence of jets toward the GC (Muno et al. 2008). However, CR rich wide jets might have existed in the past, and the *Fermi* bubbles might have been inflated by the jets in a relatively short time scale without significant cooling. Although the past AGN phase could be the primary heating source of the *Fermi* bubbles, the low density and momentum associated with the jets do not readily distribute the thermal energy isotropically, making it harder to explain the morphology and flat intensity of the *Fermi* bubbles. If a starburst phase in the GC coincided with the energetic jets, SNe in the starburst might provide a large injection of momentum and turbulence, which could help isotropize the energy distribution.

Accretion of Stars One way to form jets in the GC is for the MBH to tidally disrupt and swallow stars in the nuclear star cluster (Hills 1975; Rees 1988). The typical picture is that when a star trajectory is sufficiently close to the MBH, the

star is captured and disrupted by tidal forces, and after about an orbital timescale, a transient accretion disk forms from the debris of the disrupted star. The capture rate of the GC MBH has been estimated at $\sim 4.8 \times 10^{-5}\,\mathrm{yr}^{-1}$ for main-sequence stars and $\sim 8.5 \times 10^{-6}\,\mathrm{yr}^{-1}$ for red giant stars. Sgr A* could temporarily behave like an AGN and produce a powerful jet by accreting the debris of such stars, which may be ejected from surrounding molecular disks. If a 50 solar mass star is captured by the MBH in the GC, it gives an energy in relativistic protons as high as $\sim 10^{54-55}$ ergs on a very short timescale ($\sim 10^{3-4}$ yr), at a rate of about $\sim 10^{43}$ ergs/s.

Accretion of ISM Quasi-periodic starbursts in the GC have been recently suggested as a result of the interactions between the stellar bar and interstellar gas (Stark et al. 2004). In this scenario, gas is driven by bar dynamics toward the inner Lindblad resonance, and accumulates in a dense gas ring at 150 pc until the critical density threshold is reached. Then giant clouds can be formed on a short timescale, and move toward the center by dynamical friction. The timescale for this cycle to repeat is highly uncertain but is estimated to be of order 20 Myr (Stark et al. 2004).

Accretion of IMBH A single 10^4 solar mass BH spiraling in to the GC may also trigger starbursts and change the spin of the Sgr A*(Gualandris & Merritt 2009), thereby producing precessing jets. It has been argued that one such event happens approximately every 10^7 years in order to create a core of old stars in the GC, of radius 0.1 pc. Chandra has detected more than 2000 hard X-ray ($2 - 7$ keV) point sources within 23 pc of the GC (Muno et al. 2003). Some of them may harbor intermediate mass black holes. However, to our knowledge, no evidence of a

collimated outflow has been found from the GC. There may be aligned, VLBI-scale (∼1 pc in the GC) radio knots that have not been discovered.

Models of Past Enhanced Sgr A*Accretion Totani (2006) suggested a RIAF model of Sgr A* to explain both the past high X-ray luminosity and the kinetic luminosity of the outflows inferred from observations. The required boost factor of the accretion rate $\sim 10^{3-4}$ with a time scale of $\sim 10^7$ yr is naturally expected in the model. The induced outflow is energetic enough to support the hot (∼8 keV) plasma halo towards the GC. Such a model is claimed by Totani (2006) to better explain the positron production which is required to generate the 511 keV line emission towards the Galactic bulge observed by *INTEGRAL/SPI* (Weidenspointner et al. 2008).

Galactic Jets in Starburst Galaxies In other galaxies, powerful AGN radio jets interacting strongly with the hot gas have been observed (McNamara & Nulsen 2007). In relatively radio-quiet galaxies such as NGC 4636, NGC 708, and NGC 4472, (see e.g. Wang & Hu 2005, for a summary), faint X-ray "ghost" cavities appear without corresponding radio lobes. It has been suggested that capture of red giant stars and accretion onto the central MBH can power jets/outflows with typical energy $\sim 10^{56}$ ergs, which is the required energy to form the observed cavities.

Interferometric monitoring of the Seyfert galaxy NGC 3079 has found evidence of radio jet components undergoing compression by collision with the clumpy ISM, within a few pc of the central engine. This result supports the idea that the kpc-scale superbubble originates from the spread of the momentum of jets. The generalization of this scenario provides an explanation for why jets in Seyfert galaxies are not able

to propagate to scales of kpc as do jets in radio-loud AGN (Middelberg et al. 2007).

Precessing Jets Several processes may lead to jet precession, including magnetic torques, warped discs, and gravitational torques in a binary system (see e.g. Falceta-Gonçalves et al. 2010). If the momenta of the MBH and the accretion disk are not perfectly aligned, the Bardeen-Petterson effect could be a likely mechanism for precession (Bardeen & Petterson 1975), which will force the alignment of the disk and the MBH angular momentum.

Irwin & Seaquist (1988) suggested that the "bubble" structures that have been seen in nearby starburst galaxies could have been blown by a *precessing* VLBI-scale jet, a flat-spectrum radio core was recognized in NGC 3079 (Baan & Irwin 1995; Irwin & Sofue 1992). Typically, narrow, relativistic and non-precessing jets can carve out a hot gas bubble by interaction with ISM and release most of their energy far from the GC. Wide jets with large opening angles are capable of transferring momentum into a larger area resulting in the inflation of fat bubbles (also for precessing AGN jets see Sternberg & Soker 2008).

Shocked Shells Driven by AGN Jet

Relativistic jets dissipate their kinetic energy via interactions with the ISM. Jets in radio-loud AGN can inflate a bubble composed of decelerated jet matter which is often referred to as a cocoon. Initially, the cocoon is highly overpressured against the ambient ISM and a strong shock is driven into the ambient matter. Then a thin shell is formed around the cocoon by the compressed medium. The shells are

expected to be a promising site for particle acceleration.

As a simple estimate of the dynamics of the expanding cocoon and shell, we assume the bubbles and shells are spherical, and also assume that the ambient mass density profile has a form of a power-law given by $\rho_a(r) = \rho_0(r/1\mathrm{kpc})^{-1.5}$, where ρ_0 is the mass density at $r = 1$ kpc. We further assume that the kinetic power of the jet, L_j, is constant in time. Under these assumptions, the dynamics can be approximately described based on the model of stellar wind bubbles. The radius of the shock is given by $R(t) \sim 6\rho_{0.01}^{-2/7} L_{42}^{2/7} t_7^{6/7}$ kpc, where $\rho_{0.01} = \rho_0/0.01 m_p$ cm^{-3}, $L_{42} = L_\mathrm{j}/10^{42}$ ergs s^{-1} and $t_7 = t/10^7$ yr. Taking the expected numbers for the *Fermi* bubbles, we get a approximate estimate of the bubble size. The total internal energy stored in the shell can be expressed as $E_\mathrm{s} \sim 0.1\, L_\mathrm{j} t$, implying that roughly 10% of the total energy released by the jet is deposited in the shell.

Buoyant Bubbles

X-ray images have revealed shock fronts and giant cavities, some with bipolar structure, in the inner regions of clusters, surrounded with X-ray emitting gas. It is believed that the power in radio jets is comparable to the energy required to suppress cooling in giant elliptical galaxies or even rich clusters (McNamara & Nulsen 2007).

The depressions in the X-ray surface brightness of the *ROSAT* map may themselves indicate the presence of empty cavities or bubbles embedded in hot gas, and could be interpreted as a signature of previous AGN feedback with hot outflows. For adiabatic or supersonic bubbles first inflated by AGN jets, once the bubble reaches pressure equilibrium with the surrounding gas, it becomes buoyant

and rises, because the mass density is lower in the bubble than in its surroundings. As the bubble moves away from the GC, toward regions with even lower density and pressure, it expands. The velocity at which the bubbles rise depends on the buoyancy and the drag forces.

The ISM is in turn pushed by the rising bubble, which causes a upward displacement behind the bubble called "drift". This trailing fluid can give rise to filaments of cool gas. There are indeed filamentary structures in the inner Galaxy in both H I and Hα maps. Their identification could support the buoyant bubble scenario.

4.1.3 Nuclear Starburst

Another possible source of dramatic energy injection is a powerful starburst in the nucleus. Starburst induced Galactic winds are driven by the energy released by supernova explosions and stellar winds following an intense episode of star formation, which create an over-pressured cavity of hot gas. The galactic wind fluid is expected to have an initial temperature within the starburst region in the range of 10^{7-8} K even if it has been lightly mass loaded with cold ambient gas (Chevalier & Clegg 1985). The ISM can be swept up by the mechanical energy of multiple SN explosions and stellar winds. Large-scale galactic outflows have been observed in starburst galaxies both in the local Universe and at high redshifts (Veilleux et al. 2005; Bland-Hawthorn et al. 2007). Starburst episodes near the GC have been discussed in (e.g. Hartmann 1995).

Morphology of Outflows in Starburst Galaxies

Starburst-driven galactic winds have been studied extensively in both multi-waveband observations and hydrodynamical simulations (Strickland & Stevens 2000; Veilleux et al. 2005).

AGN or starburst galaxies show bipolar outflows (Gallimore et al. 2006; Sharp & Bland-Hawthorn 2010). The total energy of the superwind has been estimated as $\sim 10^{55-56}$ ergs, comparable to the estimated energy of the *Fermi* bubbles. The *Spitzer* Space Telescope has found a shell-like, bipolar structure in *Centaurus A*, 500 pc to the north and south of the nucleus, in the mid-infrared (Quillen et al. 2006). The shell has been estimated to be a few million years old and its mechanical energy of 10^{53-55} erg depends on the expanding velocity. A small, few-thousand solar mass nuclear burst of star formation, or an AGN origin has been proposed to explain the formation of the shell.

Recently, Westmoquette et al. (2009) showed that ionized gas in the starburst core of M82 is dynamically complex with many overlapping expanding structures located at different radii, with compressed, cool, photo-ionized gas at the roots of the superwind outflow. Extra-planar warm H_2 knots and filaments extending more than $\sim$3 kpc above and below the galactic plane have also been found (e.g. Veilleux et al. 2009)

NGC 253 is one of the most famous nearby starburst galaxies and is similar to our Milky Way in its overall star formation rate, except for a starburst region toward the center of the galaxy with spatial extent of a few hundred pc. A galactic wind in NGC 253 was found in Hα (McCarthy et al. 1987). Strickland & Stevens

(2000) discussed the spatial structure in detail in X-ray. The wind reaches out to ∼9 kpc perpendicular to the disk. Filamentary structures as part of projected conical outflow are found in Hα and near-infrared H_2 emission. The relatively warm gas ($\sim 10^4$ K) exists close to the hot gas ($\sim 10^6$ K). The X-ray filaments tend to be located in inner regions compared to Hα, and are brighter where the Hα emissions are locally weak. The separation between the Hα and X-ray filaments is ∼70 pc. The spatial distributions of Hα and X-ray indicate that the inner Galactic wind has higher temperature than the outer part. The UV emission seems to form a shell around the X-ray emission (Bauer et al. 2008). VLBI and VLA observations of the nuclear region of NGC 253 at 22 GHz shows no detection of any compact continuum source on milliarcsecond scales, indicating no low-luminosity AGN in the central region of NGC 253. It seems that the starburst region is the most plausible explanation for the source powering the wind (Brunthaler et al. 2009).

The Mechanism of Galactic Winds

The energy and momentum transfer of the Galactic wind could be dominated by high thermal and/or ram pressure. Materials have been swept-up and entrained as part of the wind, and the wind fluid comprises merged SN ejecta and massive star stellar wind material with ambient gas from the starburst region. Two popular extrinsic feedback mechanisms have been suggested: thermally driven winds powered by core-collapse supernovae and momentum-driven winds powered by starburst radiation (Cox 2005).

On the other hand, the idea that CRs and magnetic fields can help to drive

galactic winds has been known for decades (Ipavich 1975; Breitschwerdt et al. 1991). For every core-collapse SN, about 10 percent of the energy release is converted into CRs ($\sim 10^{50}$ erg). These CRs interact with the magnetized ISM extensively and exchange momentum through Alfvenic disturbances: the characteristic mean free path for a CR proton in the starburst phase of the GC is $\sim$1 pc. The effective cross section for CR protons and nuclei interacting with the ambient gas is much higher than the Thomson cross section for electrons. The luminosity at which CR collisions with gas balance gravity is about 10^{-6} of the usual Eddington luminosity (Socrates et al. 2008).

Momentum wind outflowing galactic supershells can also be driven by Lyα radiation pressure around star-forming regions (Dijkstra & Loeb 2009). The supershell velocity can be accelerated to 10^{2-3} km/s, and it may even be able to escape from the host galaxy. The radii are predicted to be $r_{sh} = 0.1 - 10$ kpc, with ages $t_{sh} = 1 - 100$ Myr and energies $E_{sh} = 10^{53-55}$ erg.

However, the morphology of the galactic wind in nearby starburst galaxies inferred from synchrotron, Hα, and H I maps is asymmetric about both the galactic minor axis and galactic plane, which may suggest the inhomogeneous nature of the ISM. On the other hand, as we have shown, the north and south *Fermi* bubbles are approximately symmetric with respect to the galactic plane and the minor axis of the disk. The symmetric structure of the *Fermi* bubbles might indicate that they are not generated by subsequent interactions with ambient gas throughout the wind.

Furthermore, the typical speed of galactic winds is about $200 - 300$ km/s. It takes about 5×10^7 yr for CR electrons to reach 10 kpc, but we have not seen any

evidence of cooling in the gamma ray intensity and spectrum. We probably need a faster transport mechanism for CRs if they were generated from the GC. However, the higher the velocity of the wind which entrains the CRs, the greater the kinetic energy the wind contains. The estimated energy of the *Fermi* bubbles only includes thermal energy; if they are actually kinetic energy dominated, then the energy requirement to form the *Fermi* bubbles is even larger (Gebauer & de Boer 2009; Jokipii & Morfill 1987; Lerche & Schlickeiser 1982).

The estimated supernova rate in the NGC 253 starburst region is about 0.1/yr (Engelbracht et al. 1998). Assuming each supernova explosion releases 10^{51} erg, and 10 percent of the energy is transferred to heating the *Fermi* bubbles, this gives a rate of energy injection comparable to $\sim 10^{42}$ erg/s. The star formation activity in NGC 253 has been underway for about $20 - 30$ Myr, and is considered to be in a steady state for the CR transport, presumably with a smaller time scale (Engelbracht et al. 1998).

It is possible that although the center of our Milky Way is currently in its quiet phase, it was recently (in the past 10^7 yr) in a starburst phase similar to NGC 253 (Heesen et al. 2009). To our knowledge, however, there is no evidence of massive supernova explosions ($\sim 10^{4-5}$) in the past $\sim 10^7$ yr towards the GC, and no apparent Galactic wind features have been found in Hα, indicating no strong recent ($\sim 10^4$ yr) star formation activity.

Everett et al. (2008, 2010) compared the synchrotron and soft X-ray emission from large-scale galactic wind models to *ROSAT* and Haslam 408 MHz maps. They show that a CR and thermally-driven wind could consistently fit the observations

and constrain the launching conditions of the wind, including the launching region and magnetic field strength. The comparison of the gamma-ray prediction of the wind model with *Fermi*-LAT diffuse emission, especially to the *Fermi* bubbles might have important implications for the CR driven wind of our Milky Way.

Cosmic Rays from a Starburst

A central starburst might also generate the increased population of electron CRs in the GeV-TeV energy range required to produce the gamma-ray bubble signals. Starburst galaxies host a greatly increased rate of supernovae in the central region. The shocks from supernovae can merge and produce energetic galactic scale winds, and the enhanced population of supernova remnants is believed to accelerate CRs, resulting in orders of magnitude higher CR density than currently expected in the GC. It is likely that the GC exhibited comparable CR density in the past, with a starburst phase turned on by boosted formation of massive stars. As previously discussed, during this starburst phase the CR protons produced in the inner Galaxy scatter on the ISM with very short path lengths, producing gamma rays (via π^0 production and decay), and electron (and positron) CRs. Although the immediately-produced gamma-rays and high density gas and ISRF associated with the starburst phase would not be observable today, the secondary electrons might be leftover from the past active starburst phase, and could have been transported to $\sim$10 kpc by the magnetic field entrained in the Galactic winds. GeV and TeV gamma-rays have recently been detected in nearby starburst galaxies NGC 253 (Acero et al. 2009), M 82, and Large Magellanic Cloud (LMC), by *Fermi*-LAT (Abdo et al. 2010a), High Energy Stereoscopic System (H.E.S.S.) (Itoh et al.

2007) and VERITAS (Karlsson & for the VERITAS collaboration 2009), support the starburst galaxies as a rich source of high energy gamma-rays. If a transient starburst did occur in the GC of our Milky Way, and produced a large population of CRs responsible for the observed *Fermi* bubbles, and *WMAP* haze, what triggered and terminated the starburst phase is unclear.

If the CRs are driven by winds, the halo magnetic field can carry CRs along the field lines from the inner disk/bulge into the halo, which could help the CR electrons to reach 10kpc without significant diffusive softening of their spectrum. The vertical CR bulk velocity is typically hundreds of km/s, which is remarkably constant over the entire extent of the disk and for galaxies with different mass. In the standard picture, CRs can't stream faster than the Alfvén speed with respect to the static frame of the magnetic field, due to the well-known streaming instability (Kulsrud & Pearce 1969). Considering nearby starburst galaxies, the vertical CR bulk speed has been measured to be $v_{\rm CR} = 300 \pm 30\,{\rm km\,s^{-1}}$ for NGC 253. For a typical magnetic field strength of $B \approx 15\,\mu{\rm G}$ and a density of the warm gas of $n \approx 0.05\,{\rm cm^{-3}}$ leads to an Alfvén speed of $v_{\rm A} = B/\sqrt{4\pi\rho} \approx 150\,{\rm km\,s^{-1}}$ (Heesen et al. 2009). The super-Alfvénic CR bulk speed requires that the CRs and the magnetic field which is frozen into the thermal gas of the wind are advectively transported *together*. The measured CR bulk speed is the superposition $v_{\rm CR} = v_{\rm wind} + v_{\rm A}$.

In this picture, the spectrum of electrons injected in the starburst region might be harder than elsewhere in the Galaxy if the transient starburst phase led to a top-heavy mass function of stars. Magnetic turbulence in the GC could also be much stronger than in the Solar neighborhood: the stronger the turbulence, the faster CRs are transported, and the higher the transition energy at which synchrotron/ICS

losses overtake diffusive losses. It has been shown that the high star formation rate per area in the GC leads to short transport times (Becker et al. 2009).

Constraints on Recent Starburst Activity

If the *Fermi* bubbles were generated by previous starburst activity in the GC, we would expect to see many more supernova remnants towards the GC than have been discovered. Moreover, radioactive ^{26}Al (half-life $\sim 7.2\times10^5$ yr) is believed to be mainly produced by massive stars, supernovae, and novae in the Galaxy (Prantzos & Diehl 1996). ^{26}Al decays into ^{26}Mg, emitting a gamma-ray photon of 1808.65 keV. Observations of the spectrometer (SPI) on the *INTEGRAL* gamma-ray observatory seem to disfavor the starburst scenario: the Galaxy-wide core-collapse supernova rate has been estimated at 1.9 ± 1.1 per century from the flux of ^{26}Al gamma-rays (Diehl et al. 2006). Within its half-life, ^{26}Al can only travel $\sim$0.1 kpc with the typical Galactic outflow velocity of $\sim$ 100 km/s. One expects strong ^{26}Al gamma-ray emission concentrated towards the GC, with a flux comparable with the total gamma-ray flux from the disk, if the outflow was produced by a starburst (Totani 2006). However, such a strong concentration at the Galactic center is not found (Prantzos & Diehl 1996), indicating that the accretion activity of Sgr A* is more plausible as the origin of the mass outflow. Future observations of the ratio of the Galactic ^{60}Fe to ^{26}Al may provide better constraints on the starburst scenario.

4.1.4 Other Ways to Generate the Bubbles

The molecular loops in the GC could possibly be explained in terms of a buoyant rise of magnetic loops due to the Parker instability. For a differentially rotating, magnetically turbulent disk, such magnetic loops can easily be formed and rise out of the disk. The typical scale of such a loop is 1kpc (Machida et al. 2009).

4.2 The Origin of the Cosmic Rays

It is not necessary that the physical mechanism that creates the bubbles also injects the electron CRs responsible for the *Fermi* bubbles. It is possible that the bubble structures were formed earlier and the electron CRs were injected by an alternative mechanism that then lights up the bubble structure with gamma-ray emission. In this section, we would like to separate the CR production from the bubble formation, and address the spatial origin of the CRs.

In any case, the production mechanism should generate electron CRs inside the *Fermi* bubbles, and also prevent them from efficiently leaving the bubbles, in order to produce the observed "sharp edge". However, electrons with $\sim 10^2$ GeV diffuse on the order of 1 kpc before losing half their energy (McQuinn & Zaldarriaga 2010). Higher energy electrons lose energy more rapidly and so have shorter path lengths; if the gamma-ray emission from the bubbles is dominated by IC scattering from TeV-scale electrons injected inside the bubble, then the sharp edge of the bubbles may be natural. This would in turn imply that the gamma rays observed by *Fermi* are largely upscattered *CMB* photons (starlight and far

infrared photons are upscattered to much higher energies), which is advantageous for generating such a latitudinally extended IC signal. If instead $\sim$ 100 GeV electrons scattering on starlight are primarily responsible, the electron CR density must increase markedly at high Galactic latitudes to compensate for the falling of the starlight density to higher latitude. However, generating a very hard CR electron spectrum extending up to $\mathcal{O}$(TeV) energy may be challenging for conventional CR production and acceleration mechanisms. These difficulties may be ameliorated if the hard gamma-ray signal from the *Fermi* bubbles is a transient rather than a steady-state solution.

4.2.1 CRs from the Galactic Center

As discussed in Chapter 4.1, the electron CRs could be produced in the inner Galaxy by mechanisms such as OB associations (Higdon & Lingenfelter 2005), accretion events, and supernova explosions, then entrained in subsequent jets or outflows and rapidly carried up to large scales, avoiding diffusive softening of the spectrum. Breitschwerdt & Schmutzler (1994) suggested that the all-sky soft X-ray emission can be explained by delayed recombination in a large-scale CR and thermal-gas pressure driven wind. Such a wind model has been applied to the Milky Way which could explain the observed Galactic diffuse soft X-ray emission and synchrotron. The model indicates that the Milky Way may possess a kpc-scale wind.

The cooling time (denoted τ) of TeV-scale electron CRs can impose stringent constraints on such models. In the Thomson regime, the cooling time scales as (electron energy)$^{-1}$, leading to estimates of $\tau \sim 10^5$ years for TeV-scale electrons.

However, where scattering on starlight photons is important, electron energies of $100 - 1000$ GeV are no longer in the Thomson regime, so the scattering cross section is suppressed and the cooling time can be longer than naively expected.

Figure 4.2 shows the variation in cooling time (defined as $1/(d \ln E/dt)$) as a function of electron energy and height above (or below) the Galactic plane, for the standard ISRF model, both with and without the inclusion of synchrotron losses (for a simple exponential magnetic field profile)[1]. For example, at $z = 2$ kpc, the cooling time for TeV electrons is $\sim 3 - 4 \times 10^5$ years, rising to $\sim 7 \times 10^5$ years at $z = 5$ kpc. Scatterings purely on the CMB give an upper bound on the lifetime of $\sim 5 \times 10^6 \, (1 \, \mathrm{TeV}/E)$ years, but even several kpc from the GC, scatterings on the infrared photons dominate at TeV-scale energies. The effect of the KN cross-section suppression at higher electron energies can be seen in the small-z limit where synchrotron losses are neglected, so IC scattering of the electrons on starlight is an important contribution to the total energy loss rate.

These relatively short lifetimes, especially close to the Galactic plane, may lead to severe difficulties in propagating CR electrons from the GC out to fill the bubbles. Propagation over such large distances may also lead to significant diffusive softening of the electron spectrum, which must be reconciled with the apparent spatial uniformity of the bubbles' (gamma-ray) hard spectral index. With electron injection primarily at the GC there is also no obvious natural explanation for the flat projected intensity profile, which seems to require sharp increases in the CR density at the bubble walls.

[1]However, note that we have treated the target photon distribution as isotropic.

4.2.2 CRs from the Bubble Edge

If the majority of the electron CRs are produced from shock acceleration within the edge of the *Fermi* bubbles, the electron CRs in the bubble interior might be leftover CRs which undergo cooling after the shock passes through. The CRs continue to diffuse inward from the shock front while also diffusing outward; if the shock is moving faster than the electrons diffuse out, a sharp edge in the resulting *Fermi* bubble gamma-rays is still expected. It is also possible that the CRs may be secondary electrons, produced by enhanced proton-ISM interaction in shocks (within the bubble shell), where protons could be ejected from the GC and entrained in the shocks with high gas density due to shock compression.

We can estimate the diffusion path length of $100 - 1000$ GeV electrons, given the lifetimes calculated in Chapter 4.2.1. We use the estimated diffusion constant from `GALPROP`, $K = 5.3 \times 10^{28}$ cm^2/s at a reference rigidity of 4 GV, and take the diffusion coefficient index to be $\delta = 0.43$ following the results of Ahn et al. (2008). Then the path length is given by,

$$\sqrt{K\tau} \approx 1.4 \left(\frac{E}{1\mathrm{TeV}}\right)^{0.43/2} \left(\frac{\tau}{10^6\mathrm{yr}}\right)^{0.5} \mathrm{kpc}. \tag{4.1}$$

Thus we expect the diffusion scale to be small relative to the bubble size, although not negligible.

Consequently, the electrons in the interior of the *Fermi* bubbles are unlikely to maintain a hard spectrum due to diffusion inward from the bubble walls. In this scenario, one needs to tune the electron CR distribution to get near-flat projected intensity. Although the *Fermi* bubble gamma-rays along any line of sight include contributions from both the bubble interior and bubble shell (due to the integration

along the line of sight), the flat intensity and consistent spectrum of the inner bubble and outer shell templates (Figure 2.16) implies that the CR spectrum in the 3D bubble interior cannot be very different from the spectrum at the 3D bubble shell with electron CRs generated *in situ*.

The edge of the *Fermi* bubbles might contain MHD turbulent fluid with compressed gas and magnetic field. Fast magnetic reconnection rather than shocks might drive the CR acceleration. Significant magnetic reversals within the bubble shell are naturally expected, just like the heliosheath region of the solar system (Drake et al. 2006; Innes et al. 1997): the crossing of the termination shock by Voyager 1 and 2 may indicate the acceleration within regions of fast magnetic reconnection (Lazarian & Opher 2009). It is well known that magnetic field reversal can cause magnetic reconnection. When two magnetic flux tubes of different directions become too close, rearrangement of the magnetic field lines takes place, converting the energy of the magnetic field into energy of plasma motion and heating. Such phenomena have been investigated extensively in e.g. the solar sphere and gamma-ray bursts. In the reconnection region, the energetic particles bounce between two magnetic tubes, undergoing first-order Fermi acceleration as the dominant acceleration process (Beck et al. 1996; Biskamp 1986; Elmegreen & Scalo 2004).

On the other hand, maintaining the shape of the bubble, and preventing it from breaking out, is a non-trivial process. As the bubble rises through the ISM, it tends to fatten simply because the fluid moves faster on its sides than its front. The classical Rayleigh-Taylor instability appears at the leading edge of the bubble, as the inside density is lower than that of the ISM; Kelvin-Helmholtz instability occurs at

the sides of the bubble due to discontinuities in the velocity and density. Although hydrodynamical processes may be capable of stabilizing the bubble structures against these instabilities, it has been suggested that a large-scale coherent magnetic field could help to prevent disruption. We will discuss in Chapter 4.2.3 the possibility that the magnetic field can be coherent on the *Fermi* bubble scale.

4.2.3 CRs from Diffuse Production in the Bubble

The hard, spatially uniform spectrum of the *Fermi* bubbles motivates the possibility of some diffuse injection of hard CR electrons throughout the bubble volume. Such a mechanism, if present, would solve the issues of short electron cooling times, relative to the propagation time from the GC, and the hardness of the required spectrum. A uniform diffuse injection would give rise to a centrally brightened signal, so in models of this type there would most likely need to be some other mechanism increasing the electron intensity at the bubble wall, perhaps associated with a shock there.

This requirement for multiple mechanisms may seem unwieldy, and perhaps also unnecessary, if diffusion or cooling of electrons produced at the shock can explain the flat projected intensity profile and hard spectrum across the entire bubble. Given the large size of the bubble, however, it is unclear whether production or acceleration of electron CRs solely at the bubble walls can give rise to a sufficiently centrally bright and hard signal.

Decay or annihilation of dark matter has previously been proposed as a mechanism for diffuse injection of very hard electrons and positrons; in particular, dark matter annihilation has provided good fits to the data (at least in the inner

$\sim 15 - 20^{\circ}$) in previous studies of the *WMAP* haze (Hooper et al. 2007; Cholis et al. 2009a,b; Harding & Abazajian 2010; McQuinn & Zaldarriaga 2010; Lin et al. 2010; Linden et al. 2010). The IC signal from electrons produced in dark matter annihilation would naively be expected to have approximate radial symmetry about the Galactic center and fall off sharply at increasing r and z, roughly tracing the distribution of dark matter density squared, but smoothed and broadened by diffusion of the electrons. This expectation is in conflict with the bubble morphology, with a gamma-ray distribution elongated *perpendicular* to the Galactic disk, and extending to 10 kpc without much change in intensity. However, this naive picture is based on isotropic diffusion with a spatially uniform diffusion constant, in a tangled magnetic field; including the effects of an ordered magnetic field and anisotropic diffusion can lead to a much more bubble-like morphology (Dobler 2010).

Another way to produce CRs *in situ* inside the bubble is through magnetic reconnection. Electrons could be accelerated directly, or produced as secondaries from accelerated protons. The magnetic fields in the underdense bubbles, which may be inflated by AGN outflow, may relax into an equilibrium filling the entire volume of the bubbles. The timescale depends on the magnetization and helicity of the outflow and also the properties of the ISM. The magnetic field could undergo reconnection on a short timescale, converting magnetic energy into heat. This mechanism can explain how the bubbles could move a large distance through the ISM without breaking up. The reconnection in the bubbles can also accelerate energetic particles, circumventing the problem of synchrotron emitters having a shorter lifetime than the age of the bubble they inhabit (Braithwaite 2010). The *Fermi* bubbles might be initially highly turbulent, with a disordered magnetic field far from equilibrium

(gas pressure and Lorentz force are not balanced); the kinetic energy would then be dissipated by viscosity, especially in the low density bubble.

The time scale of the relaxation to equilibrium can be estimated (Braithwaite 2010) by,

$$\tau_{\rm relax} \approx \frac{r}{\alpha v_{\rm A}} = \frac{r\sqrt{4\pi\rho}}{\alpha B} = \frac{r}{\alpha}\left(\frac{4\pi r^3\rho}{6E}\right)^{\frac{1}{2}} \tag{4.2}$$

$$\approx 4.4\times10^{6}\left(\frac{\alpha}{0.1}\right)^{-1}\left(\frac{r}{4{\rm kpc}}\right)\left(\frac{\rho}{10^{-5}m_{\rm p}{\rm cm}^{-3}}\right)^{\frac{1}{2}} \left(\frac{B}{5\mu{\rm G}}\right)^{-1}{\rm yr}, \tag{4.3}$$

where $v_{\rm A}$, B and E are the Alfvén speed, magnetic field and energy *at equilibrium*. We use the estimated characteristic values for the *Fermi* bubbles. The resulting time scale is on the order of $10^{6-7}yr$. Furthermore, the reconnection time scale is orders of magnitude shorter than the relaxation time scale: we expect to see ongoing reconnection if equilibrium has not already been reached.

4.3 Potential connections to other open questions

4.3.1 The Cosmic Gamma-ray Background

Measurement of the intensity and spectrum of cosmic gamma-ray background (Abdo et al. 2010c; Fields et al. 2010) has suggested that instead of rare but intrinsically bright active galaxies, it is numerous but individually faint normal galaxies that comprise the bulk of the *Fermi* gamma-ray background. This result infers a tighter correlation between cosmic star formation history and the cosmic gamma-ray background (Thompson et al. 2007; Lacki et al. 2010). Galactic outflows have

been identified from near infrared observations at redshift $z \sim 2$ (Alexander et al. 2010) indicating that such outflows are common features of ultraluminous infrared galaxies. Such outflows can entrain energetic cosmic rays to escape the galaxies, thus providing a way to contribute to the cosmic gamma-ray background at energies in the *Fermi* range. The *Fermi* bubbles may provide local evidence for such a scenario.

4.3.2 The Origin of Hypervelocity Stars

Recent surveys of hypervelocity stars (HVSs) have found 16 HVSs which are mostly B-type stars with ages $\gtrsim (1-2) \times 10^8$ yr (see e.g. Brown et al. 2009). These HVSs distributed in the Galactic halo are believed to originate from the GC involving interactions of stars with the MBH (Hills 1988; Yu & Tremaine 2003). Thus energetic energy release from the GC which generate the *Fermi* bubbles could be dynamically related to the ejection of HVSs. Recently Lu et al. (2010) have shown that the spatial distribution of the discovered HVSs is consistent with being located on two thin disk planes. The orientation of the planes are consistent with the inner/outer clockwise-rotating young stellar disk. One possibility could be that the HVSs originate from some unknown and previously existing disk-like stellar structures. HVSs might have been ejected periodically, and related accretion events produce jets which generate the *Fermi* bubbles.

4.3.3 The Future of the *Fermi* Bubbles

What is the future of the *Fermi* bubbles, are they in a "breakout" stage? An interesting possibility is that the *northern arc* and even part of the *Loop I* feature are

parts of the relics of previous bubbles, and the bubble production is a quasi-periodic process. The bubbles might be fast expanding shocks which might finally expand freely into the galactic halo, thus contaminating the ISM with entrained hot gas and CRs. An intriguing possibility is that CRs and gas released from previous such bubbles to the Galactic halo may contribute to the observed diffuse X-ray and gamma-ray background. In any case, the study of *Fermi* bubbles would have potential implications for the understanding of the *feedback* mechanism from the Galaxy.

4.3.4 Missing Baryons and High-Velocity Clouds

N-body/gas dynamical galaxy formation simulations have shown that for Milky Way like galaxies, about 70% extra baryonic mass should reside around the galaxy in form of hot gas (Sommer-Larsen 2006). Warm clouds are confined by the pressure of the ambient hot halo gas, which contains mass at least two orders of magnitude more than these warm clouds. The study of the *Fermi* bubbles may provide hints of hot gas feedback from the Galaxy, the search for the missing baryons (Bregman 2007) and the puzzle of high-velocity clouds.

4.3.5 Metallicity

Although the Galactic outflow can not inject a large fraction of the ISM, a significant amount of the freshly produced metals could be channeled along the galactic wind. In ordinary photo-ionization it is difficult to make the [N II]/Hα ratio exceed about 1.0; shock ionization/excitation is plausible once [N II]/Hα is detected. [N II]/Hα

has been estimated ∼1.5 in NGC 253, less than 1.0 in M82 where the ratio trends to increase far from the disk.

The presence of metals in the IGM has been interpreted as the consequence of energetic metal-rich outflows from galaxies. Active star formation in the inner Galaxy may contaminate the surrounding ISM, with (periodic) Galactic winds entraining the metal-rich gas to tens of kpc. The *Fermi* bubbles may give some hints to understanding the feedback and metallicity of the IGM. Jets from GC in general do not imply a high metallicity, and detections of metal rich outflows may essentially constrain the energetic injection from jets or Galactic outflows from previous starburst towards the GC.

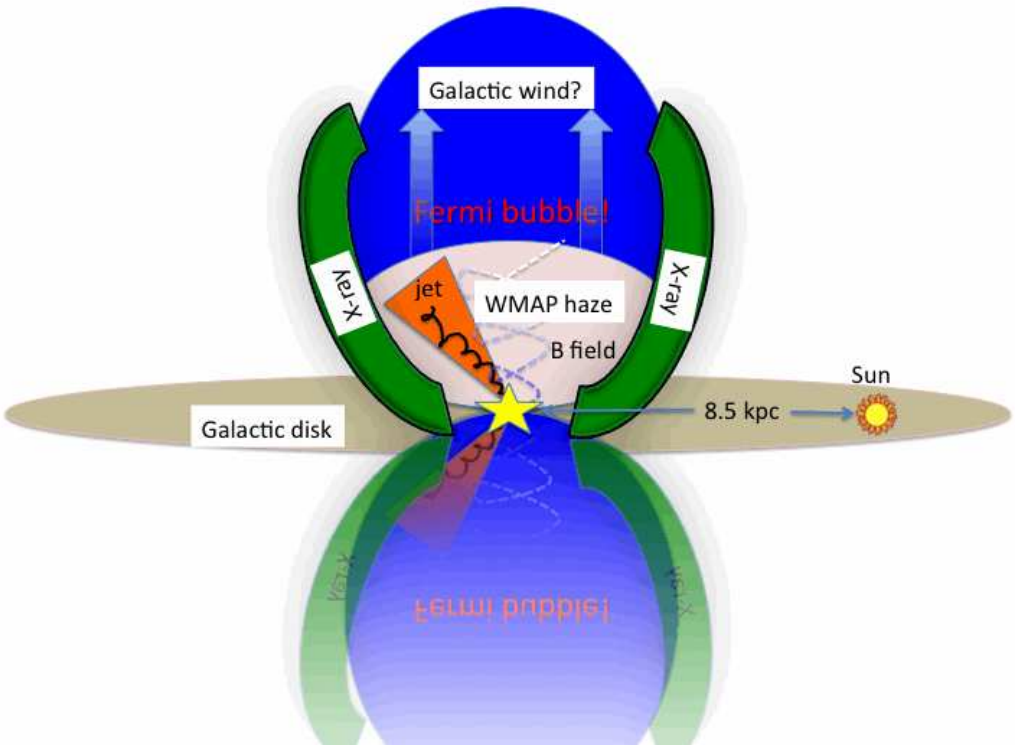

Figure 4.1.— A cartoon picture to summarize the observations of the *Fermi* bubble structures. Two blue bubbles symmetric to the Galactic disk indicate the geometry of the gamma-ray bubbles observed by the *Fermi*-LAT. Morphologically, we see corresponding features in *ROSAT* soft X-ray maps, shown as green arcs embracing the bubbles. The *WMAP* haze shares the same edges as the *Fermi* bubbles (the pink egg inside the blue bubbles) with smaller extension in latitude. These related structures may have the same physical origin: past AGN activities or a nuclear starburst in the GC (the yellow star).

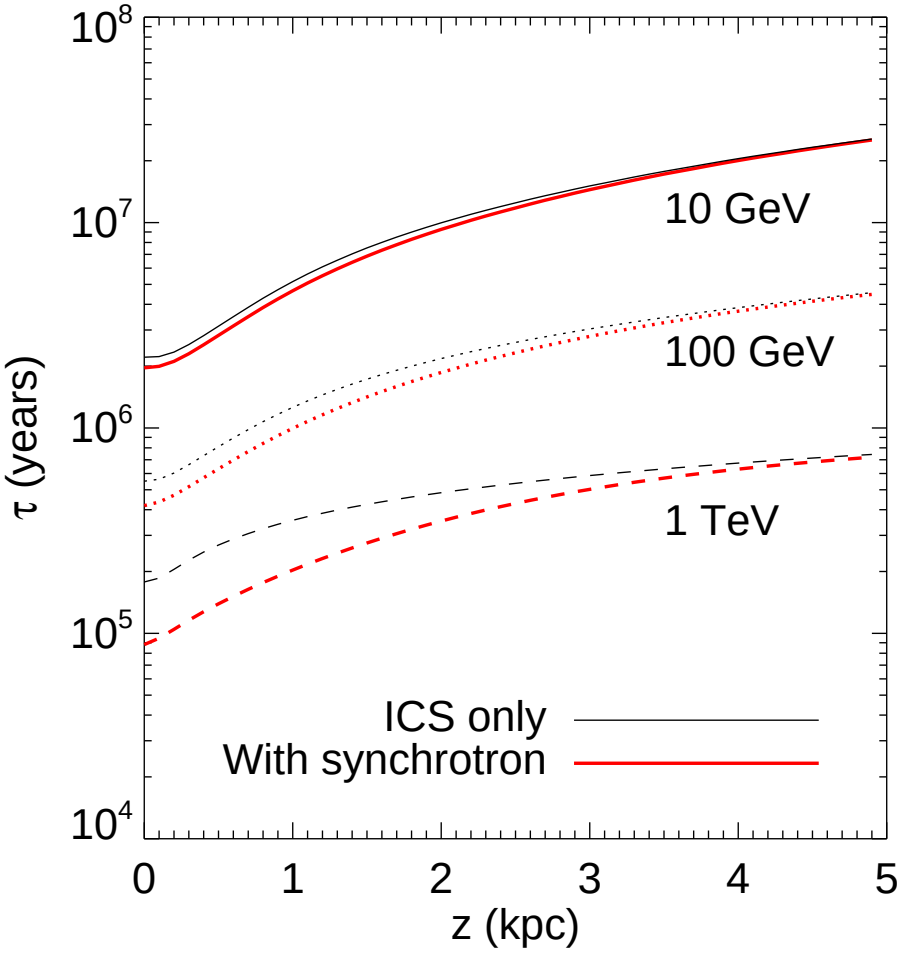

Figure 4.2.— The cooling time for electron CRs as a function of energy and height above the Galactic plane, for $r = 0$. *Thin black lines:* Synchrotron losses are neglected; equivalently, the B-field is assumed to be negligible everywhere. *Thick red lines:* The cooling time calculation includes synchrotron losses in a magnetic field given by $|B| = 30e^{-z/2\mathrm{kpc}}\mu\mathrm{G}$. We use the standard radiation field model from `GALPROP` version 50p, and define the cooling time $\tau = 1/(d \ln E/dt)$.

Chapter 5

Evidence of Large Scale Galactic Jets

Although accretion onto supermassive black holes in other galaxies is seen to produce powerful jets in x-ray and radio, no convincing detection has ever been made of a kpc-scale jet in the Milky Way. As we have shown in previous chapters, the recently discovered *Fermi* bubbles structure, the pair of ∼10 kpc tall gamma-ray bubbles in our Galaxy may be signs of earlier jet activity from the central black hole. In this chapter, we identify a gamma-ray cocoon feature in the southern bubble, a jet-like feature along the cocoon's axis of symmetry, and another directly opposite the Galactic center in the north. The cocoon and jets have a hard spectrum from $1-100$ GeV, with a cocoon luminosity of $5.5 \pm 0.45 \times 10^{35}$ erg/s and total jet luminosity of $1.8 \pm 0.35 \times 10^{35}$ erg/s at $1-100$ GeV. If confirmed, these jets are the first resolved gamma-ray jets ever seen.

5.1 Introduction

Supermassive black holes (SMBHs) of 10^6 to 10^{10} solar masses are believed to lie at the center of most galaxies and are fed by accretion of ambient gas and stars. Accretion-powered jets have been observed at various astronomical scales ranging from active galactic nuclei (AGN) (Bridle & Perley 1984), especially blazars (BL Lac objects and flat spectrum radio quasars) and gamma-ray bursts at the bright to Galactic binaries (stellar mass black holes, neutron stars and cataclysmic variables). Some of these objects appear to have produced jets nearly continuously for at least tens of millions years. The mechanism by which jets turn on and off is one of the major puzzles in high energy astrophysics, and may be connected to star formation (Antonuccio-Delogu & Silk 2008). The relativistic jets inject significant amounts of energy into the medium within which they propagate, creating an extended, under-dense and hot cocoon. After decades of study, we still lack a complete understanding of the main mechanism launching, accelerating and collimating jets, with limited knowledge of the energy content, the composition, and the particle acceleration mechanisms of the jets (Blandford & Znajek 1977; Blandford & Payne 1982).

The SMBH at the center of the Milky Way (MW) is surrounded by clusters of young stars and giant molecular clouds (Morris & Serabyn 1996). Although there are indications of past activity (Sunyaev et al. 1993), the SMBH is currently in a quiescent state. Despite the abundant observational evidence of large-scale jets in other galaxies, it was not expected that the Milky Way's SMBH would produce such a relativistic collimated structure, given its current quiescence. However, the

Milky Way must have undergone phases of nuclear activity in the past in order for the SMBH to grow, and it is plausible that signs of past activity are still visible. One might expect relics of past activity in high energy cosmic rays (CRs) and hot gas, perhaps far off the disk. The sensitivity and angular resolution of the Large Area Telescope (LAT) on board the *Fermi Gamma-ray Space Telescope* (Atwood et al. 2009) make possible the search for inverse Compton (IC) gamma-rays from a Galactic jet.

In this work, we use LAT data at $0.3 < E_\gamma < 100$ GeV to look for unexpected diffuse Galactic gamma-ray structure. We will show evidence for a large scale collimated double-jet structure, which appears symmetric with respect to the Galactic center (GC). For the remainder of this paper, we refer to these collimated jet-like structures as the "gamma-ray jets" or simply the "jets". We also argue that the southern jet has produced a large cocoon feature, visible over a wide range of gamma-ray energies. These jets and cocoon features might be associated with the previously discovered *Fermi* bubble structures (Su et al. 2010), and may hold the key to understanding their origin.

In Section 5.2 we describe the *Fermi*-LAT data selection and our data analysis procedure including map making. In Section 5.3 we describe our model of the Galactic diffuse gamma-ray emission. In Section 5.4, we show that the gamma-ray maps constructed from three-year *Fermi*-LAT observations reveal evidence of large-scale Galactic jet features along with a south cocoon structure. We characterize the morphology of the jet/cocoon system in some detail and employ regression template fitting to determine the jet and cocoon spectra in Section 5.5. We calculate and discuss the radio luminosity of the jet in Section 5.6 and carefully discuss the

statistical significance of the jet structure in Section 5.7. Finally, we discuss the implications of the presence of the Galactic jet and future observations in Section 5.8.

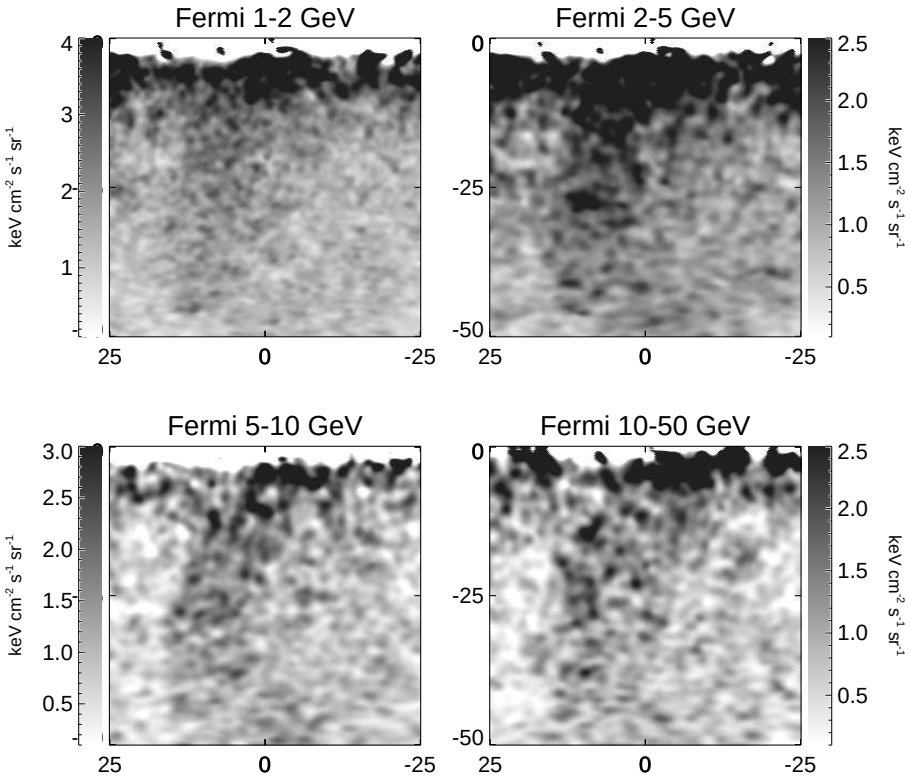

Figure 5.1.— A large scale gamma-ray cocoon feature is revealed by template decomposition of the gamma-ray maps in energy range of $1-2$ GeV (*upper-left*), $2-5$ GeV (*upper-right*), $5-10$ GeV (*lower-left*), and $10-50$ GeV (*lower-right*) maps constructed from *Fermi*-LAT three year observations. Bright point sources have been masked and fainter ones subtracted. The maps are smoothed by a Gaussian kernel with FWHM of 90 arcmins.

5.2 Map Construction from Fermi-LAT Data

5.2.1 *Fermi* Data Selection

We make use of the *Fermi* Pass 7 (P7) data products, using the latest publicly available event reconstruction algorithms[1].For the purpose of studying Galactic diffuse gamma-ray emission with minimal non-photon contamination (low background), we select events designated ULTRACLEAN[2] class that have the most stringent data selection criteria, so that any diffuse features appearing on the gamma-ray maps at not due to CR contamination. Photons coming from the bright limb at Earth's horizon, dominantly produced by grazing-incidence CR showers coming directly towards the LAT are a strong source of contamination. We minimize this background by restricting to events with zenith angle less than 100° as suggested in the *Fermi* Cicerone[3].

5.2.2 Map Making

Our current gamma-ray maps (v3_3) constructed from the three year *Fermi* data have greater signal/noise and significantly lower background compared to the previously released v2_3 maps in Su et al. (2010). The "three year maps" exclude some short

[1]Details at http://fermi.gsfc.nasa.gov/ssc/

[2]Maps produced with CLEAN have about 20% more events. Repeating our analysis on these maps yields similar results, with similar error bars at $E \lesssim 10$ GeV, and slightly larger error bars at $E \gtrsim 10$ GeV, where background is relatively more important.

[3]http://fermi.gsfc.nasa.gov/ssc/data/analysis/documentation/.

time periods, primarily while *Fermi* passes through the South Atlantic Anomaly. We construct maps using the newly released photon event list corresponding to the P7_V6 Instrument Response Functions (IRFs).

As in Su et al. (2010), we construct maps of front-converting and back-converting events separately, smooth to a common PSF, and then combine them. To reveal the diffuse emission, we subtract point sources using the Second *Fermi*-LAT catalog (2FGL), which is based on 24 months of LAT observations[4] and the P7_V6 event selections and IRFs. The point-spread function (PSF) and effective area of the *Fermi*-LAT varies with energy, and we subtract each point source from the maps in each energy bin, using the in-flight version of the PSF contained in the P7_V6 IRFs. We produce the exposure maps using the `gtexpcube` task in the Fermi Science Tools. Further details of the map processing may be found in Chapter 2.1. The v3_3 maps used in this work are available for download[5] in both FITS and jpeg formats.

5.3 Diffuse Galactic Gamma-ray Emission Models

At low ($\sim$1 GeV) energies, and near the Galactic plane ($|b| < 20°$), the gamma rays observed by *Fermi*-LAT are dominated by photons from the decay of π^0 particles, produced by the collisions of CR protons with ambient gas and dust in the ISM. Collisions of CR *electrons* with the ISM (primarily protons, but also heavier nuclei)

[4] `http://fermi.gsfc.nasa.gov/ssc/data/access/lat/2yr_catalog`, the file we used is `gll_psc_v05.fit`

[5] Available at `http://fermi.skymaps.info`

produce bremsstrahlung radiation. The CR electrons also inverse-Compton scatter the interstellar radiation field up to gamma-ray energies. In order to reveal the gamma-ray jet features, significant π^0 emission, bremsstrahlung, and IC emission from the Galactic disk must be removed. We take two approaches to this foreground removal: one is to use the *Fermi* Diffuse Galactic Model[6] provided by the *Fermi* team; the second is to employ a linear combination of templates of known emission mechanisms, using existing maps from multi-wavelength observations and/or constructed geometric templates.

5.3.1 *Fermi* Diffuse Galactic Model

The LAT Diffuse Galactic Model is a comprehensive model of Galactic gamma-ray emission from the ISM[7]. The *Fermi* diffuse model is primarily designed as a background template for point source analysis or investigation of small-scale diffuse structures, and comes with a number of caveats. However these caveats apply mainly near the Galactic plane, and at $E > 50\,\mathrm{GeV}$. It is nevertheless useful for qualitatively revealing features in the diffuse emission at high latitude. In this work, we use the version of *Fermi* diffuse Galactic model `gal_2yearp7v6_v0.fits`.

[6] `http://fermi.gsfc.nasa.gov/ssc/data/`

[7] available from `fermi.gsfc.nasa.gov/ssc/data/`

5.3.2 Simple Template-Based Diffuse Galactic Model

As we did in Chapter 2.1, we use the SFD dust map as a template of the π^0 gamma foreground. The correlation between *Fermi* gamma-ray maps and the SFD dust map is striking, and most of the ISM emission is removed by this subtraction. To reveal the structure deeper into the plane, a simple disk model is subtracted (Su et al. 2010)[8]. The disk model mostly removes the IC gamma-rays produced by cosmic ray electrons interacting with the interstellar radiation field (ISRF) including CMB, infrared, and optical photons; such electrons are believed to be mostly injected in the Galactic disk by supernova shock acceleration before diffusing outward. The two jets are symmetric with respect to the Galactic plane and well centered on the GC, thus they are unlikely to be local structures.

5.4 Gamma-ray Cocoon and Evidence of Galactic Jet

The gamma-ray cocoon in the south is visible in the 3-year LAT maps at energies from $1 - 50$ GeV (Figure 5.1). We remove the dominant diffuse Galactic signal from π^0 (and bremsstrahlung) gamma-rays produced by CR protons (electrons) interacting with the ISM using a dust map template constructed based on far IR data (Schlegel et al. 1998). A smooth disk model is also subtracted to reveal the structure deeper into the plane. This model mostly removes the IC gamma-rays produced by

[8]The functional form of this disk template is $(\csc|b|) - 1$ in latitude and a Gaussian ($\sigma_\ell = 30^\circ$) in longitude

CR electrons interacting with the interstellar radiation field including CMB, infrared and optical photons. We also subtract a uniform template of the *Fermi* bubbles to remove the corresponding gamma-ray emission. The cocoon feature is revealed on the East (left) side of the previously discovered southern *Fermi* bubble structure (Su et al. 2010), with relatively sharp edges. By inspection, the major symmetric axis of the cocoon lines up with the Galactic center to within $\sim 5^\circ$, and the major to minor axis ratio is about a factor of three. The gamma-ray luminosity of the south cocoon with Galactic latitude $|b| > 20^\circ$ and in the energy range $1 - 100$ GeV is $5.5 \pm 0.45 \times 10^{35}$ erg/s. The morphology of the gamma-ray cocoon resembles the observed radio cocoon structures of Fanaroff-Riley (FR) type II (Fanaroff & Riley 1974) active radio galaxies (e.g. Cygnus A), which have been found surrounding collimated large-scale jets and may be formed by backflow of magnetized jet plasma. How the gamma-ray cocoon system formed and retains its tight columnar shape despite traveling from the GC for $\sim$10 kpc is intriguing. The presence of this large scale cocoon suggests collimated injection of high energy particles from the inner Galaxy.

In Figure 5.2, we show the $0.8 - 3.2$ GeV gamma-ray map of the inner Galaxy. A pair of collimated linear features are revealedFigure 5.2, with similar morphology in each energy bin. There are no other apparent large scale features in the residual maps. The gamma-ray jets do not appear to be associated with the well-known *Loop I* structure (Berkhuijsen 1973). The north jet extends from the GC to Galactic coordinates $(\ell, b) = (-11, 40)$, and the south jet extends from the GC down to $(\ell, b) = (11, -44)$. Although the jets are faint, 3 lines of evidence suggest they are real: (1) the jets both emanate from the GC, in nearly opposite directions; (2) the

jets extend away from the GC to about the edge of the previously discovered *Fermi* bubble structure (Su et al. 2010); and (3) the south jet aligns with the symmetry axis of the cocoon structure. The morphology of the jet and cocoon gamma-ray feature and the possible association with the *Fermi* bubbles strongly suggests the Galactic center origin of these structures and implies recent activity towards the inner Galaxy.

On a much smaller scale, *Chandra* X-ray observations have revealed a faint jet-like feature at sub-pc scale, pointing toward Sgr A*(Muno et al. 2008). It is tempting to interpret this feature as a jet of synchrotron-emitting particles ejected from the SMBH. However, due to its much smaller size and $\sim$15° misalignment with the gamma-ray jet, there is no clear association. Limits on the gamma-ray jet from other wavelengths do not strongly constrain its nature, underscoring the need for further multi-wavelength studies.

The projected direction of the gamma-ray jets is about 15° from the north-south axis of the Galaxy. If the gamma-ray jets constitute the projection of double large-scale jets symmetric to the Galactic plane and the GC, taking the distance from the solar system to the GC $R_\odot = 8.5$ kpc, each projected jet is $\sim$10 kpc. The small angle of the projected jet relative to the north-south Galactic axis suggests that the apparent length of $\sim$10 kpc is a good approximation of the spatial scale of the Galactic jet. The width of the jets appears to be $\lesssim 5°$. The total luminosity of the north and south jet-like features is $1.8 \pm 0.35 \times 10^{35}$ erg/s at $1 - 100$ GeV (see Table 5.2). The jets do not align with any plausible artifacts relating to the Fermi orbit or scan direction, or any other known systematics. The north and south jet have similar integrated gamma-ray flux, so there is no evidence the jets are close to

the line of sight; otherwise, the approaching jet would appear substantially Doppler brightened relative to the receding one.

We now turn to the relation between the jet/cocoon and the *Fermi* bubbles. We recently discovered two giant gamma-ray bubbles with a total luminosity from $1-100$ GeV of 2.0×10^{37} erg/s[9], extending $\sim 50^\circ$ above and below the GC, with a width of $\sim 40^\circ$ in longitude, and found them to be spatially correlated with a hard-spectrum microwave excess (known as the *WMAP* haze) (Finkbeiner 2004a) and large-scale X-ray features (Su et al. 2010). Galactic shock waves produced by energetic explosions at the Galactic nucleus or by a high rate of supernova explosions in the nuclear disk will be channeled by the decreasing ambient gas density in directions perpendicular to the Galactic plane.

The gamma-ray emission associated with these bubbles has a significantly harder spectrum ($dN/dE\sim E^{-2}$) than the IC emission from electrons in the Galactic disk, or the gamma-rays produced by decay of π^0 from proton-ISM collisions. The *Fermi* bubbles are likely formed during an active phase in the Galactic center $\sim 10^{6-7}$ years ago from the central supermassive black hole. The bubble region might consist of decelerated jet material, radiating isotropically. Observational data and numerical simulations indicate that the energy required to form the bubbles is on the order of 10^{55-58} ergs (Su et al. 2010; Guo & Mathews 2011a). Even though the current jet luminosity is relatively faint, the discovery of the jet/cocoon system generally supports the AGN hypothesis for the origin of the bubbles.

[9]We note that in Su et al. (2010), the total gamma-ray luminosity of the *Fermi* bubbles was mis-quoted as 4.0×10^{37} erg/s.

5.5 Energy Spectrum of the Gamma-ray Cocoon and Jets

We have shown in Figure 5.1 that the gamma-ray jets, the cocoon, and the *Fermi* bubbles all have a harder spectrum than other large-scale diffuse ISM emission. In order to measure the hardness of the spectrum and to explore possible mechanisms responsible for the observed gamma-ray emission, we maximize the likelihood that the maps are described by a linear combination of spatial templates, one for each gamma-ray emission mechanism. We fit a coefficient to each emission component using a multi-linear regression of simple templates, one energy bin at a time. By combining results from 12 logarithmically-spaced energy bands from 300 MeV to 300 GeV, we determine an SED for each component. In each fit, we maximize the Poisson likelihood of a simple diffuse emission model involving the 7 following templates: the SFD map of Galactic dust (Schlegel et al. 1998), the simple disk model, the *Fermi* bubbles, a template of the *Loop I* structure (Su et al. 2010), the gamma-ray cocoon, the gamma-ray south jet, and a uniform background as template to account for background gamma-ray emission and cosmic ray contamination (Su et al. 2010). All maps and templates have been smoothed by a Gaussian kernel with FWHM of 2° for the regression analysis. Systematic uncertainties are dominated by the imperfect representation of the diffuse emission by these simple templates. We feel that this analysis is sufficient for a rough characterization of the cocoon and jet spectra, and provides motivation for more thorough analysis using a more physical model in the future.

For each set of model parameters, we compute the Poisson log likelihood,

$$\ln \mathcal{L} = \sum_i k_i \ln \mu_i - \mu_i - \ln(k_i!), \tag{5.1}$$

where μ_i is the synthetic counts map (i.e., linear combination of templates times exposure map) at pixel i, and k is the map of observed counts. The last term is a function only of the observed maps. We compute errors in the Gaussian approximation by inverting the matrix of second partial derivatives of $-\ln \mathcal{L}$ to obtain the covariance matrix, and taking the square root of the diagonals. So far we have described the procedure for obtaining the correlation coefficient for each template at each energy. However, some templates have units (e.g., the SFD dust map is in magnitudes of E_{B-V} reddening) so the correlation coefficient has unusual units (e.g. gamma-ray emission per magnitude). In such a case we multiply the correlation spectrum by the average SFD value in the ($|b| > 20^\circ$) bubble region, to yield the average spectrum of dust-correlated gamma-ray emission in this region. For the uniform, *Loop I*, cocoon, jet, and bubble templates, no renormalization is done. These templates are simply ones and zeros (smoothed to the appropriate PSF), so the south jet spectrum is simply the spectrum of the south jet template shown in e.g. left panels of Figure 5.4, *not* the mean of this template over the whole bubble region.

The spectrum for emission correlated with the gamma-ray jet and cocoon is clearly significantly harder than either of these components, consistent with a *flat* spectrum in $E^2 dN/dE$. This fact coupled with the distinct spatial morphology of the jet/cocoon system indicates that if these gamma-ray features are generated by IC scattering of interstellar radiation fields, then a *separate* electron population must

exist in the jet/cocoon. We also note that the spectrum of the jet/cocoon template does not fall off significantly at energy $\lesssim$1 GeV as the bubble spectrum does. The fitting coefficients and corresponding errors of each template are listed in Table 5.1 and 5.2.

The hardness of this spectrum may be the key to deciphering the origin of the gamma-ray jet/cocoon. In (Su et al. 2010), we show that at lower energy ($E \lesssim 1\,\mathrm{GeV}$) the bubble spectrum falls sharply with decreasing energy (becomes dramatically harder than -2). With reduced statistical error from three year LAT data and the new Pass 7 `ULTRACLEAN` event selection, we confirm significant falling of the bubble spectrum at lower energy but not the jet and cocoon component. This is true whether we perform the entire analysis with front-converting events only, or use front-converting at $E < 1$ GeV and both front- and back-converting at $E > 1$ GeV as usual.

The null hypothesis of zero intensity of the north (south) jet is ruled out by 3.1σ (4.1σ), respectively, and 5.2σ jointly for the whole jet structure. The same fit simultaneously finds the cocoon with 12σ significance. Since the region south of the Galactic center has less foreground emission than the north (where ρ Oph is), we focus on the south jet/cocoon for our analysis. Figure 5.3 (right panel) shows the resulting energy spectrum of the gamma-rays associated with the cocoon and the south jet. Like the *Fermi* bubbles, the energy spectrum of the jet/cocoon is harder than other diffuse gamma-ray components, although the cocoon has a spectrum at < 1 GeV different from the *Fermi* bubbles, which suggests its origin from a distinct population of electron CRs. The cocoon spectrum is consistent with $E^2dN/dE \sim$ constant, and the north and south jet structures have an energy spectrum of

$E^2dN/dE \sim E^{0.2\pm0.2}$ at latitudes $|b| > 20^\circ$. The correlation coefficients for the SFD map and simple disk model are multiplied by the average value of these maps in the bubble region with a $|b| > 20^\circ$ cut to obtain the associated gamma-ray emission. Given how hard the cocoon/jet spectra are up to ~ 100 GeV, bremsstrahlung can be ruled out as the emission mechanism based on the arguments in (Kino et al. 2009). Maps of the models constructed from linear combinations of these templates, and the residual maps between the *Fermi* data and the combined templates at different energy bins in Figure 5.4. To increase signal/noise, larger energy bins are used. The *left* column of this figure shows the linear combination of the disk, *Loop I*, uniform, bubble template, the south cocoon, and the south jet template, that provide the best fit to the *Fermi* maps (*middle column*) after subtracting the best fit SFD dust template. Because the π^0 emission traced by SFD is so bright, it is subtracted from both the models and data shown in this figure. The difference maps (data minus template model) are in the *right* column. The template fitting is done for the region with $|b| > 20^\circ$ to avoid contamination from the Galactic disk. The subtraction of the model largely removes the features seen in the *Fermi* maps with $|b| > 20^\circ$. We have also masked the inner Galactic plane region ($|b| > 4^\circ$ and $|l| > 60^\circ$), which is significantly contaminated by point sources. We use the same gray scale for all panels. We find that both the disk IC template and *Loop I* features fade away with increasing energy, but the jet template does not. The oversubtraction in the residual maps, especially in the lower energy bins, is due to the simple disk IC model, which is not a good template across the entire disk. However, in the fit region ($|b| > 20^\circ$), the residual maps are consistent with Poisson noise without obvious large scale features.

The gamma-ray jets appear to possess north-south symmetry in morphology without noticeable difference in intensity. To investigate whether there is any spectral difference between the north and south jets, we augment the 7-template fit (dust, simple disk, *Fermi* bubble, cocoon, south jet, uniform, *Loop I*), with a *north jet* template. We show the resulting spectrum in Figure 5.5 and the maps in Figure 5.6. We then repeat the previous fitting procedure involving the simple disk IC template, but splitting the bubble template into *north and south bubble* templates, and allow an independent fit of the two jet templates along with the two bubbles. The goal is to identify variations in the intensity and spectral index between the northern and southern jet and the dependence of the jet spectrum on the combination of different emission templates. Even given this freedom, no significant spectral differences are found between the north and south jet or the north and south bubbles. There was no significant improvement of the likelihood for such splitting. The spectrum and the maps are shown in Figure 5.7 and Figure 5.8, respectively. Our conclusion is that the gamma-ray jets appear to be north-south symmetric, both with a hard spectrum. This statement is largely independent of our choice of template for the disk IC emission. In summary, we found no apparent difference between the north and the south jet both in morphology and in energy spectrum, which indicates they might share the same origin.

5.6 Expected Radio Luminosity of the Jet

The gamma-ray jet/cocoon structure is not visible in the *ROSAT* All-Sky Survey of soft X-ray (Snowden et al. 1997), *WMAP* microwave maps, radio maps at 408 MHz

(Haslam et al. 1982a), or any other available radio maps. We estimate expected radio spectra in Figure 5.9 corresponding to electron spectral indices $1.5 < \gamma < 2.5$, and find that over this range, current full-sky radio surveys are not sensitive enough to detect the jet. However, combining the gamma-ray energy spectrum along with the radio limits, we find that the cosmic ray electrons producing the jet has a hard spectrum with spectral index $\lesssim -2$. The interstellar radiation field model is taken from `GALPROP` version 50p, and the magnetic field is assumed to be 5 μG for synchrotron calculation. The data points in the upper panels show the south cocoon emission the same as in Figure 5.3. The arrows shows 3σ upper limits rather than data points with 1σ error bars, due to the large uncertainties in those energies. The data point in the lower panel shows the magnitude of the *WMAP* haze averaged over $b = -20^\circ$ to -30° in the 23 GHz K-band, and the gray area indicates the range of synchrotron spectral indices allowed for the *WMAP* haze (Dobler & Finkbeiner 2008). Two arrows at lower frequency shows the 3σ upper limits for the cocoon radio emission from Rhodes/HartRAO 2.326 GHz radio continuum survey (Jonas et al. 1998) and Haslam 0.408 GHz map (Haslam et al. 1982b). The same population of cosmic ray electrons can consistently produce both the radio/microwave observations and the gamma-ray observations.

In order to estimate the expected radio luminosity of the jet, we must either have a physical model of the radio and gamma-ray emission mechanisms, or a prototype object for comparison. VLBA 5 GHz observations of blazars detected by LAT provide one benchmark (Linford et al. 2011). This sample of blazars shows a median 5 GHz flux of ~ 300 mJy and a median gamma-ray flux ($0.1 - 100$ GeV) of 3×10^{-8} photons cm^{-2}s^{-1}, although individual objects can deviate from this ratio by

an order of magnitude or more. BL Lac objects have a spectrum of $dN/dE \sim E^{-1.8}$ is this energy range, and therefore have 1/15 of their $0.1 < E < 100$ GeV photons in the range $1 - 2$ GeV. Assuming such a spectrum, a 5 GHz flux of 300 mJy corresponds to 4×10^{-9} GeV cm^{-2}s^{-1} $(1 - 2$ GeV). Therefore, the 5 GHz radio signal corresponding to our observed 4×10^{-7} GeV cm^{-2}s^{-1}sr^{-1} would be 30 Jy/sr, much smaller than our radio limits in Figure 5.9. However, because BL Lac objects are thought to contain a relativistic jet pointed along the line of sight, they may be a poor analog for the Galactic jet.

An alternative is to take a magnetic field constrained by radio and Faraday rotation measure observations (Sun et al. 2008) and an interstellar radiation field (taken from `GALPROP`, 4 kpc below the Galactic center) to compute the IC gammas and synchrotron given a power-law CR electron spectrum. The high-energy cutoff of the electron spectrum is important for the IC gammas, especially for spectra harder than $dN/dE \sim E^{-2}$. As an example, we have computed the IC gamma-ray and synchrotron emission for 4 power laws, with spectral index in the range $\gamma = 1.5 - 2.5$ with a cutoff at $E_{electron} = 1$ TeV (Figure 5.9). The electron spectra are normalized such that the IC gammas go through the data points. The synchrotron is then computed assuming a 5 μG magnetic field and the `GALPROP` ISRF (Porter et al. 2008) at 4 kpc below the Galactic plane. Upper limits from maps at 408 MHz (Haslam et al. 1982b) and 2.3 GHz (Jonas et al. 1998), and a data point from WMAP 23 GHz 4 kpc off the disk (which together serve as an upper limit for the jet brightness (Dobler & Finkbeiner 2008)) are included. Most of the lines pass below the limits, making it plausible that the radio signal corresponding to a gamma-ray jet would not yet have been observed. Additional uncertainty arises from the fact that the

1 GHz radio signal is produced by order 1 GeV electrons, whereas the gamma-ray signal arises from order $100 - 1000$ GeV electrons. If the electron spectrum has any downward curvature over this range in energy, the radio/microwave limits become even less constraining. Another uncertainty comes from the choice of energy cutoff for the power law. We considered spectra with cutoffs at 3 and 5 TeV with index $\gamma \sim 3$ to fit the gamma-ray data. Such spectra predict a synchrotron signal bright enough to be ruled out by the radio data. This implies that the required CRe spectrum is much harder than the locally measured index of $\gamma \sim 3 - 3.25$.

5.7 Statistical Significance of the Jet

In Figure 5.10, we show the full sky residual maps at $0.8 - 3.2$ GeV after subtracting the *Fermi* diffuse emission model. This figure is the full sky version of Figure 5.1. We identify a pair of Galactic jet features towards the inner Galaxy, present both above and below the Galactic plane and aligned with the Galactic center. There are no other significant large-scale jet structures appearing in the full sky gamma-ray map. The *Fermi* bubble structure has been included in the diffuse emission model. We find no large-scale jet features other than the central Galactic jet towards the inner Galaxy. The Galactic jet feature is crossing the Galactic center, and aligns with the long axis of the cocoon structure. *Lower panel:* The *Fermi* bubble edge has been marked in green dashed circles above and below the Galactic center, overplotted on the gamma-ray map the same as the *upper panel*. Both the north and the south jet approximately ends on the edge of the Fermi bubble structure.

Our best-fit values are derived from a maximum likelihood analysis, in which

we maximize the Poisson probability of observing the observed counts, given a set of model parameters. The error bars are derived from the parameter covariance matrix. In our previous work (Su et al. 2010), we analyzed numerous mock maps to verify that our code gives unbiased results with the correct uncertainties, at least in the case where the model (plus Poisson noise) is a good description of the data. However, our fits contain systematic residuals, and it is necessary to investigate to what extent these might be able to mimic a signal. To this end, we have repeated the 7-component fit with the cocoon and jet structures shifted around the sky at 5 degree intervals in longitude ℓ, and determined the best fit coefficient for each case by fitting the same templates as in Figure 5.3. By placing the templates at different position along the longitudes where we expect no significant large scale diffuse structures, we can measure the RMS of the jet and cocoon coefficients, and this RMS may exceed that due to the Poisson noise. In some parts of the sky, (e.g. $\ell \sim 290 - 320^{\circ}$) the π^0 emission is somewhat oversubtracted, which pushes the cocoon coefficient negative, effectively renormalizing the sky background for the jet. As expected, the distribution of jet template coefficients (shown in Figure 5.11) is centered around zero, consistent with a Gaussian of mean zero and $\sigma = 0.044$. The Galactic jet coefficient is more than 4 sigma out of the background noise distribution, which is consistent with the estimated significance of the south jet derived from the covariance matrix of our Poisson likelihood fit. We interpret this agreement to mean that systematic errors in foreground modeling have not substantially distorted the meaning of the south jet's 4σ formal significance.

E range (GeV)	Energy	Uniform	SFD dust	Simple disk	Bubble	Bubble (1.6 yr)	South cocoon
$0.3 - 0.5$	0.4	1.376 ± 0.007	1.602 ± 0.019	0.451 ± 0.011	0.024 ± 0.020	0.035 ± 0.033	0.373 ± 0.055
$0.5 - 0.9$	0.7	1.175 ± 0.007	1.696 ± 0.019	0.458 ± 0.012	0.128 ± 0.021	0.211 ± 0.037	0.315 ± 0.060
$0.9 - 1.7$	1.3	0.897 ± 0.007	1.489 ± 0.019	0.383 ± 0.012	0.167 ± 0.022	0.321 ± 0.044	0.415 ± 0.066
$1.7 - 3.0$	2.2	0.734 ± 0.006	1.104 ± 0.016	0.324 ± 0.010	0.290 ± 0.018	0.436 ± 0.036	0.264 ± 0.054
$3.0 - 5.3$	4.0	0.562 ± 0.007	0.778 ± 0.017	0.249 ± 0.011	0.295 ± 0.021	0.353 ± 0.043	0.321 ± 0.064
$5.3 - 9.5$	7.1	0.500 ± 0.008	0.475 ± 0.020	0.170 ± 0.013	0.363 ± 0.025	0.343 ± 0.049	0.306 ± 0.078
$9.5 - 16.9$	12.7	0.392 ± 0.009	0.305 ± 0.023	0.117 ± 0.015	0.365 ± 0.030	0.205 ± 0.055	0.298 ± 0.094
$16.9 - 30.0$	22.5	0.287 ± 0.011	0.236 ± 0.026	0.111 ± 0.018	0.307 ± 0.035	0.263 ± 0.068	0.473 ± 0.119
$30.0 - 53.3$	40.0	0.244 ± 0.013	0.156 ± 0.030	0.028 ± 0.020	0.279 ± 0.041	0.217 ± 0.083	0.051 ± 0.125
$53.3 - 94.9$	71.1	0.169 ± 0.014	0.170 ± 0.036	0.014 ± 0.022	0.309 ± 0.050	0.251 ± 0.120	0.132 ± 0.152
$94.9 - 168.7$	126.5	0.130 ± 0.016	0.060 ± 0.039	0.014 ± 0.025	0.241 ± 0.057	0.319 ± 0.162	0.079 ± 0.180
$168.7 - 300.0$	225.0	0.086 ± 0.017	0.045 ± 0.040	-0.010 ± 0.027	0.040 ± 0.052	-0.015 ± 0.194	0.071 ± 0.173

Table 5.1: The template fitting coefficients and errors corresponds to Figure 5.5 and Figure 5.6. The gamma-ray luminosity in each energy range is shown in the unit of $\mathrm{keV\,cm^{-2}s^{-1}sr^{-1}}$. For comparison, we also listed the *Fermi* bubble luminosity from (Su et al. 2010).

5.8 Discussion and Conclusion

Given the alignment of the cocoon with the southern bubble edge, the cocoon/jet is probably associated with the bubble, and their origins may be intertwined. A possible scenario in which a jet creates both the cocoon and the *Fermi* bubble is as follows. The propagation of a large-scale relativistic jet may generate a double bow-shock structure at the head of the jet (Blandford & Rees 1974; Scheuer 1974). Entrained energy and matter are pushed aside due to a high pressure gradient and create a hot cocoon around the jet. The cocoon applies sufficiently high pressure to collimate the jet and substantially reduce its opening angle. Continuous injection of relativistic electrons can be produced in the forward, reverse, and re-collimation shocks emitting synchrotron radiation and gamma-ray IC emission. The jets deliver kinetic energy to the surrounding interstellar gas and the jet/medium interactions could be strong enough to accelerate particles and produce non-thermal radiation. In this scenario, as the jets emerge from the GC, they expand freely until they are recollimated when their ram pressure falls to the thermal pressure of the surrounding cocoon. The jet decelerates once the accumulated mass of the swept up ISM gas becomes similar to that carried by the jet. The cocoon and *Fermi* bubble could be explained by jet shocked material (re-confinement region and cocoon) and the ambient material shocked by the bow shock. However, the 15° misalignment between the jet/cocoon and the bubbles, and the absence of an obvious northern cocoon, suggest that this is not the whole story. We cannot rule out the possibility that the *Fermi* bubbles were formed by an earlier energetic event, while the jet might be produced more recently and be penetrating through the older structure.

The gamma-ray jet is the first collimated jet structure found in gamma-rays and the only collimated jet close enough to resolve with *Fermi*-LAT. The presence of such a large-scale Galactic jet in our Milky Way provides an ideal nearby laboratory for studying basic questions about jet formation, acceleration and collimation. It is likely that similar systems are not uncommon. For example, the recently observed unusual transient source (Swift J164449.3 + 573451) has been understood as a newly formed relativistic outflow launched by transient accretion onto a SMBH with mass similar to the Galactic center SMBH (Zauderer et al. 2011; Burrows et al. 2011). It provides the evidence that a normal galaxy can transform to an AGN-like phase and produce a relativistic jet. Similar structures on much larger scales have been found in galaxy clusters with radio lobes inflated by the jets of SMBH at the center of powerful radio galaxies (McNamara et al. 2005).

Follow-up observations at other wavelengths are required to advance our understanding of the jet and cocoon structures, and their relation to the *Fermi* bubbles. In coming years, *eRosita* will survey the whole sky in X-rays with approximately 30 times *ROSAT* sensitivity, in the medium energy X-ray range up to 10 keV with an unprecedented spectral and angular resolution (Cappelluti et al. 2011). It has the ability to reveal important information about the state of the material in the jet, cocoon and bubble structures. Such multi-wavelength exploration will advance our understanding not only of our own Galaxy, but of black hole accretion and jet formation in general.

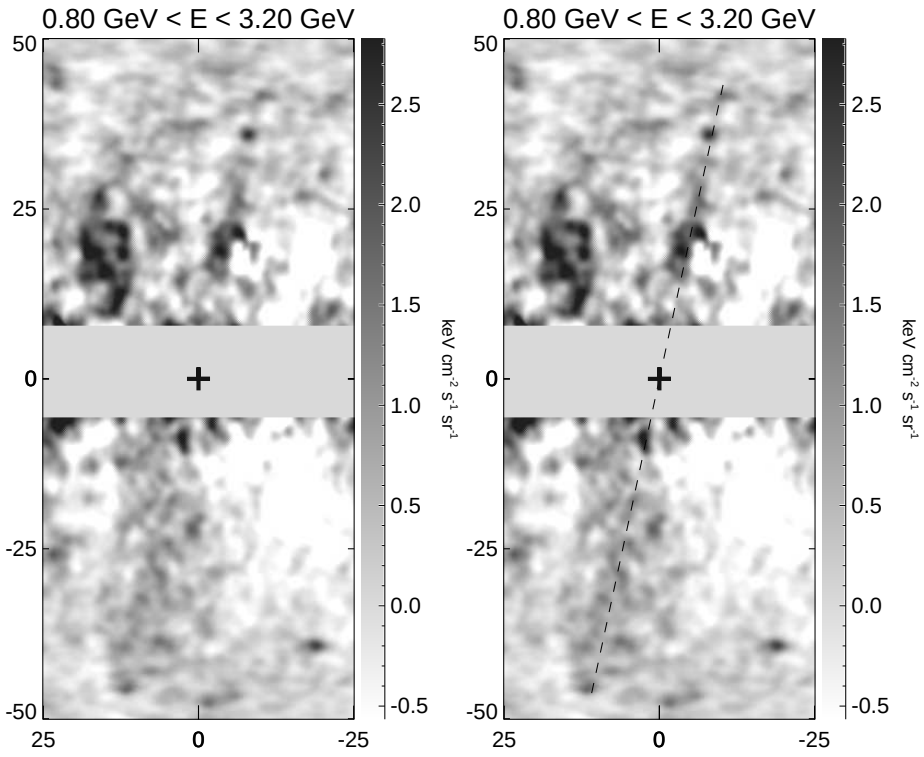

Figure 5.2.— We show gamma-ray maps in Galactic coordinate ($-50^\circ < b < 50^\circ, -25^\circ < \ell < 25^\circ$) from *Fermi*-LAT for photon energies 0.8−3.2 GeV. The Galactic center is marked with a cross sign in the center the maps. A pair of large-scale collimated jet-like features (the gamma-ray jets) are revealed. The *right* panel shows the same image as the *left* panel, but with a dashed line representing the direction of the suspected jet. Point sources have been subtracted based on the Second *Fermi*-LAT catalog (2FGL) (The Fermi-LAT Collaboration 2011a), and large sources, including the inner disk ($-5^\circ < b < 7^\circ$), have been masked. The maps are smoothed by a Gaussian kernel with FWHM of 2°. The *Fermi* diffuse Galactic model (Pass7_V6) has been subtracted to remove known large scale diffuse gamma-ray emission.

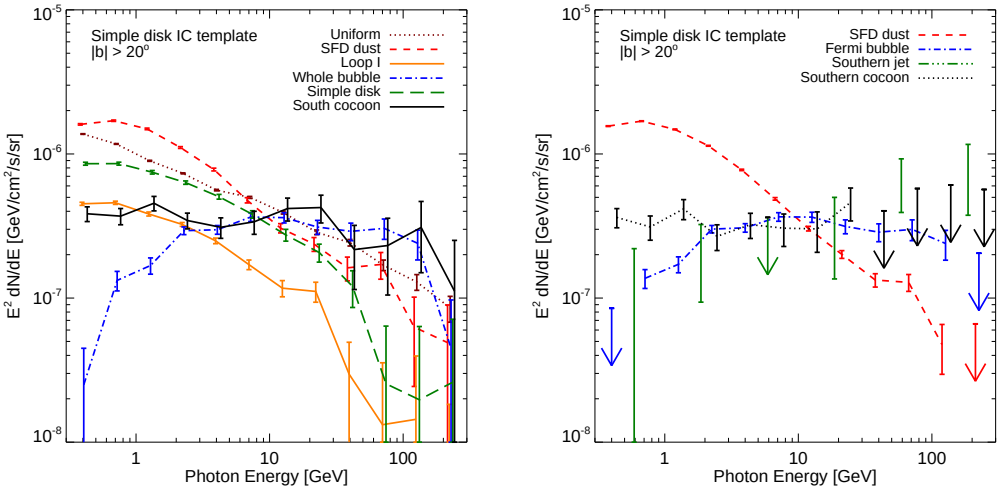

Figure 5.3.— *Left panel:* Spectral energy distribution of the components in our six-template fit. The dust-correlated spectrum (*red short-dashed line*), traces π^0 emission. The disk-correlated emission (*green dashed*), approximately traces the soft inverse Compton and bremsstrahlung components. The spectrum of the uniform emission (*dotted brown line*) includes the isotropic part of the extragalactic background and cosmic-ray contamination. The spectrum of emission correlated with *Loop I* (*solid orange*) has a spectrum similar to the disk-correlated emission. In contrast to these soft-spectrum components, the *Fermi* bubble template (*blue dot-dashed*) and the gamma-ray cocoon (*black solid*) have notably harder (consistent with flat) SEDs. Vertical bars show the marginalized 68% confidence range derived from the parameter covariance matrix for the template coefficients in each energy bin. *Right panel:* Same, but with one additional template representing the gamma-ray jet. For clarity, we only show the spectrum of the gamma-ray jet, the cocoon and the *Fermi* bubbles, and compare their spectra with the softer π^0 emission (*red dashed*).

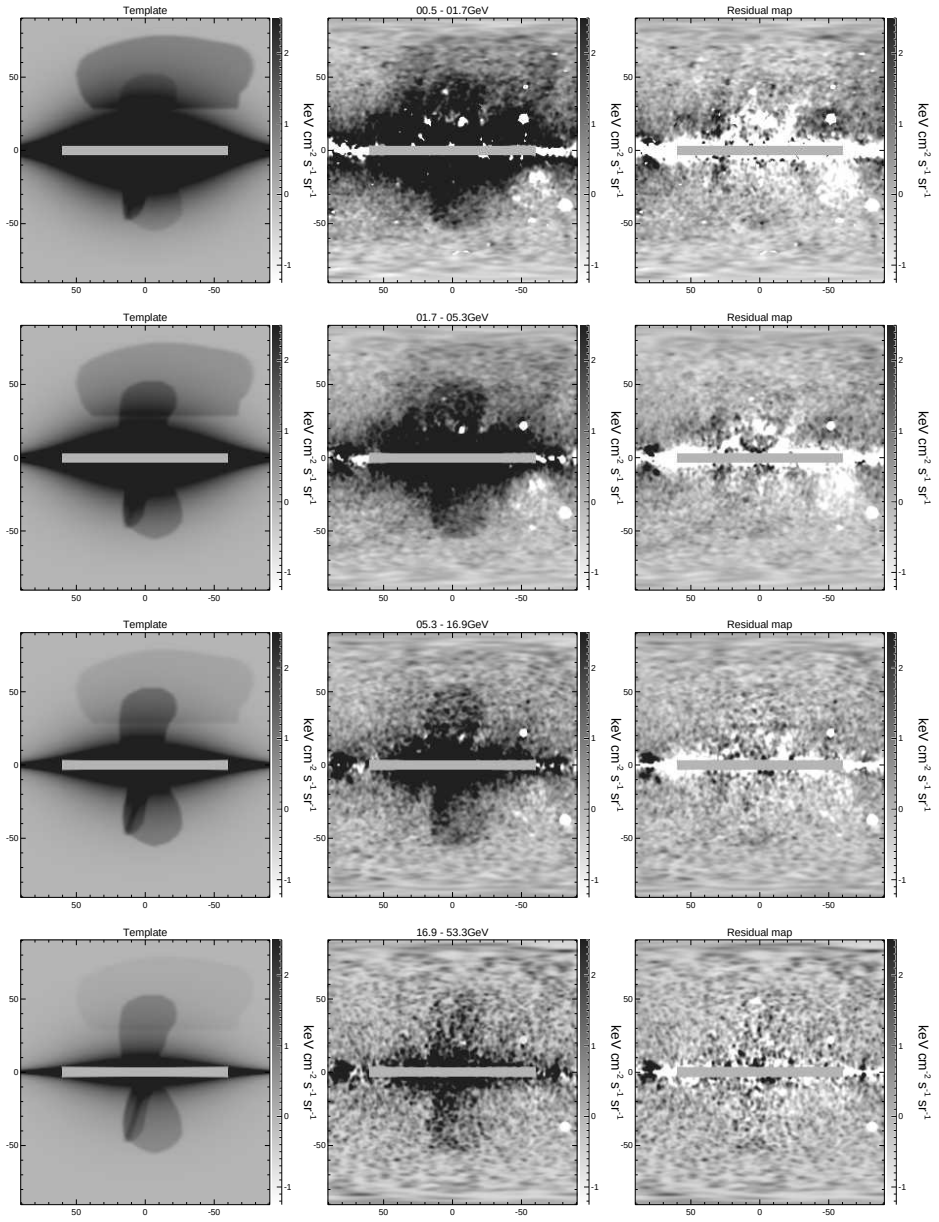

Figure 5.4.— This figure shows the best fit linear combination maps corresponding to the spectra in Figure 5.1.

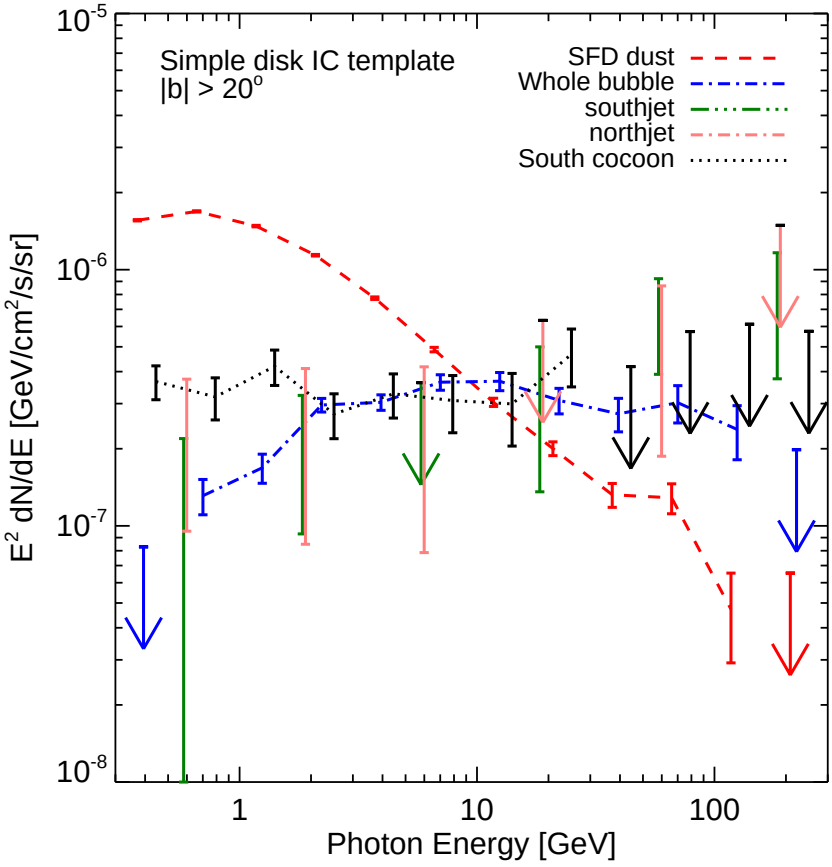

Figure 5.5.— This figure is the same as Figure 5.3, except with the north jet template added to the regression. The north and south jet spectra are noisy, but consistent with each other, and consistently hard. Note that the upper limit is shown for 3σ. The spectra plotted here are available in Table 5.1 and Table 5.2.

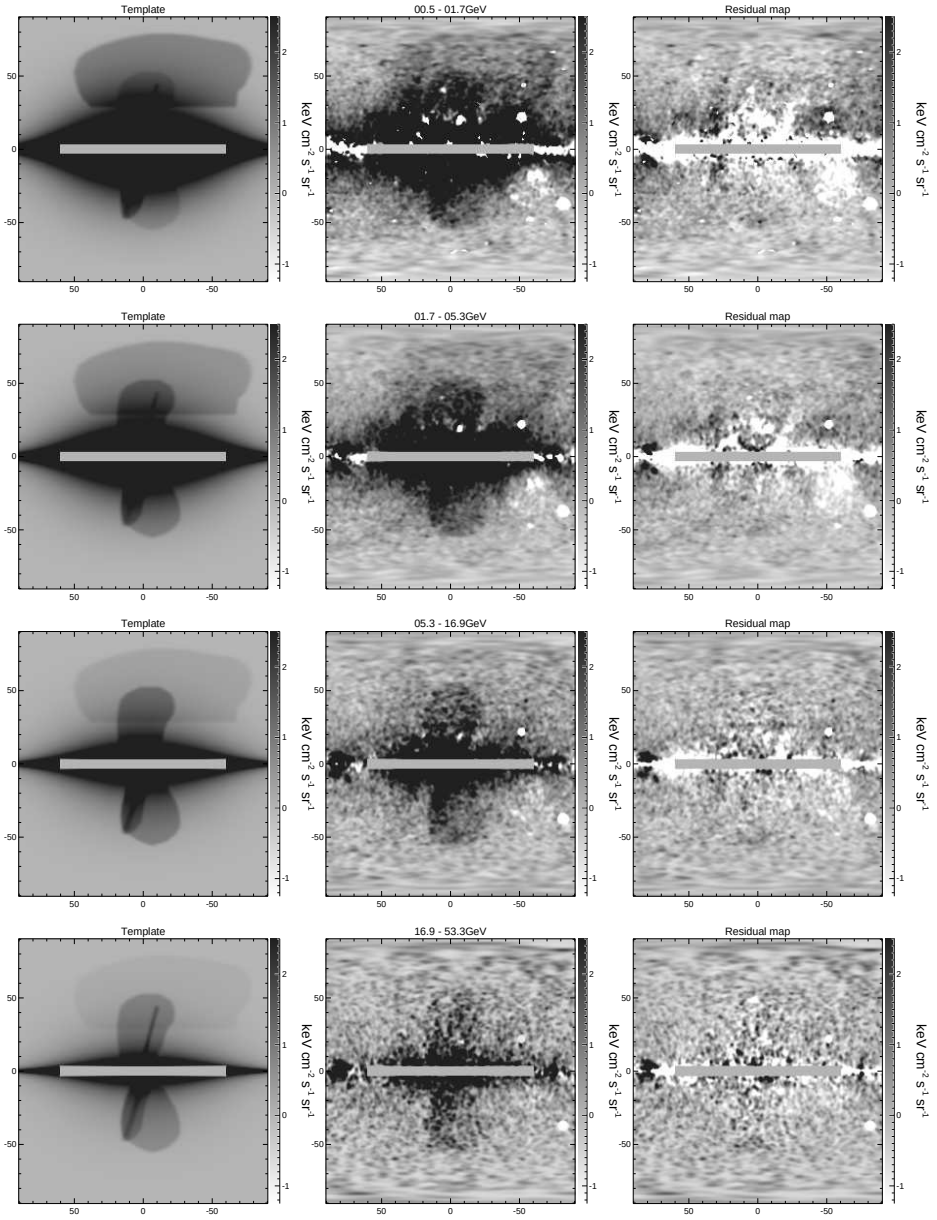

Figure 5.6.— Same as the Figure 5.4, except we include the north jet template.

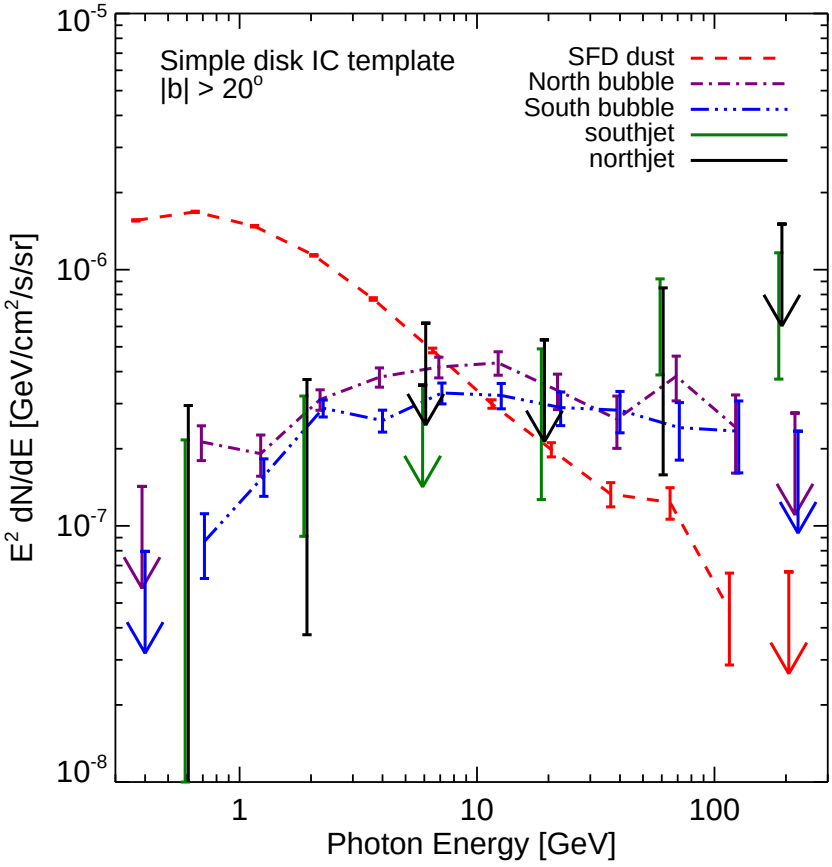

Figure 5.7.— Same as Figure 5.1, except we add the north jet template and split the *Fermi* bubble into north and south bubbles separately. The south cocoon template is included in the fit. The north and south jet spectra are consistently hard. The fitting results are not significantly effected by the bubble template splitting.

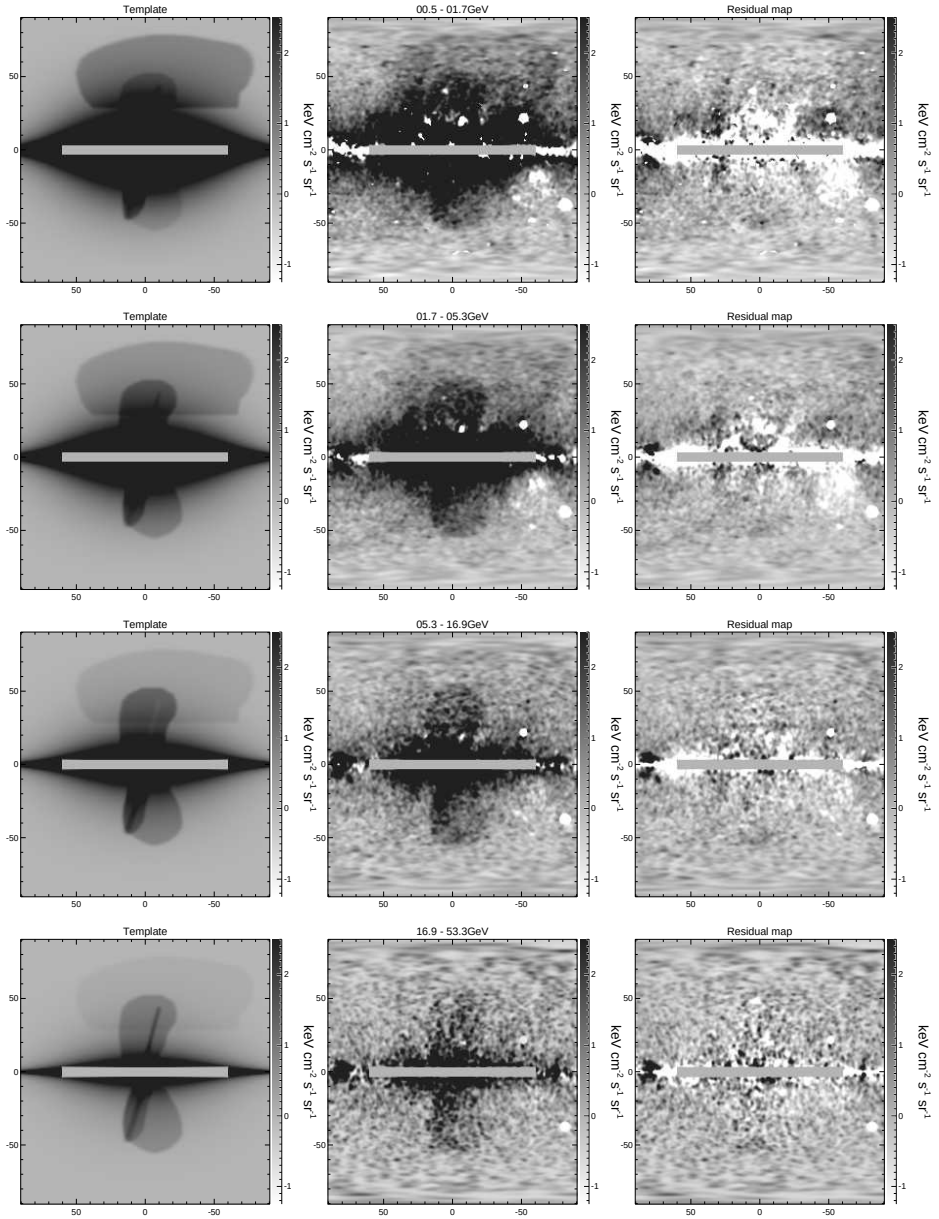

Figure 5.8.— Same as Figure 5.1, except we add the north jet template and split the bubble template to north and south separately. Note that the south cocoon template is included in the fitting. The north and south jet spectrum is consistently hard.

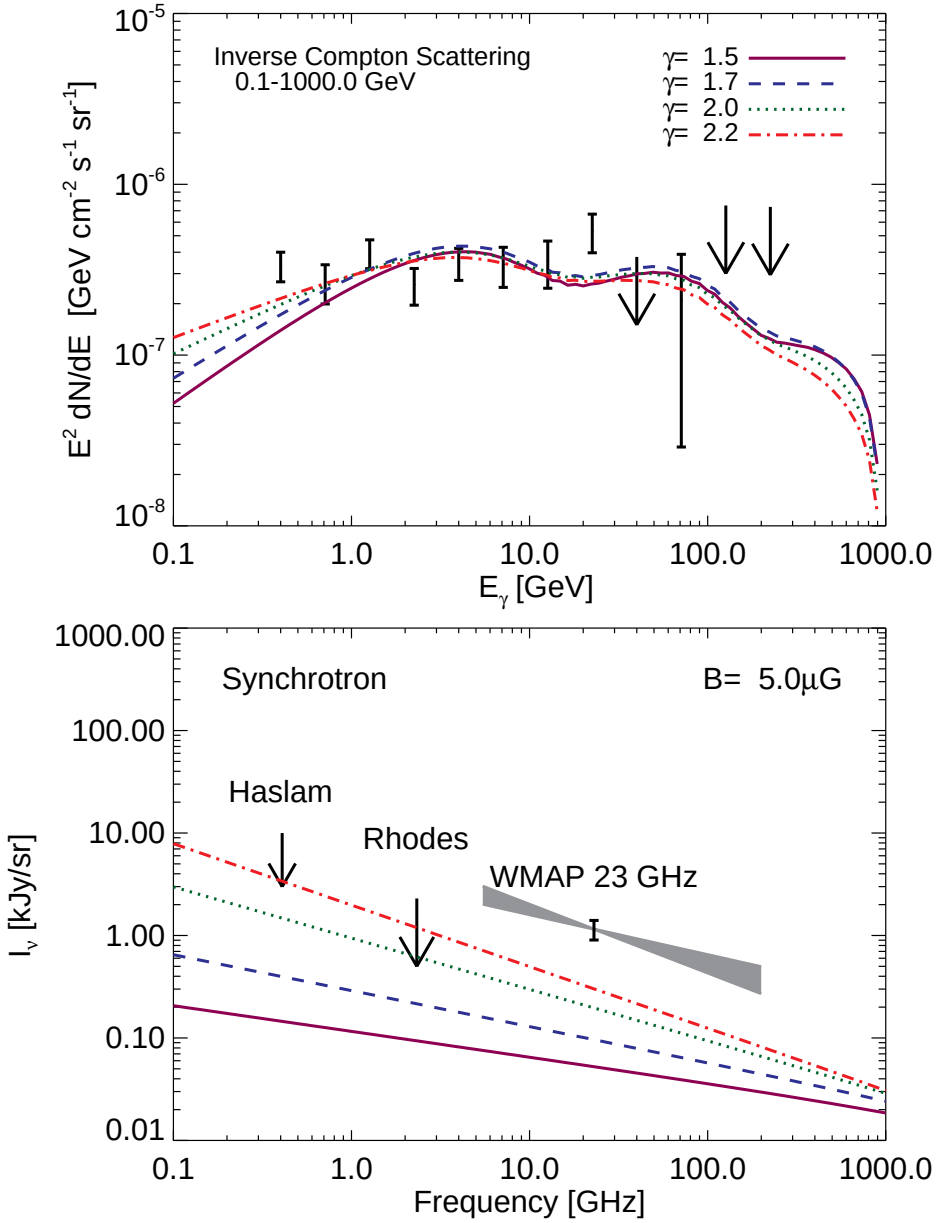

Figure 5.9.— The estimated spectrum of inverse Compton gamma-rays (*upper panel*) and corresponding synchrotron radiation (*lower panel*) originating from a hard electron spectrum along a line of sight 4 kpc below the Galactic plane (i.e. $b \approx -25°$). The steady-state electron spectrum is taken to be a power law, $dN/dE \propto E^{-\gamma}$, with index $\gamma = 1.5$ (*solid black*), 1.7 (*blue dashed*), 2.0 (*green dotted*), and 2.5 (*red dash-dotted*) in both the upper and lower panels. In all cases the cosmic ray electron has a range of [0.1, 1000] GeV.

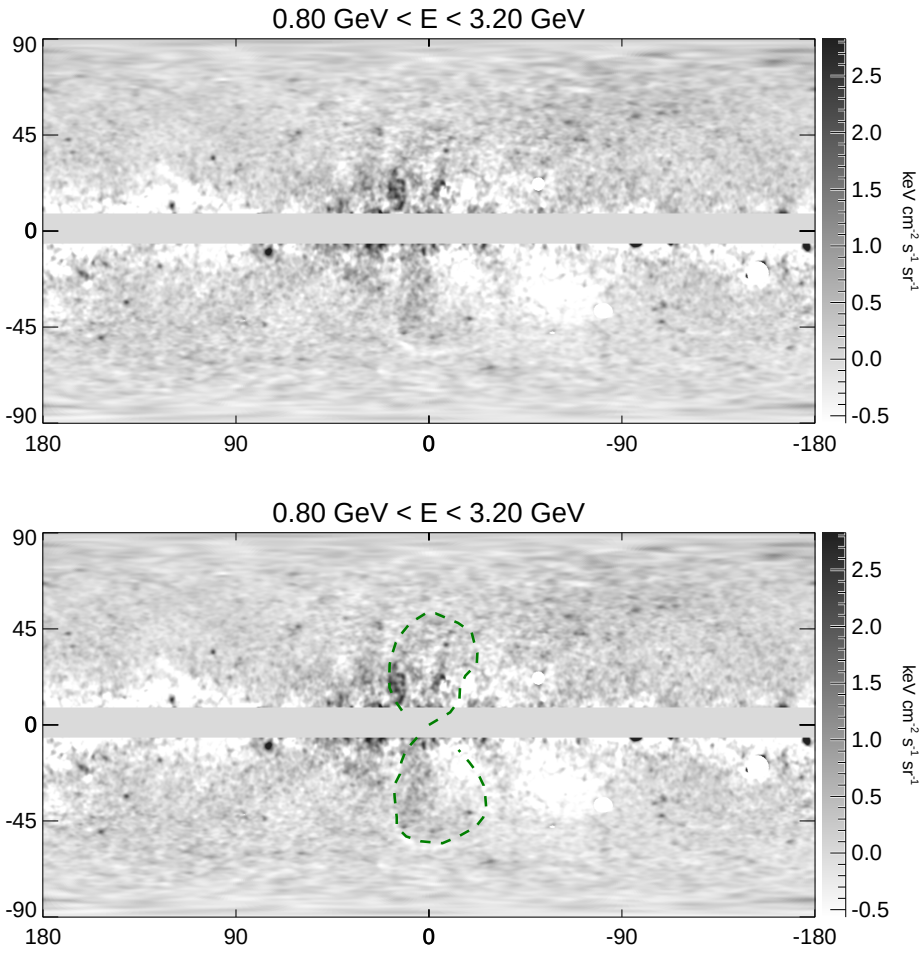

Figure 5.10.— Full sky residual maps after subtracting the *Fermi* diffuse emission model from the *Fermi*-LAT three year gamma-ray maps. *Upper panel:* Point sources have been subtracted, and large sources, including the inner Galactic disk, have been masked.

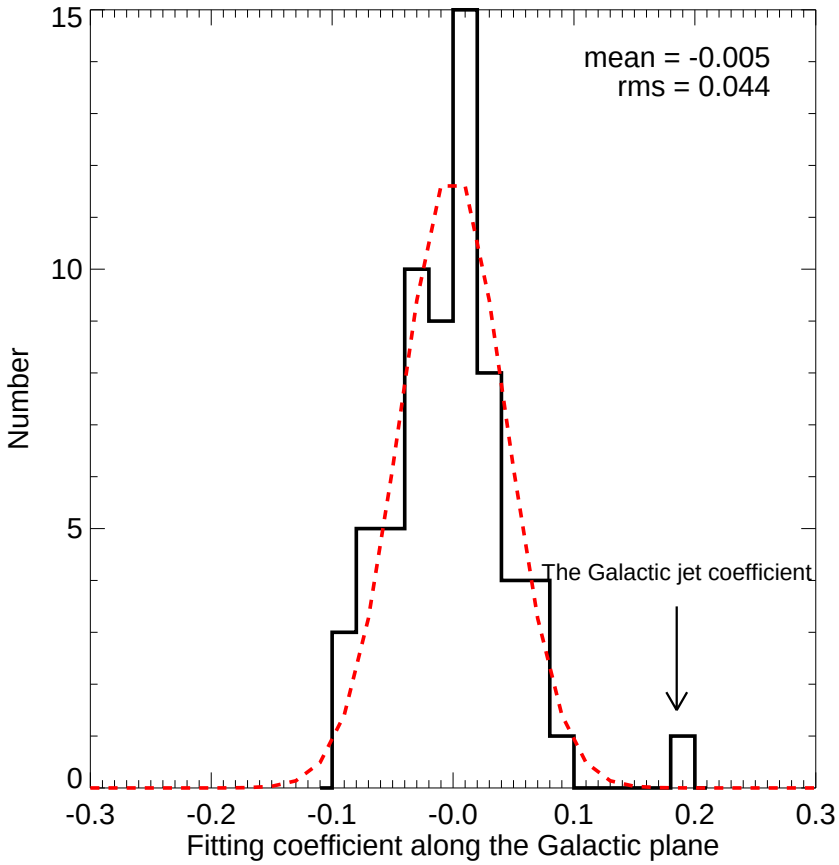

Figure 5.11.— As a verification of our uncertainty estimate for the Galactic jet structure, we have rotated the south jet and cocoon templates in longitude around the sky, and determined the best fit coefficient for each case. This histogram shows the distribution of the coefficients overplotted with the fitted Gaussian distribution. The coefficient distribution is well centered around zero and well fitted with a Gaussian noise distribution. The south jet template with a coefficient 0.182 is about 4σ significance from the background noise estimation. The estimated uncertainty of the jet template agrees well with our estimation of the significance of the south jet based on the Poisson likelihood fitting.

E range (GeV)	Energy	North jet	South jet
$0.3 - 0.9$	0.6	0.235 ± 0.139	0.107 ± 0.112
$0.9 - 3.0$	1.8	0.248 ± 0.163	0.208 ± 0.115
$3.0 - 9.5$	5.6	0.248 ± 0.170	0.002 ± 0.120
$9.5 - 30.0$	17.6	-0.036 ± 0.223	0.318 ± 0.182
$30.0 - 94.9$	55.6	0.526 ± 0.339	0.656 ± 0.266
$94.9 - 300.0$	175.7	0.151 ± 0.446	0.770 ± 0.395

Table 5.2: The template fitting coefficients and errors of north and south jet correspond to Figure 5.5 and Figure 5.6. The gamma-ray luminosity in each energy range is shown in the unit of $\mathrm{keV\,cm^{-2}s^{-1}sr^{-1}}$.

Chapter 6

Fermi Bubbles Revisited with Three Year Fermi-LAT Data

In this chapter, we present an updated analysis of the Fermi bubbles using three years of Fermi-LAT data, improved event selection, and improved analysis tools.

In Chapter 6.1 we describe the *Fermi*-LAT data selection and our data analysis procedure including map making. In Chapter 6.2, we discuss the different Galactic diffuse gamma-ray models we have used for removing foregrounds. In Chapter 6.3 and Chapter 6.4 we show the gamma-ray maps constructed from three-year *Fermi*-LAT observations, and reveal the *Fermi* bubble features and show that they are robust when different models for the expected Galactic diffuse emission are subtracted. We characterize the morphology of the bubbles in some detail and employ regression template fitting to reveal a hard, spatially uniform spectrum for the gamma-ray emission associated with the bubbles. Finally in Chapter 6.5, we discuss the implications of the *Fermi* bubbles and possible scenarios to produce

the gamma-ray bubbles, with emphasis on the origin of the electron CRs and the challenges in explaining the spectral and spatial profiles of the gamma-ray emission from the bubbles.

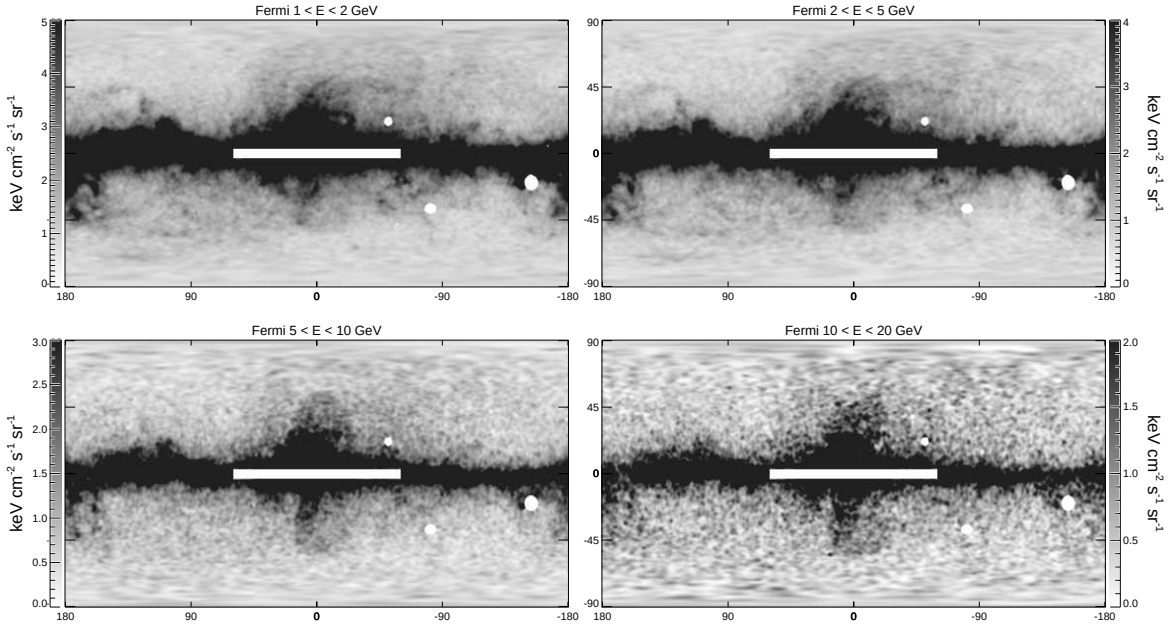

Figure 6.1.— All-sky *Fermi*-LAT three year maps for photon energies in 4 different bins ranging from 1 to 20 GeV. Point sources have been subtracted based on the Second *Fermi*-LAT catalog (2FGL), and large sources, including the inner disk ($-2^\circ < b < 2^\circ, -60^\circ < \ell < 60^\circ$), have been masked. To make diffuse emission more visible, these maps have been smoothed with a Gaussian kernel of σ=120 arcmin.

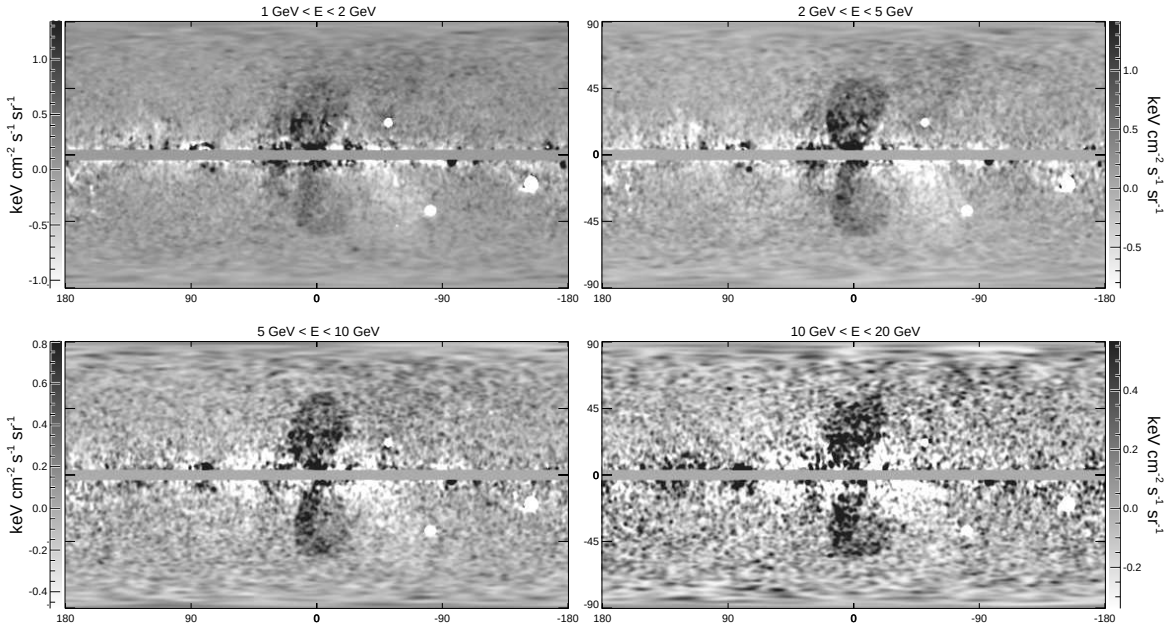

Figure 6.2.— All-sky residual maps after subtracting the *Fermi* diffuse Galactic model (P6V11) from the LAT three year maps in 4 energy bins (see Chapter 6.2.1). Two bubble structures extending to $|b| \sim 50^\circ$ appear above and below the GC, symmetric about the Galactic plane. The *Fermi* diffuse Galactic model is binned and smoothed in the same manner as the real data.

6.1 Improved *Fermi* Data Analysis and Map Making

6.1.1 *Fermi* Three Year Data Selection

In this subsection, we describe our improved data selection procedure. The selected photon events with energy from 300 MeV to 300 GeV are binned into full sky maps using HEALPix, a convenient iso-latitude equal-area full-sky pixelization widely

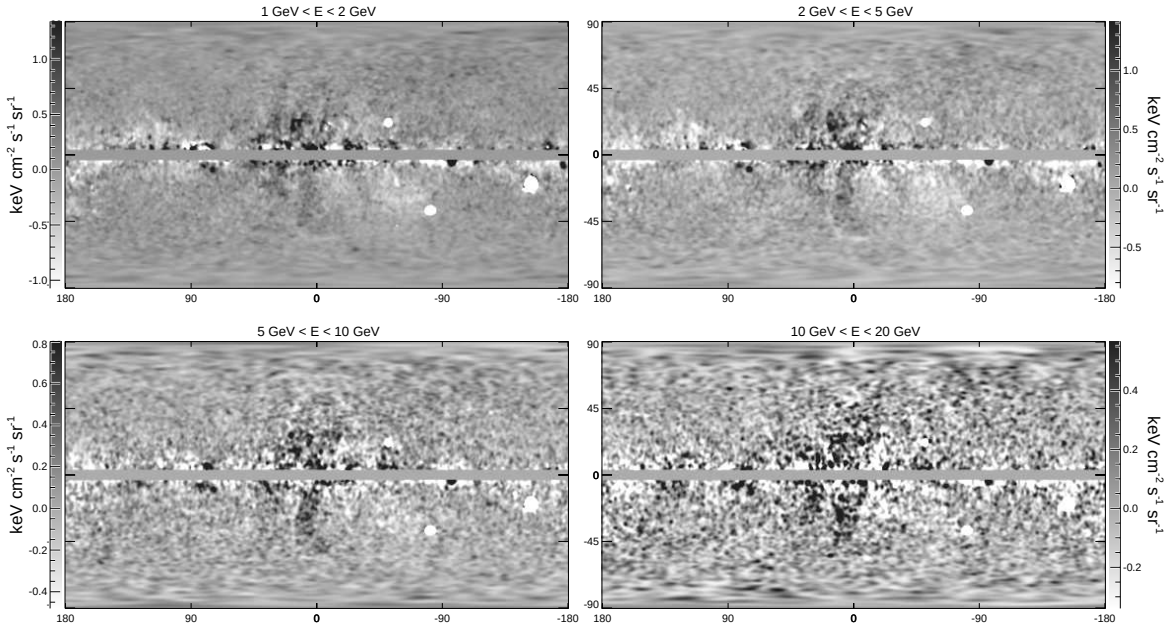

Figure 6.3.— All-sky residual maps after subtracting the *Fermi* diffuse Galactic model of P7_V6 in 4 energy bins from *two years* Fermi-LAT data (see Chapter 6.2.1). No apparent bubble structure are seen in this residual maps.

used in the CMB community.[1] Spherical harmonic smoothing is straightforward in this pixelization, and we smooth each map by the appropriate kernel to obtain a Gaussian PSF of 2° FWHM. Due to the rapid change of effective area with energy below 100 MeV, the residual instrument uncertainty may not be properly treated by the `Fermi Science Tools` and may cause spurious spectral features. Because the PSF of the initial map must be smaller than this, at energies below 1 GeV we use only front-converting events as they have a smaller FWHM than back converting

[1]HEALPix software and documentation can be found at `http://healpix.jpl.nasa.gov`, and the IDL routines used in this analysis are available as part of the IDLUTILS product at `http://sdss3data.lbl.gov/software/idlutils`.

events. A larger smoothing scale would help improve S/N, but a relatively small smoothing scale is necessary to see sharp features (such as the bubble edges). Furthermore, for the comparisons and linear combination analysis described in e.g. Chapter 6.2.3, it is necessary to smooth the maps at each energy to a common PSF. We generate maps from $1 - 4^\circ$, and find that a FWHM of 2° works well for morphological/spectral study on map domain, however we decide to use FWHM of 90 arcmin maps for the purpose of showing the sharp edge of the bubbles[2].

We make use of the first three year data products of *Fermi* Pass 7 (`P7`) event reconstruction algorithms which were developed based on post-launch information using flight data[3]. The main advantages of `P7` include improved estimation of instrument effective area and photon/cosmic ray seperation, inclusion of azimuthal and livetime dependence of the instrument effective area, and the new PSF derived by fitting the width of stacked bright point sources.

Fermi provides two classes of event selection that might be appropriate for diffuse emission, CLEAN and ULTRACLEAN. We must balance the need for low background provided by ULTRACLEAN with the larger effective area provided by CLEAN. We performed our analysis with both maps and find better results (smaller uncertainties at high energy) with ULTRACLEAN.

[2]See Dobler et al. (2010) and Su et al. (2010) for details on map construction, smoothing, masking, and for instructions on how to download the maps.

[3]Which is an update of the Pass 6 used in our previous analysis Su et al. (2010). Please refer to `http://fermi.gsfc.nasa.gov/ssc/data/analysis/documentation/Pass7_usage.html` for more details.

6.1.2 Map Making with Update Software

We produce the exposure maps by using the `gtltcube` function of `Fermi Science Tools` and `gtexpcube2` to generates a set of exposure maps for different energy bins, multiplying effective area by exposure, and integrating over solid angle. The updated analysis tool accounts for the inclination angle phi-modulation of the effective area for the IRFs that implement this dependence by setting `phibins`, instead of using the phi-averaged effective area.[4]. The LAT instrument response functions (IRF) depend on the photon inclination angle, thus the total detected number of photon counts is a function of the duration of observations depending on various inclination angles. The sky position and inclination angle information is available from the spacecraft files.

The version of gamma-ray maps (v3_3) constructed and used in this chapter from the three year *Fermi* data have greater signal/noise and significantly lower background compared to the previously released v2_3 maps in Chapter 2. As in Su et al. (2010), we construct maps of front-converting and back-converting events separately, smooth to a common PSF, and then combine them. To reveal the diffuse emission, we subtract point sources from the maps. The point source subtraction has been improved from the previous analysis Su et al. (2010): we use the Second *Fermi*-LAT catalog (2FGL, The Fermi-LAT Collaboration (2011b)) based on 24 months of LAT observations containing 1873 sources detected and characterized in the 100 MeV to 100 GeV energy range[5], as the successor of the LAT Bright Source

[4]We compute the energy layers at the center of the count map ebounds by setting `bincalc=CENTER`

[5]The Available from `http://fermi.gsfc.nasa.gov/ssc/data/access/lat/2yr_catalog`. The

list (Abdo et al. 2009a) and the First Fermi LAT (1FGL, Abdo et al. (2010b)) catalogs, which were based on 3 months and 11 months of flight data, respectively. Source detection of 2FGL is based on their average fluxes. For the calibration and the improved analysis techniques leading to updates to the 2FGL catalog, please refer to (The Fermi-LAT Collaboration 2011b). The 2FGL analysis also takes advantage of the accompanying set of the newly released Pass 7 event selections and the parameterized IRFs[6], rather than the Pass 6 event selections. This catalog also employed a new diffuse Galactic emission model, in which the *Fermi* bubbles were involved as a seperate large scale diffuse template. Furthermore, the source association process has been also improved. The point-spread function (PSF) and effective area of the *Fermi*-LAT varies with energy, and we subtract each point source from the maps in each energy bin, using the in-flight verion of the PSF contained in the newly released IRFs.

At lower energies the angular resolution of the PSF is limited by multiple scattering, and at high energies by the spatial resolution of the Silicon tracker system. The PSF also depends on the angle at which a photon enters the LAT; because of the scan strategy, photons from the orbital poles arrive with a different distribution of angles than photons from the equator. Therefore, in principle the average PSF varies across the sky. It has been known that the PSF derived from pre-flight calibration and Monte Carlo simulations is under-estimated at energies of a few GeV, and this version (P6_V3) of the PSF has been used in our previous

file we used is `gll_psc_v06.fit`

[6]http://fermi.gsfc.nasa.gov/ssc/data/analysis/documentation/Cicerone/Cicerone_LAT_IRFs/

analysis (Su et al. 2010). The new technique has been developed to characterize the PSF using *Fermi* in-flight data. However, this new technique required a large integration time on the sources. As a result, the in-flight version of the PSF uses the same PSF parameters for different photon inclination angles at a given energy. For the analasis in this chapter, we use this in-flight version of the PSF in the modeling, instead of choosing the spatially varied PSF[7]. The in-flight version of the PSF provides unbiased results for long observation times, since the maps we construct contain integrated three-year long observation times provided by *Fermi*, we observe each direction with a distribution of observing angles, the inclination angle dependence of the PSF is effectively included in our analysis[8]. Non-uniformities in the averaged PSF will neither over nor underestimate the true containment in any significant manner[9].

For the 400 brightest and 400 most variable sources, the subtraction is noticeably imperfect, so we interpolate over the core of the PSF after subtracting the best estimate. We take care to expand the mask for very bright sources (Geminga, 3C 454.3, and LAT PSR J1836+5925). The resulting map is appropriate for diffuse work at $|b| > 3^\circ$. At $|b| < 3^\circ$ the maps are severely compromised by the poor subtraction and interpolation over a large number of point sources. Further details of the map processing may be found in Dobler et al. (2010) and Su et al. (2010). The v3_3 maps

[7]The version we used is `v9r23p1` with the addition of the Pass 7 instrument response functions.

[8]The inclination from the LAT boresight is included in the IRFs as an average weighted over two years of observations from the `Fermi science tools`

[9]Please see more detailed discussion of the PSF of the contained in *Fermi* IRF P7_V6 in `http://fermi.gsfc.nasa.gov/ssc/data/analysis/documentation/Cicerone/Cicerone_LAT_IRFs/`

used in this chapter and color versions of the map are available for download[10].

Due to the difficulty of no standard astronomical sources with sufficiently well known and sharp spectral features to allow an absolute calibration of the LAT energy scale, the LAT team uses the geomagnetic cutoff in the cosmic ray electron-plus-positron (CRE) spectrum in low earth orbit to obtain several calibration points between ∼6 to ∼13 GeV with an estimated uncertainty of 2% (The Fermi LAT Collaboration 2011). Such high accuracy energy calibration reduces the systematic uncertainty in LAT measurements of the spectral features seen in the emission from *Fermi* bubbles.

6.2 Galactic Gamma-ray Diffuse Emission Models

The diffuse gamma rays observed by *Fermi* are dominated by photons from the decay of π^0 particles, produced by the collisions of CR *protons* with Galactic ambient ionized gas and dust in the ISM, with contributions from bremsstrahlung radiation from collisions of high energy CR *electrons* with the ISM and IC emission by interaction with ISRF. The *Fermi* all-sky gamma-ray maps from three years of observation with LAT are shown with different energy bands in Figure 6.1. Both the north and the south *Fermi* bubble can be seen towards the inner Galaxy, above and below the Galactic center, especially at higher energy where the bubbles are brighter relative to other diffuse gamma-ray components. In order to uncover the *Fermi* bubble features better, significant π^0 emission, bremsstrahlung, and IC emission from

[10]Available at `http://fermi.skymaps.info`

the Galactic disk must be removed. We take three approaches (different foreground templates construction) for the foreground removal (same as Chapter 2). One is to use the *Fermi* Diffuse Galactic Model provided by the *Fermi* team[11](Chapter 6.2.1). The second approach employs a linear combination of templates of known emission mechanisms (Chapter 6.2.2), using existing maps from multiwavelength observations and/or constructed geometric templates. The third approach is taking advantage of the lower energy band $0.5 - 1.0$ GeV *Fermi* map to form a template of a diffuse emission model (Chapter 6.2.3).

6.2.1 Update *Fermi* Diffuse Galactic Model

The LAT Galactic diffuse model provided with the `Fermi Science Tools` publicly available from the `Fermi Science Support Center` (FSSC)[12] is a comprehensive model of Galactic gamma-ray emission from the ISM. This model is constrained by fitting gamma-ray and microwave observations, locally measured CR spectra, etc. In this model, the π^0 emission as a function of the gas and the proton CR distribution is modeled with maps of interstellar gas: H I from the Leiden/Argentine/Bonn (LAB) Galactic Survey (Kalberla et al. 2005) and CO from the CfA composite CO survey (Dame et al. 2001). Both the H I and CO surveys contain velocity information which allows the emissivity of the gas to vary with Galactocentric radius to derive the distribution of interstellar gas in Galactocentric rings. This freedom also allows for varying amounts of bremsstrahlung (with varying spectrum) which also scales

[11]See `http://fermi.gsfc.nasa.gov/ssc/data/access/lat/BackgroundModels.html`

[12]`http://fermi.gsfc.nasa.gov/ssc`

with the ISM density. The contribution from IC is modeled with an IC component generated by the GALPROP cosmic ray propagation code. GALPROP calculates the steady state solution to the diffusion-energy-loss equation, given the 3D gas distribution, interstellar radiation field, B-field model, CR diffusion assumptions, and many other input parameters (Strong & Moskalenko 1999; Strong et al. 2009, 2007). The diffuse model is the key connection between the input assumptions and the observables, and is essential for interpretation of the *Fermi*-LAT data. It is important to make it as complete as possible.[13].

The Fermi diffuse model is primarily designed as a background template for point source analysis or investigation of small-scale diffuse structures, and comes with a number of caveats. However these caveats apply mainly near the Galactic plane, and at $E > 50\,\mathrm{GeV}$. It is nevertheless useful for qualitatively revealing features in the diffuse emission at high latitude. In Figure 6.3, we show the residual maps after subtracting the *Fermi* diffuse Galactic model (gll_iem_v02_P6_V11_DIFFUSE) in different energy bins. A double-lobed bubble structure is clearly revealed, with similar morphology in the different energy bins. There are no other apparent large scale features appearing in the residual maps. We note that the bubble is neither limb brightened nor centrally brightened, consistent with a flat *projected* intensity distribution.

Recently, along with the new P7 data products, an updated version of the Fermi diffuse model has been released (gal_2yearp7v6_v0). This new model is based on 24

[13]A description of this diffuse emission model is available at fermi.gsfc.nasa.gov/ssc/data/access/lat/ring_for_FSSC_final4.pdf

months of LAT data, with sources removed based on preliminary 2FGL source list. The resulting model contains full sky diffuse gamma-ray emission estimation of 30 energy bands, ranging from 50 MeV to 600 GeV. Compare with the last released version (`gll_iem_v02_P6_V11_DIFFUSE` in Pass 6 data product), this new released model (`gal_2yearp7v6_v0`) including the *Fermi* bubbles as a new component have been incorporated in the model as a dedicated template along with other large-scale regions of excess emission. The bubble template has uniform intensity whose shape correspond roughly to the edge of the bubbles, which is the same as Su et al. (2010). The loop I feature was modeled as two independent templates, the North Polar Spur region was based on the Haslam 408 MHz map, and the diffuse excess within the loop I region was modeled with a template with constant intensity in this region. The model for the Galactic diffuse emission was developed using updated H I map and updated GALPROP-derived IC template. Infrared tracers of dust column density were used to correct column densities in directions where the optical depth of HI was either over or under-estimated. The model of the diffuse gamma-ray emission was then constructed by fitting the gamma-ray emissivities of the rings in several energy bands to the LAT observations (after removal of the point sources). The fitting also required a model of the inverse Compton emission calculated using `GALPROP`[14] and a model for the isotropic diffuse emission.

[14] `http://galprop.standford.edu`

6.2.2 Simple Template-Based Diffuse Gamma-ray Model

The π^0/bremsstrahlung gamma-ray intensity is proportional to the ISM density $\times$ the CR proton/electron density integrated along the line of sight. As long as the CR proton/electron spectrum and density are approximately spatially uniform, the ISM column density is a good tracer of the resulting gamma-ray distribution from π^0/bremsstrahlung emission. The dominant Galactic gamma-rays originate from π^0 gammas produced by CR protons interacting with the ISM, largely removing the π^0 gammas can better reveal the *Fermi* bubble especially close to the Galactic plane. The the ISM column density should be morphologically correlated with other tracers of the ISM. *Fermi* diffuse model used H I and CO maps as tools to trace the gas distribution (Chapter 6.2.1). Another good candidate is the SFD map of Galactic dust, based on 100 μm far IR data (Schlegel et al. 1998). The dust map has some advantages over gas maps (see discussion in Chapter 2.2.1). One shortcoming of using H I and CO maps is the existence of "dark gas" (Grenier et al. 2005), clouds with gamma-ray emission that do not appear in the H I and CO surveys. These features are seen in dust maps (Schlegel et al. 1998) and may simply be molecular H clouds underabundant in CO. The goal is to remove the expected diffuse gamma-rays from our Fermi three year maps in a fashion that with as few physical assumptions as possible, to better reveal the *Fermi* bubble structure.

In Figure 6.4, we show the full sky residual maps at energy ranging $1 - 100$ GeV to best reveal the *Fermi* bubble features from *Fermi*-LAT three year data. We use the SFD dust map as a template of the π^0 gamma foreground. The correlation between *Fermi* and SFD dust is striking, and the most obvious features are removed

by this subtraction. To reveal the structure deeper into the plane, a simple disk model is subtracted (Su et al. 2010)[15]. The disk model mostly removes the IC gamma-rays produced by cosmic ray electrons interacting with the ISRF including CMB, infrared, and optical photons; such electrons are believed to be mostly injected in the Galactic disk by supernova shock acceleration before diffusing outward. Although photon Poisson noise is much greater in the higher energy maps, we can see brighter *Fermi* bubble structure both above and below the Galactic plane relative to other large scale diffuse gamma-ray components.

6.2.3 Low Energy Fermi Map as a Diffuse Galactic Model

We have introduced the Galactic diffuse gamma-ray template using low energy maps constructed from *Fermi* data (Chapter 2.2.1). In Figure 6.5, we show the $0.5 - 1$ GeV and $2 - 50$ GeV residual maps after subtracting only the SFD dust map as a template of foreground π^0 gammas. The residual maps should be dominated by IC emission from CR electrons interacting with the ISRF. We use the $0.5 - 1$ GeV maps as a template of IC emission from high energy electrons scattering *starlight*, and subtract the template from higher energy maps (the *lower panels* of Figure 6.5). The *Fermi* bubble structures are clearly revealed. We thus conclude that the *Fermi* bubbles are mostly from high energy electron CRs IC scattering on CMB photons, and IR photons at higher energies. By comparing the *Fermi* diffuse model (Figure 6.3) with our simple template model subtraction (Figure 6.4), we find that the

[15]The functional form of this disk template is $(\csc|b|) - 1$ in latitude and a Gaussian ($\sigma_\ell = 40^\circ$) in longitude

bubble structures are robust to quite different foreground subtractions. It is difficult to see how such emission could arise – especially with sharp edges – as an artifact of these subtractions.

6.3 *Fermi* Bubbles from Three Year LAT data: Morphology

In this section, we discuss more in detail about the revealed morphology of *Fermi* bubbles. In the *right* panels of Figure 6.4, we illustrate the edges of the *Fermi* bubbles and some other large scale features we found in the three year gamma-ray maps. The *Fermi* bubbles show distinct sharp edges, clearly not smoothly falling off further from the disk, as modeled in Dobler et al. (2010). Besides the two bubbles, on a even larger scale, we confirm the diffuse loop I features we identified in Su et al. (2010), a fainter structure compared with the bubbles extended up to $b \sim 80^\circ$, with ℓ ranging from roughly -80° to 50°. Part of this large extended loop I structure share similar morphology with the famous *North Polar Spur* emission associated with *Loop I* found in radio observations over decades (as seen for example in the Haslam 408 MHz map Haslam et al. 1982a). We still see one giant *northern arc* that embraces about half of the north bubble, that extends from the disk up to $b \sim 50$, with ℓ ranging from roughly -40° to 0°. Although at lower latitude, this feature overlaps with the loop I feature, it has brighter and sharper edges in the $1 - 5$ GeV map, espectially towards higher latitude and lower longitude.

In Figure 6.6 we compare the *Fermi* bubble morphology in different energy

bins. We show the difference of the $1-2$ and $2-5$ GeV residual maps in the *upper panels*; each residual map is the result of subtracting the SFD dust map and the simple disk model to best reveal the *Fermi* bubbles. The difference maps between the $1-5$ and $5-50$ GeV maps are shown in the *lower panels*. The bubble features almost disappear in the difference maps, indicating that different parts of the *Fermi* bubbles have similar spectra.

We note that the flat intensity of the bubbles is striking. If we assume that the *Fermi* bubbles are projected from spherically symmetric three-dimensional bubbles centered above and below the GC, a non-trivial emissivity distribution in the bubble interior is required to produce a flat projected intensity distribution (Su et al. 2010). If the "bubbles" originate from IC scattering, this suggests a rather non-uniform density distribution for the electron CRs, which – combined with a nearly uniform spectral index – presents challenges for many models for the electron injection. The expected intensity profile for a shock generated bubble with a compressed gas shell is limb-brightened, in contrast to observations too.

To study the sharp edges of the bubbles at high latitude more carefully, we examine the (projected) intensity profiles along arcs of great circles passing through the estimated centers of the north and south bubbles, and intersecting the bubble edge (as defined in Figure 6.4) at $|b| > 28°$. Along each such ray, we define the intersection of the arc with the bubble edge to be the origin of the coordinate system; we then perform an inverse-variance-weighted average of the intensity profile along the rays (as a function of distance from the bubble edge). We subtract a constant offset from the profile along each ray, prior to averaging the rays together, to minimize aliasing of point sources onto the averaged profile,

and then add the averaged offset back in at the end. The inverse variance for each data point is obtained from the Poisson errors in the original photon data, prior to any subtraction of point sources or templates (however, the smoothing of the map is taken into account). When the rays are averaged together, the naive inverse variance in the result is multiplied by a factor of the annulus radius (for the points being averaged together) divided by $4\pi\sigma^2$, where σ is the 1σ value of the PSF, and the annulus width is taken to be 1° (the spacing between the points along the rays; this is comparable to the smoothing scale, so there may still be unaccounted-for correlations between the displayed errors); this is done to take into account that the number of independent measurements being sampled by the rays can be far less than the number of rays, especially close to the center of the bubbles. This procedure is repeated for all the stages of the template subtraction, using the simple disk template for ICS for illustration (our conclusions do not depend on this choice).

The results are shown in Figure 6.7 for the averaged $1-2$ GeV and $2-5$ GeV maps, and the averaged $5-10$ GeV and $10-20$ GeV maps. In both energy ranges the edges are clearly visible; in the south, this is true even before any templates are subtracted. The intensity profile of the north bubble is strikingly similar to profile of the south bubble. For both of the north and south bubbles, no significant edge-brightening or limb-brightening of the bubbles is apparent from the profiles, the flux is fairly uniform inside the bubbles.

In Figure 6.8, we plot the intensity profile as a function of latitude from the south to the north pole. We construct great circle arcs perpendicular to the $l = 0$ great circle, extending 10° in each direction (east and west), and average the emission over each such arc. The flatness of the bubbles with latitude (except possibly close

to the Galactic plane), and the sharp edges at high latitude, are also apparent here.

6.4 Construction of Energy Spectrum of *Fermi* Bubble

We've shown that the *Fermi* bubble has a harder spectrum than other large scale diffuse structures, which is one of the key identifying features of the bubbles. In this section, we attempt to estimate the energy spectrum of the gamma rays associated with the bubbles quantitatively. In order to measure the hardness of the spectrum of the *Fermi* bubbles we carefully compute a template regression with Poisson logarithmical likelihood for different selections of gamma-ray templates for each gamma-ray emission mechanism, fitting in 10 logarithmically-spaced energy bands from 300 MeV to 300 GeV. First, we maximize the Poisson likelihood of a diffuse emission model involving 5-templates. In this model, we include the SFD dust map as a tracer of π^0 emission which is dominant (or nearly so) at most energies on the disk and significant even at high latitudes, the simple disk model, the bubble template, the *Loop I* template, and a uniform background as templates to weight the *Fermi* data properly. Systematic uncertainties are driven by the imperfect knowledge of the diffuse emission model where we used morphological templates.

For each set of model parameters, we compute the Poisson log likelihood,

$$\ln \mathcal{L} = \sum_i k_i \ln \mu_i - \mu_i - \ln(k_i!), \tag{6.1}$$

where μ_i is the synthetic map (i.e., linear combination of templates) at pixel i, and k is the map of observed data. The last term is a function of only the observed maps.

The 1σ Gaussian error is calculated from the likelihood by $\Delta \ln \mathcal{L} = 1/2$. The error bars are simply the square root of the diagonals of the covariance matrix. We refer to Appendix B of Dobler et al. (2010) for more details of the likelihood analysis. Maps of the models constructed from linear combinations of these five templates, and the residual maps between the *Fermi* data and the combined templates at different energy bins, are shown in Figure 6.9. In this fit, we mask out all pixels with Galactic latitude $|b| < 20^\circ$ (the dashed black line in the residual maps). The *left* column shows the linear combination of the disk, *Loop I*, uniform, and bubble templates that provide the best fit to the *Fermi* maps after subtracting the best fit SFD dust template (shown in the *middle* column). The difference maps between the combined template and the data are shown in the *right* column. The template fitting is done for the region with $|b| > 20^\circ$ to avoid contaminations from the Galactic disk (shown with black dashed line in the *right* column residual maps). The subtraction of the model largely removes the features seen in the *Fermi* maps with $|b| > 20^\circ$. We use the same gray scale for all the panels. We find that both the disk IC template and *Loop I* features fade off with increasing energy, but the bubble template is required for all the energy bands and does not fade off with increasing energy. The oversubtraction in the residual maps, especially at lower energy bins, is due to the simple disk IC model, which is not a good template across the entire disk. However, outside the masked region, the residual maps are consistent with Poisson noise without obvious large scale features.

Template-correlated spectra for the 5-template fit are shown in Figure 6.10. The fitting is done with regions of $|b| > 20^\circ$. For a template that has units (e.g., the SFD dust map is in E_{B-V} magnitudes) the correlation spectrum has obscure units (e.g.

gamma-ray emission per magnitude). In such a case we multiply the correlation spectrum by the average SFD value in the bubble region, masking out the $|b| < 20^\circ$ region Su et al. (2010). For the uniform, *Loop I*, and bubble templates (including inner, outer, north, and south), no renormalization is done. These templates are simply ones and zeros (smoothed to the appropriate PSF), so the outer bubble spectrum is simply the spectrum of the bubble shell template (Su et al. 2010), *not* the mean of this template over the whole bubble region.

In Figure 6.10, we employ a simple disk model for the IC (and to a lesser degree bremsstrahlung) emission from supernova-shock-accelerated electrons (see Chapter 6.4). The SFD-correlated spectrum is shown by the red short-dashed line which roughly traces π^0 emission (the gray dashed line indicates a `GALPROP` prediction for π^0 emission). Vertical bars show statistical errors of the 68% confidence range. The disk-correlated emission is shown by the green dashed line, which traces the soft IC (gray triple-dot-dashed line) and bremsstrahlung (gray dot-dashed line) component. The spectrum of the uniform emission, which traces the isotropic background (including possible cosmic-ray contamination), is shown as a dotted brown line. The solid orange line indicates the spectrum of emission correlated with *Loop I*, which has a similar spectrum to the disk-correlated emission. Finally, the blue dot-dashed line shows the spectrum correlated with the *Fermi* bubble template. The bubble component has a notably harder (consistent with flat) spectrum than the other template-correlated spectra, and the models for the various emission mechanism generated from `GALPROP`, indicating that the *Fermi* bubbles constitute a distinct component with a hard spectrum. The fitting is done over the $|b| > 20^\circ$ region. Note that these `GALPROP` "predictions" are intended only to indicate the expected spectral

shape for these emission components, for reference. The correlation coefficients for the SFD map and simple disk model are multiplied by the average value of these maps in the bubble region, with a $|b| > 20^\circ$ cut) to obtain the associated gamma-ray emission; see Chapter 6.4 for details. In Figure 6.10, we also show spectra for π^0 emission, bremsstrahlung and inverse Compton scattering calculated using a sample `GALPROP` model (tuned to match locally measured protons and anti-protons as well as locally measured electrons at $\sim 20 - 30$ GeV), as an indication of the expected spectral shapes. The spectra for the SFD and the simple disk template reasonably match the model expectations. The dust map mostly traces the π^0 emission, and the simple disk model resembles a combination of IC and bremsstrahlung emission. The spectrum for emission correlated with the *Fermi* bubbles is clearly significantly harder than either of these components, consistent with a *flat* spectrum in E^2dN/dE. This fact coupled with the distinct spatial morphology of the *Fermi* bubbles indicates that the IC bubbles are generated by a *separate* electron component. We also note that the spectrum of the bubble template falls off significantly at energy $\lesssim$1 GeV. This feature is robust with respect to the choice of templates.

The hardness of this spectrum is one of the key/mystery to deciphering the nature/origin of the *Fermi* bubbles. In Su et al. (2010), we identify that at lower energy ($E \lesssim 1\,\mathrm{GeV}$) the bubble spectrum falls sharply (becomes dramatically harder than -2). With reduced statistical error from three year Fermi-LAT data and aforementioned improved analysis tools with less expected systematic error, we confirm the significant falling of the spectrum at lower energy. With the recently improved event selection algorithms released by *Fermi* and the increased count rates, we are able to use only the front-converting events with better angular resolution,

which is important at lower energy ($\lesssim$ few GeV). Again, we confirm the fall-off of the energy spectrum of the bubbles at $E \lesssim 1\,\mathrm{GeV}$.

To demonstrate the robustness of the spectrum we have derived for the *Fermi* bubbles, we make use of the *Fermi* $0.5 - 1$ GeV residual map (after subtracting the SFD dust map to largely remove the π^0 gammas) as a template of IC emission, and perform a 4-template fit (Chapter 6.2.3). These gamma rays mostly originate from IC scattering of a relatively soft population of electrons in the disk (originating primarily from scatterings on *starlight*, and likely involving softer supernova-shock-accelerated electrons), but might also contain gammas from IC scattering on *starlight* by a latitudinally extended electron population. We use the SFD dust map as a template for π^0 gammas as previously, and include the uniform background and the bubble template as in the previous 5-template fit. The fitting is done with regions of $|b| > 20^\circ$. For the SFD dust map and the *Fermi* $0.5 - 1$ GeV IC template (afer removing the π^0 gammas for a better template for low-latitude IC emission). The residuals are remarkably small, the correlation coefficients are weighted by the mean of each template in the "bubble" region. The resulting model and the difference maps with respect to the *Fermi* data, at different energy bands, are shown in Figure 6.11. The spectrum is shown in Figure 6.12. The *Fermi* $0.5 - 1$ GeV IC template appears to contain a small fraction of π^0 gammas, but the spectral index is consistent with the predicted `GALPROP` IC component.

In the last study, significant isotropic background is due to extra-galactic emission and misclassified charged particle contamination, including heavy nuclei at high energies. Such misclassification varies among different event classes and convertion types (front or back). The *Fermi* collaboration has measured the

extragalactic diffuse emission using additional cuts to reduce charged particle contamination (Abdo et al. 2010): below $\sim$ 20 GeV the isotropic contribution in our fits is roughly a factor of 2 larger than the extragalactic diffuse emission, but has a similar spectral slope. At energies above $\sim$ 20 GeV the isotropic contribution becomes much harder, which we attribute to charged particle contamination.

The *Fermi* bubbles appear to possess north-south symmetry in morphology without noticable difference in intensity (both with a sharp cutoff at the bubble edges). To verify if there are any spectral variations in the gamma-ray emission associated with the two bubbles which we are modeling as a whole in the 5-template fitting, we divided the previous *Fermi* bubble template into the *north* and *south bubble* templates. We then repeat the previous 5-template and 4-template fitting procedure involving either the simple disk IC template or the *Fermi* $0.5 - 1$ GeV IC template, but splitting the bubble template to *north and south bubble* templates, and allowed an independent normalization of the two bubble templates. The goal is to identify variations in the intensity and spectral index between the northern and southern bubbles. The resulting fitted spectra are shown in Figure 6.13, no significant spectral differences are found between the north and south bubble. In the *top row*, we use the simple disk model as the IC template. In the *left* panel, we split the previous bubble template into *bubble interior* and *bubble shell* templates. The correlation coefficients of the 6-template fit involving the two bubble templates are shown. The purple dash-dotted line and blue triple-dot-dashed line are for the inner bubble and the outer shell template respectively. The two templates have a consistent spectrum which is significantly harder than the other templates, indicating the *bubble interior* and the *bubble shell* have the same distinct physical

origin. In the *right* panel, we split the bubble template into *north* and *south* bubbles. As we include the *Loop I* template (which has a softer spectrum) in the north sky for regression fitting, the north bubble has a slightly harder spectrum than the south bubble. Again, both of the templates have harder spectra than any other components in the fit. In the *Bottom row*, we employ the *Fermi* $0.5-1$ GeV residual map (after subtracting the SFD dust) as a template for the *starlight* IC. In the *left* panel, we split the bubble template into *bubble interior* and *bubble shell* templates. In the *right* panel, we split the bubble template into *north bubble* and *south bubble* templates. As in Figure 6.10, the correlation spectra have been normalized to a reference region; see Chapter 6.4 for details. There was no significant improvement of the likelihood for such spliting. Our conclusion is that the *Fermi* bubbles appear to be north-south symmetric, with both a hard spectrum. This statement is largely independent of our choice of template for the disk IC emission. In summary, we found no apparent difference between the north and the south *Fermi* bubble both in morphology and in energy spectrum, which indicates they share the same origin.

Given a power law steady-state electron spectrum with spectral index γ, the spectral index of the IC scattered gamma rays is $(\gamma+1)/2$ in the Thomson limit, and $\gamma+1$ in the extreme KN limit (e.g. Blumenthal & Gould 1970). Photons in the *Fermi* energy range can be produced by scattering of $\mathcal{O}(10-100)$ GeV electrons on starlight, which is (marginally) in the KN regime, or by Thomson scattering of much higher-energy electrons on IR or CMB photons. Consequently, the spectral index of gamma rays might be expected to vary with latitude even if the electron spectral index is uniform, becoming harder at higher latitudes where scatterings in the Thomson limit dominate. Closer to the disk, where much of the ISRF energy

density is in starlight, IC scatterings are in neither the extreme KN nor Thomson limits, and the spectrum needs to be computed carefully.

6.5 Discussions

Our analysis in the discovery paper of the *Fermi* bubbles (Su et al. 2010) was adequate to convincingly reveal two large bubble structures towards the inner galaxy. In this chapter, we have confirmed these structures at $1 \lesssim E \lesssim 100\,\mathrm{GeV}$ in *Fermi* gamma-ray maps including first three year observations and improved data analysis pipeline. The bubbles extend to $\sim 50^\circ$ above and below the Galactic center, with a maximum width of $\sim 40^\circ$ in longitude. From this update analysis, we confirm that the two bubbles have well defined spacial morphology with sharp edges, neither limb brightened nor centrally brightened, and are nearly symmetric about the Galactic plane with respect to the Galactic center. We note that at $|b| \lesssim 20^\circ$, these "*Fermi* bubbles" have a spatial morphology similar to the *WMAP* microwave haze (Finkbeiner 2004a; Dobler & Finkbeiner 2008). And the *ROSAT* X-ray map also reveal limb brightened X-ray features with hard energy spectrum that align with the edges of both the north and south *Fermi* bubble (Su et al. 2010). The appearance of the X-ray edges in *ROSAT* strongly supports the physical reality of these sharp edges. The similarities of the morphology and hard spectrum strongly suggest that the *WMAP* haze and the *Fermi* bubbles share a common origin. The "*WMAP* haze" and *Fermi* bubbles are consistent with being produced from the same electron CR population (by synchrotron and IC respectively) (Su et al. 2010).

To better reveal the bubble structures, we use spatial templates to regress

out known emission mechanisms as we did in Su et al. (2010). To remove π^0 and bremsstrahlung gammas, we use the SFD dust map, assuming that the interstellar dust traces gammas produced by cosmic ray protons (π^0 decay) and electrons (bremsstrahlung) colliding with the ISM. To trace the gamma rays from IC scattering of disk electrons on the ISRF, we have compared a simple geometric disk model with the $0.5 - 1$ GeV *Fermi* map after removal of the (dust-correlated) π^0 gammas. We verify that our results are insensitive to this choice. Although our template fitting technique is subject to significant uncertainties due to uncertain line of sight gas and CR distributions, these uncertainties mainly affect the intensity profile at low latitudes. For $|b| > 20^\circ$ and $1 < E < 50\,\mathrm{GeV}$ the morphology and spectrum are completely consistent for different template choices. In fact, a significant part of the southern bubble at high latitude with $|b| > 20^\circ$ is easily visible before *any* template subtractions with uniform intensity distribution and sharp edge. We would like to emphasize that the *Fermi* bubble features are not aligned with neither *Loop I* nor *North Polar Spur* features found in low frequency radio maps (Casandjian et al. 2009). *Loop I* and other shell-like structures indeed appear in the gamma rays with softer energy spectrum compared with that of the bubble's.

We confirm that the *Fermi* bubbles have an energy spectrum of $dN/dE \sim E^{-2}$, significantly harder than other gamma-ray components. There is no apparent spectral variation neither along the galactic latitude nor between the bubble edge and the interior. And the north and south bubbles have consistent spatial and spectral profiles too. Both the morphology and spectrum are consistent with the two bubbles having the same origin and being the IC counterpart to the electrons which generate the microwave haze seen in *WMAP* (Finkbeiner 2004a; Dobler &

Finkbeiner 2008). The spectrum of the CR electrons required to generate the *Fermi* bubbles is harder than expected for electrons accelerated in supernova shocks in the disk, and such disk-produced electrons would be even softer after several kpc diffusion; the morphology of the bubble structure is also quite different to that of the lower-energy electrons traced by the Haslam 408 MHz map. Even setting aside the *WMAP* haze, the *Fermi* bubbles are unlikely to originate from excess π^0 emission, as (by construction) they are spatially distinct from the SFD dust map, their spectrum is much harder than that of the dust-correlated emission, and the *ROSAT* data suggest that the bubbles are hot and underdense rather than overdense. The morphology of the *Fermi* bubbles, and the overlap of the *Fermi* bubbles and *WMAP* haze, also strongly *disfavor* the hypothesis that a significant fraction of the high energy gamma rays observed by *Fermi* in the bubble region are photons directly produced by dark matter annihilation.

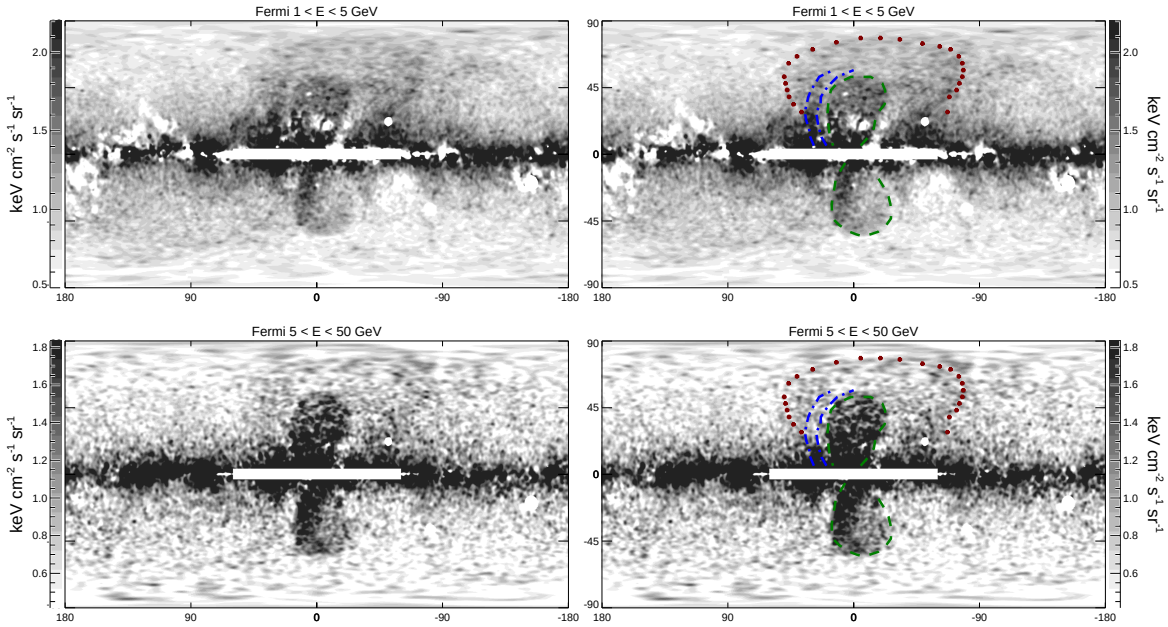

Figure 6.4.— Full sky residual maps after subtracting the SFD dust and disk templates from the *Fermi*-LAT three year gamma-ray maps in two energy bins. Point sources are subtracted, and large sources, including the inner disk ($-2^\circ < b < 2^\circ, -60^\circ < \ell < 60^\circ$), have been masked. Two large bubbles are seen (spanning $-50^\circ < b < 50^\circ$) in both cases. *Right panels:* Apparent *Fermi* bubble features marked in color lines, overplotted on the maps displayed in the *left panels*. Green dashed circles above and below the Galactic plane indicate the approximate edges of the north and south *Fermi* bubbles respectively. Two blue dashed arcs mark the inner (dimmer) and outer (brighter) edges of the *northern arc* – a feature in the northern sky outside the north bubble. The red dotted line approximately marks the edge of *Loop I*.

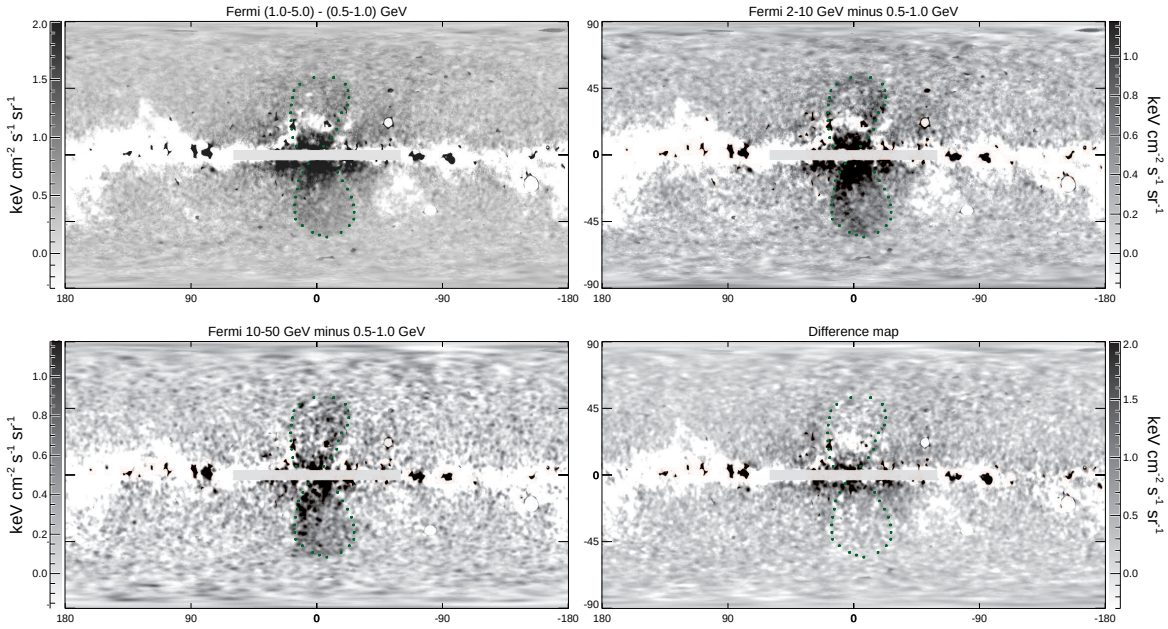

Figure 6.5.— *Top left:* Full sky *Fermi*-LAT three year $0.5-1.0$ GeV map subtracts the SFD dust map as a template of π^0 gammas. *Top right:* The same as *top left* panel, but for energy range $2-50$ GeV (note the different gray scale for the two panels). *Bottom left:* The $2-10$ GeV *Fermi* gamma-ray map subtracting the *top left* $0.5-1.0$ GeV residual map which is used as a template of ICS of *starlight*. The *Fermi* bubble structures are better revealed after subtracting the lower energy $0.5-1.0$ GeV residual map with extended disk-like emission. *Bottom right:* The difference between the the *upper* two panels. The bubble structure is largely removed in this difference map.

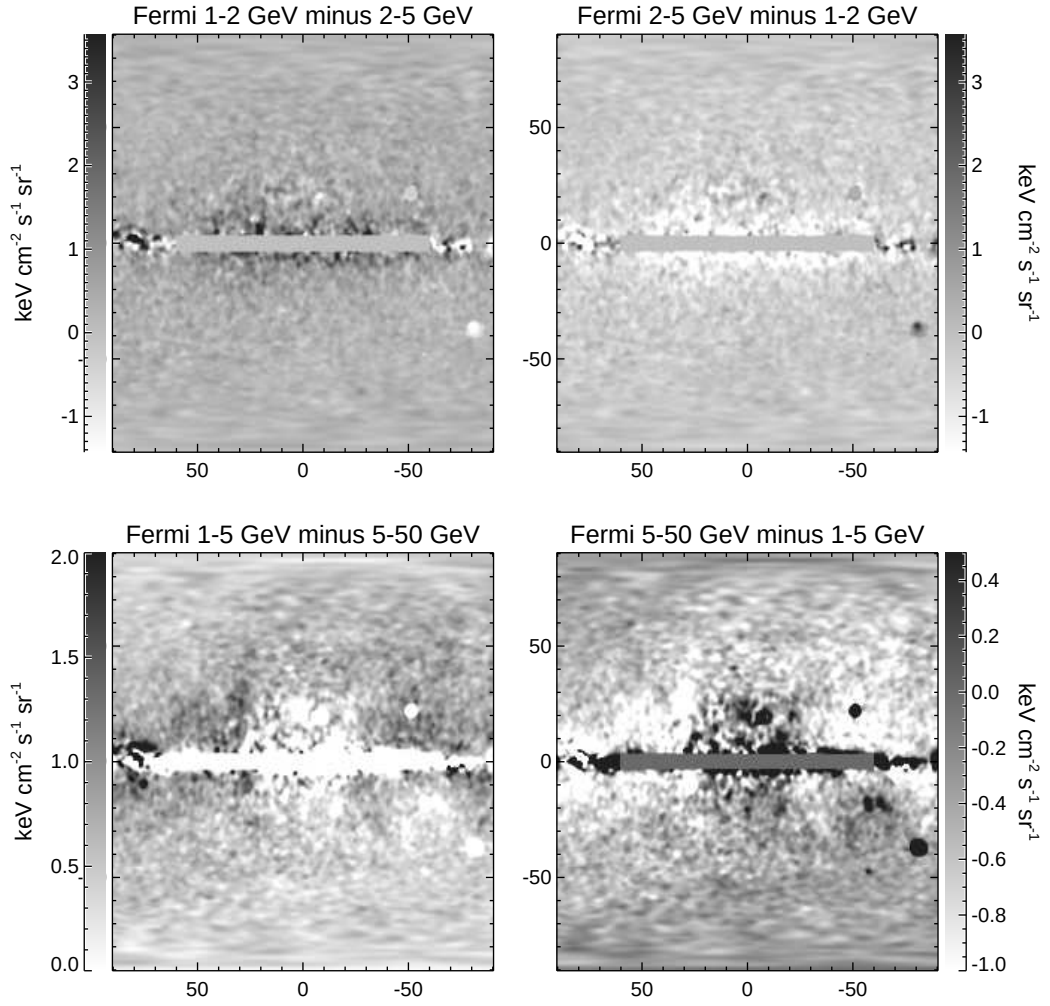

Figure 6.6.— Comparison of the *Fermi* bubbles between different energy bins revealed from the three year *Fermi*-LAT observations. *Top left:* Subtraction of the $2-5$ GeV residual map from the $1-2$ GeV residual map; each residual map is constructed from the data by regressing out the SFD dust and disk templates to best reveal the *Fermi* bubbles. The difference map is consistent with Poisson noise away from the masked region, and the bubble features can hardly be recognized, indicating that different spatial regions of the *Fermi* bubbles have the same spectrum. *Top right:* The same map as *left* panel, but with $1-2$ GeV map subtracted from $2-5$ GeV map. *Bottom row:* Same as the *upper panels*, but subtracting the $5-50$ $(1-5)$ GeV residual map from the $1-5$ $(5-50)$ GeV residual map.

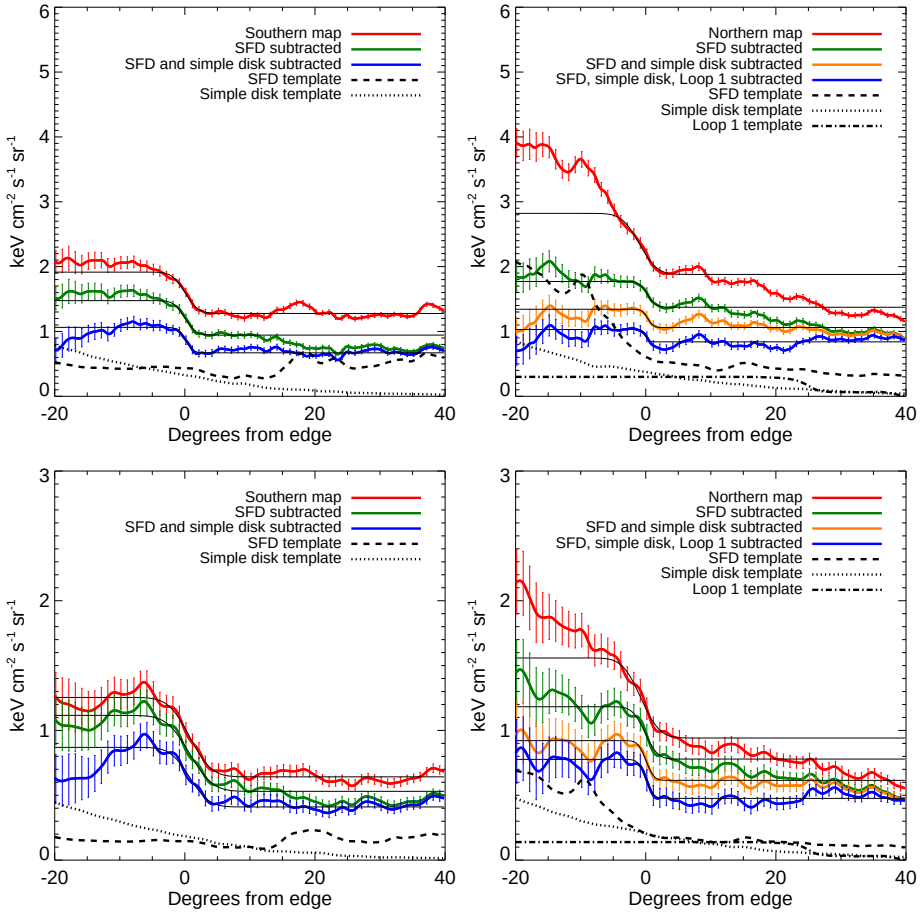

Figure 6.7.— Intensity as a function of radial distance from the bubble edge (radial profile) in different energy range, averaged over great circle arcs intersecting the bubble center and lying at $|b| > 28°$ (technical details are described in Chapter 2.2.2. Results are shown for (*left*) the southern bubble, and (*right*) the northern bubble, for (*top*) the averaged $1-2$ and $2-5$ GeV maps, and (*bottom*) the averaged $5-10$ and $10-20$ GeV maps. The origin is the edge of the bubbles. Different lines show the results after subtracting different emission templates and the corresponding errors are plotted (see text for an outline of the error analysis).

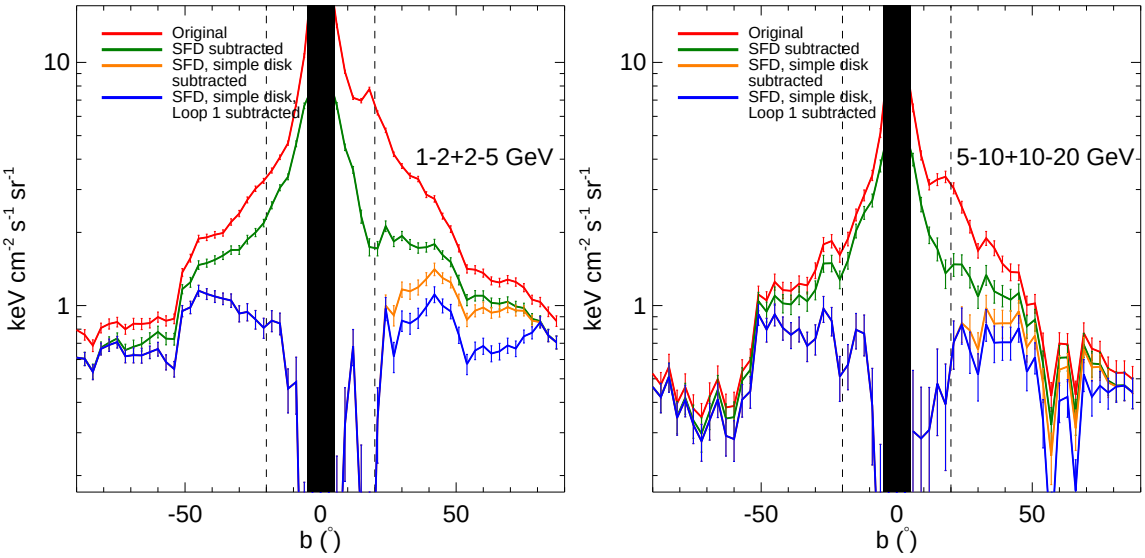

Figure 6.8.— Gamma-ray intensity profile averaged over the central 30 degrees in longitude, as a function of latitude, for (*left*) the averaged $1-2$ and $2-5$ GeV maps, and (*right*) the averaged 5-10 and 10-20 GeV maps. We construct great circle arcs perpendicular to the $l = 0$ great circle, extending 10° in each direction (east and west), and average the emission over each such arc; the "b" label corresponding to each arc, and the x-axis of the plot, refers to the value of b at $l = 0$. Different lines show the results at different stages of the template subtraction process. The large oversubtraction at $b \sim 15°$ in the north, especially pronounced in the low-energy data, is associated with a bright feature in the SFD dust map.

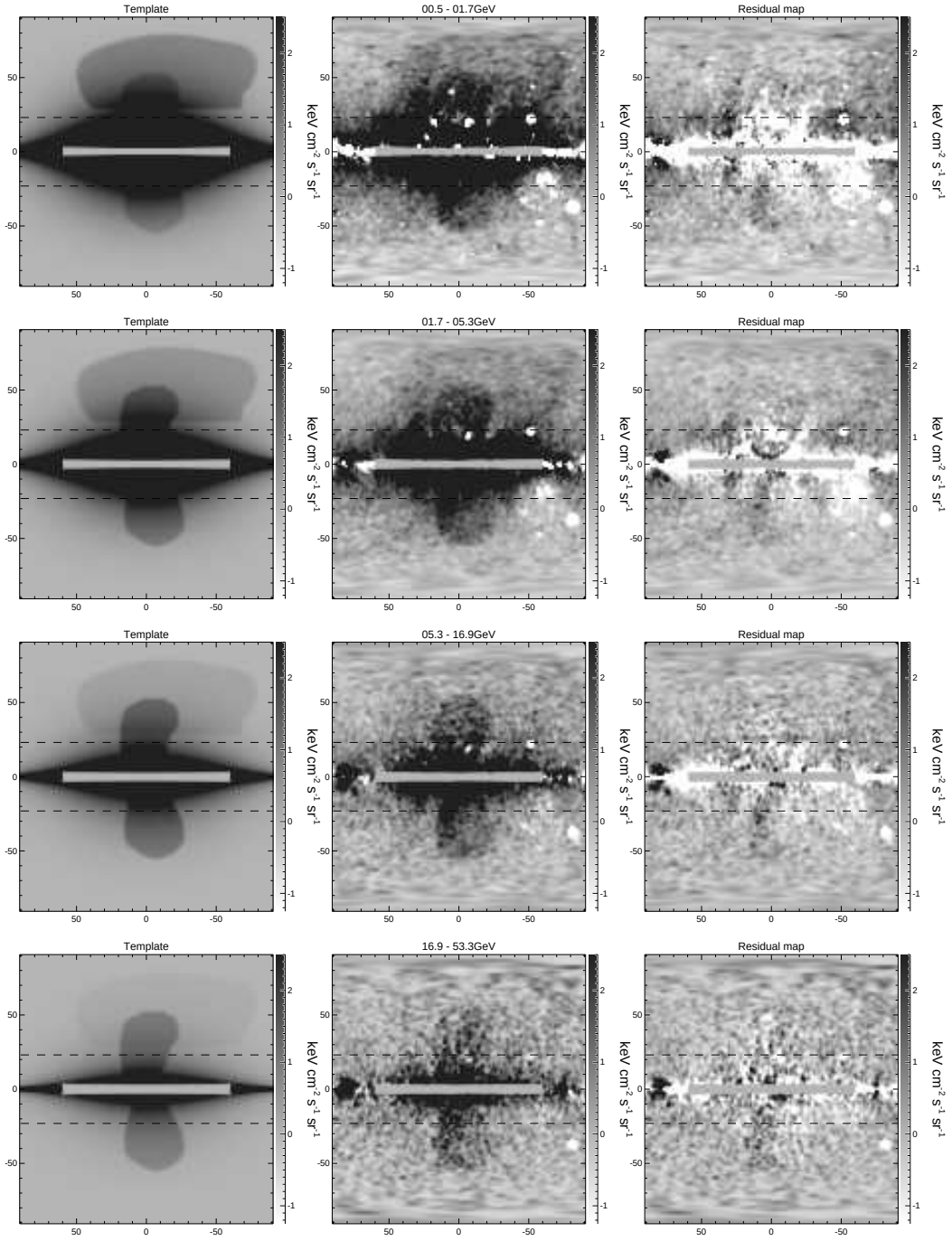

Figure 6.9.— The models obtained from the multi-template fits, compared with the *Fermi* maps, in different energy bins.

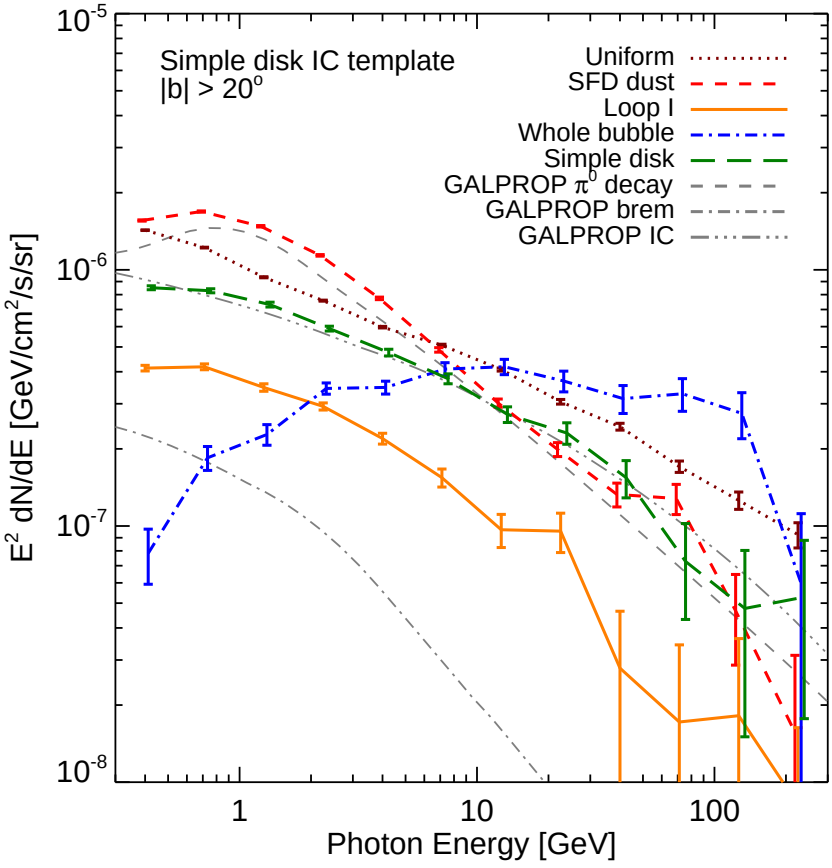

Figure 6.10.— Spectral energy distribution of the gamma-ray emission of different emission templates from the 5-template fit.

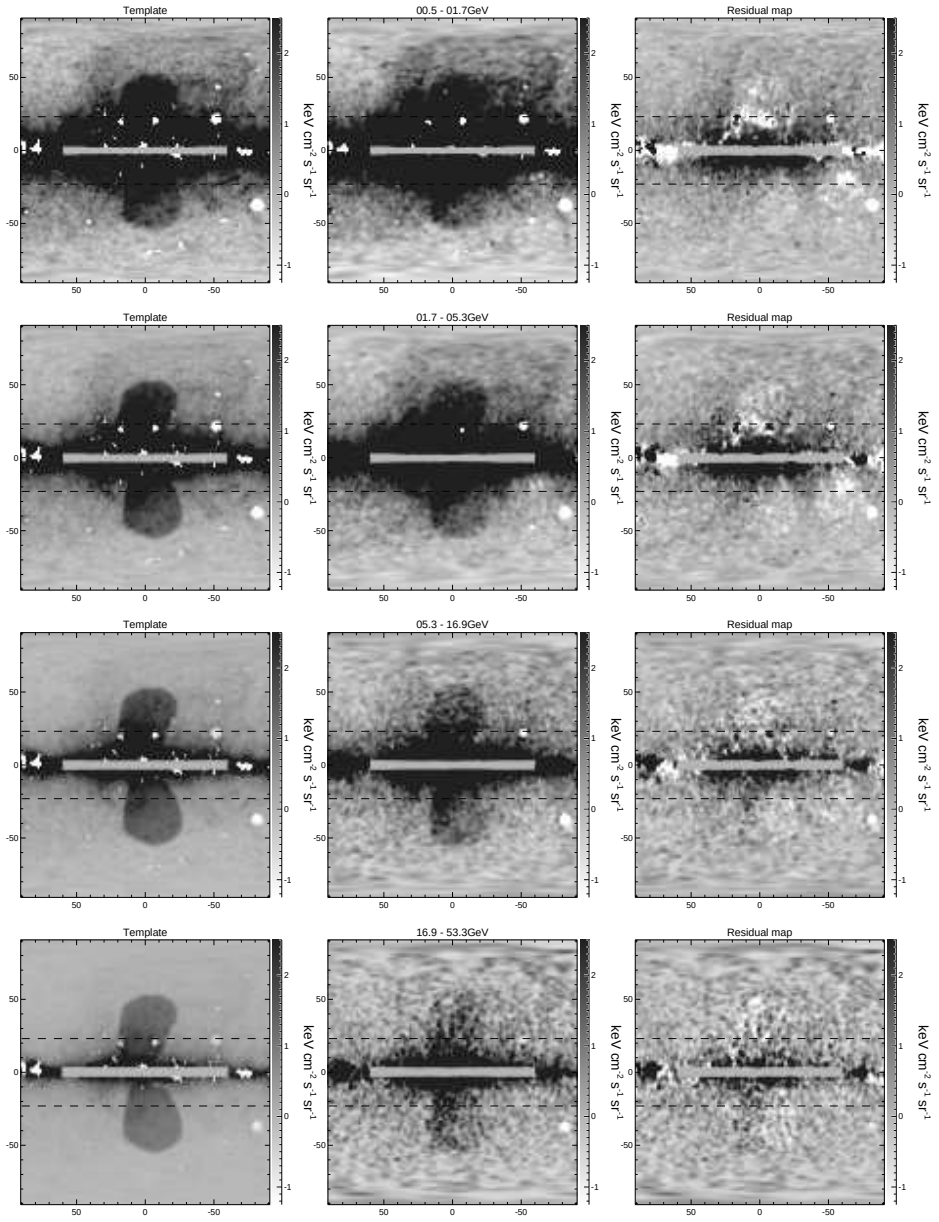

Figure 6.11.— The same as Figure 6.9, but using the *Fermi* $0.5-1$ GeV residual map after subtracting emission correlated with the SFD dust map.

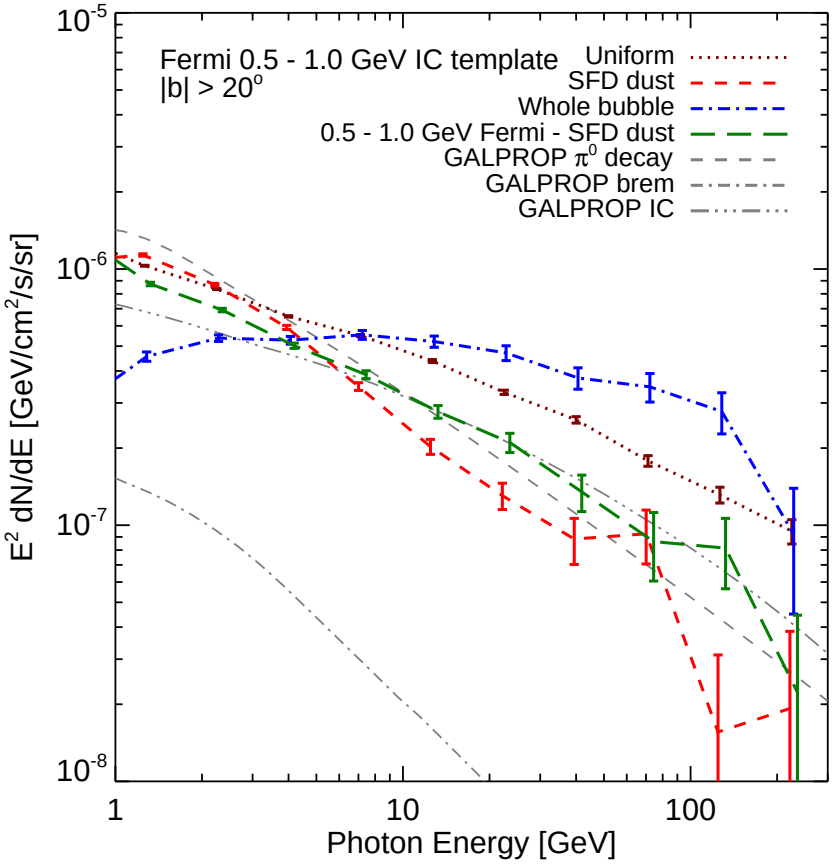

Figure 6.12.— Same as Figure 6.10, but correlation spectra for the 4-template fit employing the *Fermi* $0.5 - 1$ GeV residual map (after subtracting the SFD dust) as a template for the *starlight* IC. The line style is the same as Figure 6.10. Again, we find that the spectrum correlated with the *Fermi* bubble template (blue dot-dashed line) is harder (consistent with flat in E^2dN/dE) than the spectra correlated with the other templates, and the models for the various emission mechanism generated from `GALPROP`, indicating that the *Fermi* bubbles constitute a distinct gamma-ray component with a hard spectrum. The fitting is done for $|b| > 20°$. As in Figure 6.10, the correlation spectra have been normalized to a reference region; see Chapter 6.4 for details.

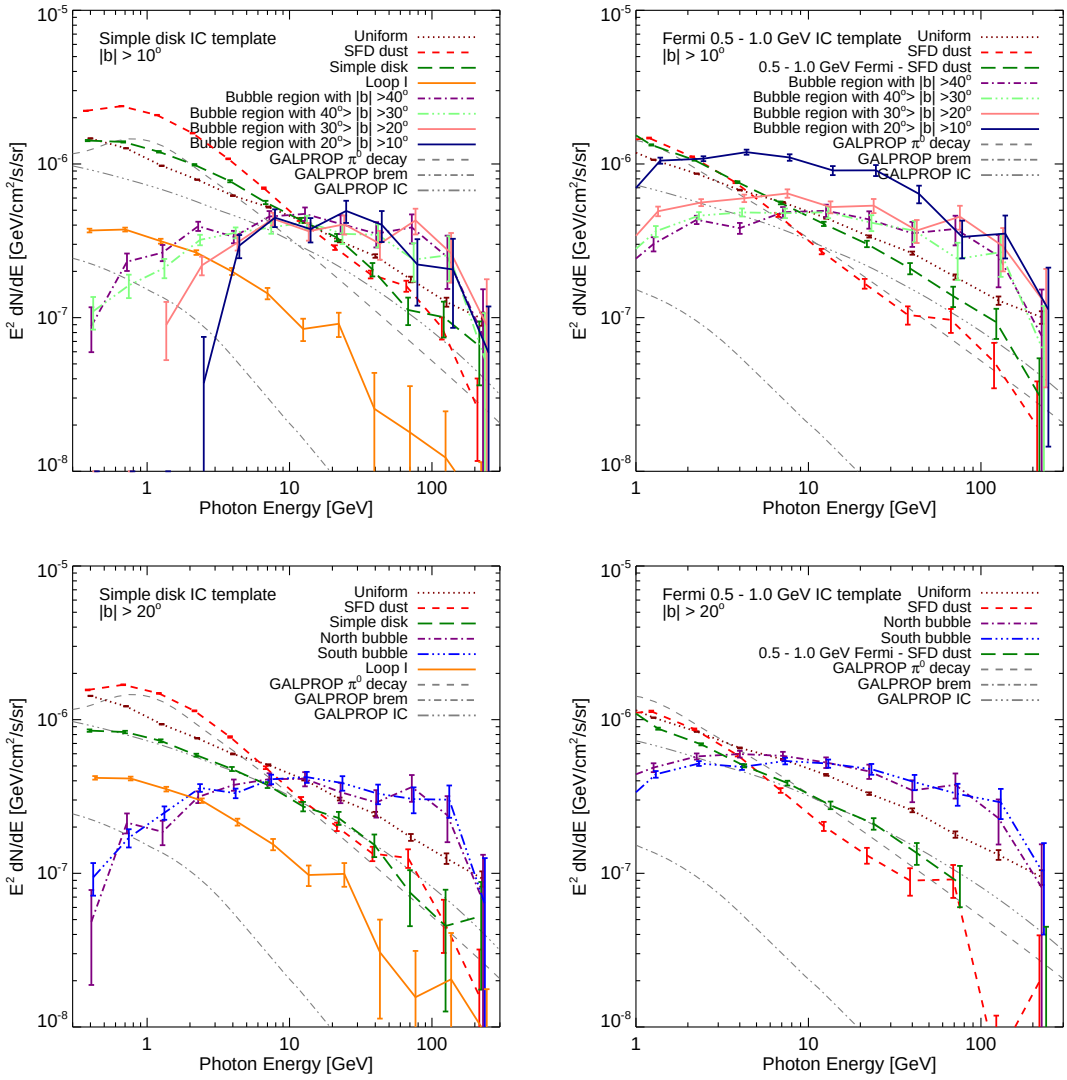

Figure 6.13.— Same as Figure 6.10 and Figure 6.12, but splitting the *Fermi* bubble template into two components for template fitting. The line styles are the same as Figure 6.10.

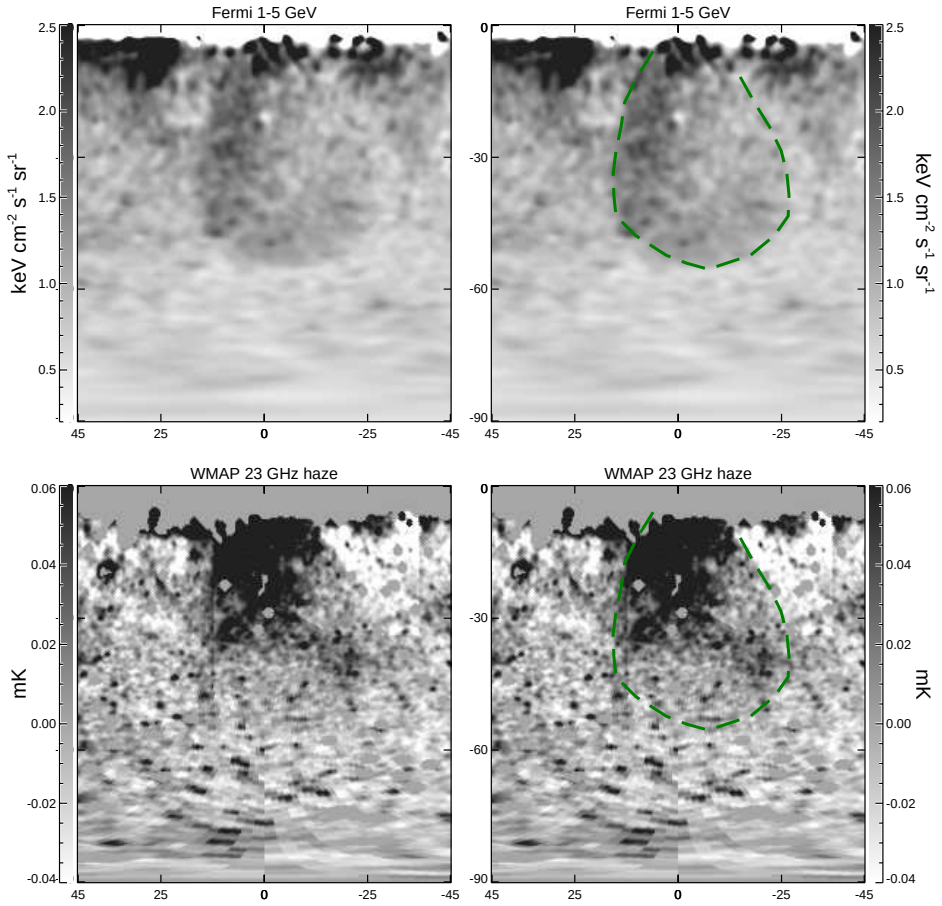

Figure 6.14.— The *Fermi* bubbles at $1-5$ GeV (the residual map obtained by subtracting the SFD dust map and the disk template) compared with the *WMAP* K-band (23 GHz) haze (Dobler & Finkbeiner 2008). *Top row:* The $1-5$ GeV map with $\ell = [-45°, 45°]$ and $b = [-90°, 0°]$ (*left* panel) with the *Fermi* south bubble edge overplotted in green dashed line (*right* panel). *Bottom row:* Same sky region as *top row* but displaying the *WMAP* haze at 23 GHz (*left* panel), with the *Fermi* south bubble edge overplotted in green dashed line (*right* panel).

Chapter 7

Conclusions and Future Directions

This thesis describes the recent discovery of two giant gamma-ray emitting bubbles with ∼10 kpc each appearing above and below the Galactic center, named "*Fermi* bubbles". This surprising structure was first revealed with 1.6 year data from Large Area Telescope aboard on *Fermi Gamma-ray Space Telescope* (Su et al. 2010). And with three years of LAT observations currently available, we have studied the *Fermi* bubble structure in further detail. Particularly, We have found evidence of a gamma-ray cocoon feature within the southern bubble, with a jet-like feature along the cocoon's axis of symmetry, and another directly opposite the Galactic center in the north.

The Morphology: The two gigantic gamma-ray emitting bubbles extend up to ∼50 degrees towards the inner Galaxy, symmetric about the Galactic plane, with a width of ∼40 degrees in longitude. The morphology of the bubbles shows sharp edges suggesting their transient nature. The gamma-ray morphology is neither limb

brightened nor centrally brightened. At $|b| \lesssim 30°$, these "*Fermi* bubbles" have a spatial morphology similar to the *WMAP* microwave haze (Finkbeiner 2004a; Dobler & Finkbeiner 2008). The *ROSAT* soft X-ray 1.5 keV map also reveals hard-spectrum features that align well with the edges of the *Fermi* bubbles. In contrast, the *Fermi* bubble features are not aligned with *Loop I* or any other feature in the Haslam 408 MHz map; while *Loop I* and other shell structures appear in the gamma rays, their spectra are softer than the bubble spectrum. Furthermore, there are no convincing features spatially correlated with the bubbles in the LAB H I or Hα maps.

The sharp edge of the bubbles might suggest the presence of a shock at the bubble walls. If the CRs producing the gamma rays have a multi-kpc diffusion length (which is not expected to be the case for 1 TeV electrons, for example), then the edges can still be sharp if the bubble edge is moving outward faster than they can diffuse. If we assume that the *Fermi* bubbles are projected structures from three dimensional symmetric blobs towards the GC, the intensity profile of the bubbles requires the emissivity to rise at the bubble walls, but remain non-negligible in the bubble interior. The morphology of the bubble structure is also quite different from that of the lower-energy electrons traced by the Haslam 408 MHz map. Even setting aside the *WMAP* haze, the *Fermi* bubbles are unlikely to originate from excess π^0 emission, as (by construction) they are spatially distinct from the SFD dust map, their spectrum is much harder than that of the dust-correlated emission, and the *ROSAT* data suggest that the bubbles are hot and underdense rather than overdense.

The Spectrum: The gamma-ray emission from the bubbles has an energy spectrum of $dN/dE \sim E^{-2}$, significantly harder than other diffuse gamma-ray

components from hundreds of MeV to ∼100 GeV, implying the ability of the *Fermi* bubbles to accelerate CR electrons up to ∼TeV, if the gamma rays are produced by inverse Compton scattering of the cosmic microwave background photons (Su et al. 2010). There is no obvious softing of the gamma-ray spectrum of the *Fermi* bubbles from the inner part to ∼50 degree away from the GC, suggesting either *in situ* particle acceleration or fast CR transportation from the inner galaxy, if the CRs were produced close to the GC. The cooling time for ∼TeV electrons is only $\sim 10^5$ years. If the CRs producing the *Fermi* bubbles are produced in the inner Galaxy, in order to transport the CRs ∼10 kpc away from the GC, the CR diffusion or the velocity of Galactic outflows (starburst or AGN origin) which entrain the CRs, depending on the transportation mechanism, must be relativistic (Su et al. 2010). The spectrum of the CR electrons required to generate the *Fermi* bubbles is harder than expected for electrons accelerated in supernova shocks in the disk, and such disk-produced electrons would be even softer after several kpc diffusion. There is no apparent spatial variation in the spectrum between the bubble edge and interior, and the north and south bubbles have consistent spatial and spectral profiles.

Implications for Cosmic Rays Producing the Bubbles: The similarities of both the morphology and hard spectrum strongly suggest that the *WMAP* haze and the *Fermi* bubbles share a common origin with the bubbles being the IC counterpart to the microwave haze. The presence of a population of e^- CR with a hard spectrum a few kpc off the plane is intriguing by itself, as energy losses during propagation up from the disk would soften the CR spectrum. Such a spectrum would also produce the observed inverse-Compton scattered gammas of the *Fermi* bubbles . The lack

of spatial variation in the spectral index may constrain models where the electrons diffuse long distances from the acceleration sites. Magnetic reconnection in the interior of the bubbles, or some other mechanism such as dark matter annihilation, may help maintain a hard spectrum throughout the bubbles by accelerating existing lower-energy electrons or injecting electrons *in situ*. However, the morphology of the *Fermi* bubbles strongly *disfavor* the hypothesis that a significant fraction of the high energy gamma rays observed by *Fermi* in the bubble region are photons directly produced by dark matter annihilation. The discovery of this large gamma-ray $(1-100$ GeV) bubble structures in the Milky Way opens a new window on large-scale injection of energy in the inner Galaxy.

AGN Jet as the Origin: We suggest that the *Fermi* bubble structures were likely created by some episode of intensive energy injection towards the GC, such as a past accretion event onto the central supermassive black hole, or a nuclear starburst in the last $\sim$10 Myr. We have discussed some models and related topics in this thesis, and found shortcomings in each scenario; it seems likely that either significant modifications to one of these ideas, or some combination of different mechanisms, will be necessary. A comprehensive survey of models to explain the *Fermi* bubbles and different scenarios of CR acceleration has been discussed in Su et al. (2010).

In the former case, accretion may produce an energetic large scale jet which can accelerate CRs to high energy and distribute CRs rapidly to scales comparable or even larger than the bubble size. The cooling time of electrons at $100-1000$ GeV is only 10^{5-6} years, so if the CRs are injected and accelerated only in the GC, a very fast bulk transport mechanism is required to convey them throughout the bubbles

before they lose a significant fraction of their energy. However, filling the bubbles completely, with $n \sim 10^{-3}$ cm^{-3} gas, would require a mass injection of $\sim 10^7$ solar masses, so in any case it is more reasonable for the bulk of the material in the bubbles to be swept up and accelerated as the bubbles expand. Energetic shocks associated with jets can have high Mach number and thus efficiently accelerate CR electrons, producing hard spectra with $dN/dE \sim E^{-2}$, and the total energy required to heat the bubbles is also readily achievable by accretion events onto the central supermassive black hole.

However, the north-south symmetry of the bubbles has no obvious explanation in the context of an AGN jet: there is no reason for the jet to be oriented perpendicular to the Galactic plane. The large width and rounded shape of the bubbles are also not typical of jets, which are generally much more collimated, although a precessing jet might help explain the wide opening angle of the bubbles. If the central supermassive black hole becomes active on a relatively short timescale $\ll$ Myr, the *Fermi* bubbles may be created by a number of past jets, which combine to give rise to the symmetric and uniform *Fermi* bubbles.

AGN/Starburst Wind as the origin: An alternate source for the large required energy injection is a nuclear starburst. The wide opening angle of the bubbles is not a problem if there are Galactic outflows associated with the nuclear starburst. Bow shaped outflow structure similar to the bubbles has been observed in nearby starburst galaxies e.g. NGC 253 (Acero et al. 2009) and NGC 3079 (Cecil et al. 2001), and the X-ray features observed by *ROSAT* are similar to those observed in these starburst galaxies with X-rays. However, no corresponding Hα signal of

the *Fermi* bubbles is observed, in contrast to other known starburst galaxies: this problem might potentially be resolved if the Hα-emitting gas has cooled in the time since the starburst phase (gas hot enough to emit the X-rays observed by *ROSAT* has a considerably longer cooling time, see Su et al. 2010). Also, generally gas filaments and clumps are observed in the X-rays in starburst galaxies, and it would seem that a relic of a past starburst should become more clumpy with gas clouds and filaments due to cooling of the gas. However, while no such structures are obvious in the *ROSAT* maps, the signal-to-noise is insufficient to place strong constraints.

The absence of any such filamentary structures inside the *Fermi* bubbles, on the other hand, argues against a hadronic origin for the bubble gamma ray emission. Hadronic jets might accelerate protons to high energies, and the interactions of these protons with the ISM could then produce hard π^0 gammas and secondary e^+e^-, which would scatter on the ISRF to produce more gamma rays. In this scenario, however, the gamma ray emission should trace the gas density, which we would not expect to be smooth and homogeneous.

The key problem for a starburst scenario is that the possible shocks at the edge of the bipolar Galactic wind are expected to be relatively weak and slow-moving, and thus may not be capable of generating a sufficiently hard electron spectrum to reproduce the observed *Fermi* bubbles by shock accelerations (Su et al. 2010). For example, in first-order *Fermi* acceleration, a shock Mach number of ~ 3.3 is needed to obtain an electron spectral index of 2.4, as required for the synchrotron explanation of the *WMAP* haze (see e.g. Jones & Ellison 1991). As a consequence, the CR electrons must be produced in the GC and transported by the Galactic wind. It's well known that the typical wind speed is less than 1000 kpc/s, the CRs need

more than 10^7 years to reach 10 kpc away from the GC. The cooling problem of the CR electrons is a barrier to explain the bubbles by only starburst.

Dark matter as the origin: Dark matter annihilation or decay, while an effective mechanism for injecting hard electron CRs at high latitudes, cannot *by itself* produce the features in the *ROSAT* X-ray maps correlated with the bubbles, and would not be expected to result in sharp brightness cutoff of the gamma-ray emission at the bubble edges. Large scale astrophysical outflows are required to transport CRs to high latitude and produce the observed morphological features of the *Fermi* bubbles. On the other hand, we cannot rule out the possibility that dark matter annihilation or decay may also provide some high energy CR electrons within the bubbles, or CRs responsible to some fraction of gamma-ray emission towards the inner Galaxy that is not well modeled by either the bubble structure template or the models for known diffuse emission mechanisms. We note that it's not reliable to put constraints on dark matter physics using observed gamma-ray intensity distribution/spectrum towards the Galactic center, as the presence of the *Fermi* bubble implying recent dynamical environment in the inner galaxy. Even if concentrated dark matter distribution produced CRs emitting observable gamma rays, these CRs would be possibly entrained in the Galactic outflow to higher latitude. Detailed knowledge of the *Fermi* bubbles will be a necessary step before extracting any such dark matter signal.

Updates from Literature: The discovery of *Fermi* bubbles has inspired follow up simulations (Guo & Mathews 2011b; Guo et al. 2011a; Zubovas & Nayakshin

2012) and a number of theoretical interpretations of the origin of the bubbles. These interpretations range from AGN activity (Mertsch & Sarkar 2011; Cheng et al. 2011) to starbursts (Zubovas et al. 2011). The nature of the gamma rays from the *Fermi* bubbles has been claimed from π^0 decay (Crocker et al. 2011a; Crocker 2011; Crocker et al. 2011b), and even dark matter (Dobler et al. 2011). The absence of any such filamentary structures inside the *Fermi* bubbles, on the other hand, argues against a hadronic origin for the bubble gamma ray emission. The *Fermi* bubble should not only accelerate CR electrons, but also protons up to much higher energies due to acceleration efficiency and much slower cooling rate of hardrons (Su et al. 2010; Guo et al. 2011b; Chernyshov et al. 2011), and the interactions of these protons with the ISM could then produce hard π^0 gammas and secondary e^+e^-, which would scatter on the ISRF to produce more gamma rays. In this scenario, however, the gamma ray emission should trace the gas density, which we would not expect to be smooth and homogeneous.

One of the ideas of producing episodic energy injection from the Galactic center proposed in Su et al. (2010) is quasi-periodic star capture processes by the Galactic supermassive black hole Sgr A. Cheng et al. (2011) recently calculated in further detail of this model and showed that the star capture induced shocks in the halo can accelerate electrons to $\sim$TeV with a hard spectrum. In Su et al. (2010), we have suggested another idea of producing the past Galactic central activity by a merger of the Galactic supermassive black hole with an globular cluster brought in by the inspiralling satellite. Recently, Lang et al. (2011) further discussed this possibility in detail that the infall of a satellite galaxy into the Milky Way which began at the redshift of 10 and ended few million years ago to produce the observed *Fermi* bubble

structure. Among several possible cosmic ray acceleration mechanisms proposed in Su et al. (2010), Mertsch & Sarkar (2011) further studied the undergoing stochastic 2nd-order Fermi acceleration by plasma wave turbulence through the entire volume of the bubbles. They found that both the hard spectrum and the nearly constant surface brightness can be explained.

Future Study on *Fermi* Bubbles: The *eROSITA*[1] and *Planck*[2] experiments will provide improved measurements of the X-ray and microwave counterparts associated with the *Fermi* bubbles, respectively. Future multi-wavelength information of the *Fermi* bubbles may discriminate different scenarios we proposed in this thesis. *eROSITA*, which is expected to launch in 2013, will provide the first imaging all-sky survey of mid-energy X-rays in the energy range of $0.5 - 10$ keV with ~ 100 eV energy resolution and a PSF of $\sim 30''$. The *Planck* satellite, launched in 2009, will greatly improve the measurements of the *WMAP* haze spectrum, and may identify interesting bubble-related features in polarized microwave maps. In addition, AMS-02[3] launched in early 2011 may significantly advance our understanding of CR acceleration and propagation, and help to refine our interpretation of the *Fermi* bubbles. In the future, ground/space based missions observing high energy electron and gamma-ray from $\sim$GeV to tens of TeV with high energy resolution and sensitivity will significantly improve our knowledge of the *Fermi* bubbles.

---

[1] `http://www.mpe.mpg.de/heg/www/Projects/EROSITA/main.html`

[2] `http://www.rssd.esa.int/index.php?project=Planck`

[3] `http://www.ams02.org`

References

Abdo, A. A., et al. 2009a, ApJS, 183, 46

—. 2009b, Physical Review Letters, 102, 181101

—. 2010a, ApJ, 709, L152

—. 2010b, ApJS, 188, 405

—. 2010c, ApJ, 720, 435

Abdo, A. A., et al. 2010, Phys. Rev. Lett., 104, 101101

Acero, F., et al. 2009, Science, 326, 1080

Aharonian, F., et al. 2009, A&A, 508, 561

Ahn, H. S., et al. 2008, Astropart. Phys., 30, 133

Alexander, D. M., Swinbank, A. M., Smail, I., McDermid, R., & Nesvadba, N. P. H. 2010, MNRAS, 402, 2211

Alvarez-Muñiz, J., Engel, R., & Stanev, T. 2002, ApJ, 572, 185

Antonuccio-Delogu, V., & Silk, J. 2008, MNRAS, 389, 1750

Atwood, W. B., et al. 2009, ApJ, 697, 1071

Baan, W. A., & Irwin, J. A. 1995, ApJ, 446, 602

Baganoff, F. K., et al. 2003, ApJ, 591, 891

Bardeen, J. M., & Petterson, J. A. 1975, ApJ, 195, L65+

Bartko, H., et al. 2009, ApJ, 697, 1741

Bauer, M., Pietsch, W., Trinchieri, G., Breitschwerdt, D., Ehle, M., Freyberg, M. J., & Read, A. M. 2008, A&A, 489, 1029

Beck, R., Brandenburg, A., Moss, D., Shukurov, A., & Sokoloff, D. 1996, ARA&A, 34, 155

Becker, J. K., Biermann, P. L., Dreyer, J., & Kneiske, T. M. 2009, ArXiv e-prints

Berkhuijsen, E. M. 1973, A&A, 24, 143

Bhat, C. L., Issa, M. R., Mayer, C. J., & Wolfendale, A. W. 1985, Nature, 314, 515

Biermann, P. L., Becker, J. K., Caceres, G., Meli, A., Seo, E., & Stanev, T. 2010, ApJ, 710, L53

Bignami, G. F., et al. 1975, Space Science Instrumentation, 1, 245

Biskamp, D. 1986, Physics of Fluids, 29, 1520

Bland-Hawthorn, J., & Cohen, M. 2003a, ApJ, 582, 246

—. 2003b, ApJ, 582, 246

Bland-Hawthorn, J., Veilleux, S., & Cecil, G. 2007, Ap&SS, 311, 87

Blandford, R. D., & Begelman, M. C. 1999, MNRAS, 303, L1

Blandford, R. D., & Payne, D. G. 1982, MNRAS, 199, 883

Blandford, R. D., & Rees, M. J. 1974, MNRAS, 169, 395

Blandford, R. D., & Znajek, R. L. 1977, MNRAS, 179, 433

Bloemen, H. 1989, ARA&A, 27, 469

Blumenthal, G. R., & Gould, R. J. 1970, Reviews of Modern Physics, 42, 237

Bouchet, L., Jourdain, E., Roques, J.-P., Strong, A., Diehl, R., Lebrun, F., & Terrier, R. 2008, ApJ, 679, 1315

Bouchet, L., Strong, A. W., Porter, T. A., Moskalenko, I. V., Jourdain, E., & Roques, J.-P. 2011, ApJ, 739, 29

Braithwaite, J. 2010, MNRAS, 406, 705

Bregman, J. N. 2007, ARA&A, 45, 221

Breitschwerdt, D., McKenzie, J. F., & Voelk, H. J. 1991, A&A, 245, 79

Breitschwerdt, D., & Schmutzler, T. 1994, Nature, 371, 774

Bridle, A. H., & Perley, R. A. 1984, ARA&A, 22, 319

Brown, W. R., Geller, M. J., Kenyon, S. J., & Bromley, B. C. 2009, ApJ, 690, L69

Brunthaler, A., Castangia, P., Tarchi, A., Henkel, C., Reid, M. J., Falcke, H., & Menten, K. M. 2009, A&A, 497, 103

Burrows, D. N., et al. 2011, Nature, 476, 421

Cappelluti, N., et al. 2011, Memorie della Societa Astronomica Italiana Supplementi, 17, 159

Casandjian, J., Grenier, I., & for the Fermi Large Area Telescope Collaboration. 2009, ArXiv e-prints

Cecil, G., Bland-Hawthorn, J., Veilleux, S., & Filippenko, A. V. 2001, ApJ, 555, 338

Chang, J., et al. 2008, Nature, 456, 362

Cheng, K.-S., Chernyshov, D. O., Dogiel, V. A., Ko, C.-M., & Ip, W.-H. 2011, ApJ, 731, L17+

Chernyshov, D. O., Cheng, K. ., Dogiel, V. A., Ko, C. M., Ip, W. ., & Wang, Y. 2011, ArXiv e-prints

Chevalier, R. A., & Clegg, A. W. 1985, Nature, 317, 44

Cholis, I., Dobler, G., Finkbeiner, D. P., Goodenough, L., Slatyer, T. R., & Weiner, N. 2009, ArXiv e-prints

Cholis, I., Dobler, G., Finkbeiner, D. P., Goodenough, L., & Weiner, N. 2009a, Phys. Rev., D80, 123518

Cholis, I., Goodenough, L., & Weiner, N. 2009b, Phys. Rev., D79, 123505

Cox, D. P. 2005, ARA&A, 43, 337

Crocker, R. M. 2011, ArXiv e-prints

Crocker, R. M., Jones, D. I., Aharonian, F., Law, C. J., Melia, F., Oka, T., & Ott, J. 2011a, MNRAS, 413, 763

Crocker, R. M., Jones, D. I., Aharonian, F., Law, C. J., Melia, F., & Ott, J. 2011b, MNRAS, 411, L11

Cuadra, J., Armitage, P. J., & Alexander, R. D. 2008, MNRAS, 388, L64

Dame, T. M., Hartmann, D., & Thaddeus, P. 2001, ApJ, 547, 792

Diehl, R., et al. 2006, Nature, 439, 45

Dijkstra, M., & Loeb, A. 2009, MNRAS, 400, 1109

Dixon, D. D., Hartmann, D. H., Kolaczyk, E. D., Samimi, J., Diehl, R., Kanbach, G., Mayer-Hasselwander, H., & Strong, A. W. 1998, New Astronomy, 3, 539

Dobler, G. 2010, Private communication

Dobler, G., Cholis, I., & Weiner, N. 2011, ArXiv e-prints

Dobler, G., & Finkbeiner, D. P. 2008, ApJ, 680, 1222

Dobler, G., Finkbeiner, D. P., Cholis, I., Slatyer, T., & Weiner, N. 2010, ApJ, 717, 825

Dodds-Eden, K., et al. 2009, ApJ, 698, 676

Drake, J. F., Swisdak, M., Che, H., & Shay, M. A. 2006, Nature, 443, 553

Eckart, A., et al. 2004, A&A, 427, 1

Elmegreen, B. G., & Scalo, J. 2004, ARA&A, 42, 211

Engelbracht, C. W., Rieke, M. J., Rieke, G. H., Kelly, D. M., & Achtermann, J. M. 1998, ApJ, 505, 639

Everett, J. E., Schiller, Q. G., & Zweibel, E. G. 2010, ApJ, 711, 13

Everett, J. E., Zweibel, E. G., Benjamin, R. A., McCammon, D., Rocks, L., & Gallagher, III, J. S. 2008, ApJ, 674, 258

Falceta-Gonçalves, D., Caproni, A., Abraham, Z., Teixeira, D. M., & de Gouveia Dal Pino, E. M. 2010, ApJ, 713, L74

Falcke, H., & Markoff, S. 2000, A&A, 362, 113

Fanaroff, B. L., & Riley, J. M. 1974, MNRAS, 167, 31P

Fichtel, C. E., Hartman, R. C., Kniffen, D. A., Thompson, D. J., Ogelman, H., Ozel, M. E., Tumer, T., & Bignami, G. F. 1975, ApJ, 198, 163

Fields, B. D., Pavlidou, V., & Prodanović, T. 2010, ApJ, 722, L199

Finkbeiner, D. P. 2003, ApJS, 146, 407

Finkbeiner, D. P. 2004a, Astrophys. J., 614, 186

—. 2004b

Gallimore, J. F., Axon, D. J., O'Dea, C. P., Baum, S. A., & Pedlar, A. 2006, AJ, 132, 546

Gebauer, I., & de Boer, W. 2009, ArXiv e-prints

Gehrels, N., & Michelson, P. 1999, Astropart. Phys., 11, 277

Ghez, A. M., Salim, S., Hornstein, S. D., Tanner, A., Lu, J. R., Morris, M., Becklin, E. E., & Duchêne, G. 2005, ApJ, 620, 744

Ghez, A. M., et al. 2008, ApJ, 689, 1044

Gillessen, S., Eisenhauer, F., Trippe, S., Alexander, T., Genzel, R., Martins, F., & Ott, T. 2009, ApJ, 692, 1075

Grenier, I. A., Casandjian, J., & Terrier, R. 2005, Science, 307, 1292

Gualandris, A., & Merritt, D. 2009, ApJ, 705, 361

Guo, F., & Mathews, W. G. 2011a, ArXiv e-prints

—. 2011b, ArXiv e-prints

Guo, F., Mathews, W. G., Dobler, G., & Oh, S. P. 2011a, ArXiv e-prints

Guo, Y., Feng, Z., Yuan, Q., Liu, C., & Hu, H. 2011b, ArXiv e-prints

Harding, J. P., & Abazajian, K. N. 2010, Phys. Rev., D81, 023505

Hartmann, D. H. 1995, ApJ, 447, 646

Haslam, C. G. T., Salter, C. J., Stoffel, H., & Wilson, W. E. 1982a, A&AS, 47, 1

—. 1982b, A&AS, 47, 1

Heesen, V., Beck, R., Krause, M., & Dettmar, R. 2009, A&A, 494, 563

Higdon, J. C., & Lingenfelter, R. E. 2005, ApJ, 628, 738

Hills, J. G. 1975, AJ, 80, 809

—. 1988, Nature, 331, 687

Ho, L. C. 2008, ARA&A, 46, 475

Hooper, D., Finkbeiner, D. P., & Dobler, G. 2007, Phys. Rev., D76, 083012

Innes, D. E., Inhester, B., Axford, W. I., & Wilhelm, K. 1997, Nature, 386, 811

Ipavich, F. M. 1975, ApJ, 196, 107

Irwin, J. A., & Seaquist, E. R. 1988, ApJ, 335, 658

Irwin, J. A., & Sofue, Y. 1992, ApJ, 396, L75

Itoh, C., et al. 2007, A&A, 462, 67

Jokipii, J. R., & Morfill, G. 1987, ApJ, 312, 170

Jonas, J. L., Baart, E. E., & Nicolson, G. D. 1998, MNRAS, 297, 977

Jones, F. C., & Ellison, D. C. 1991, Space Science Reviews, 58, 259

Kaifu, N., Kato, T., & Iguchi, T. 1972, Nature, 238, 105

Kalberla, P. M. W., Burton, W. B., Hartmann, D., Arnal, E. M., Bajaja, E., Morras, R., & Pöppel, W. G. L. 2005, A&A, 440, 775

Kaplinghat, M., Phalen, D. J., & Zurek, K. M. 2009, JCAP, 0912, 010

Karlsson, N., & for the VERITAS collaboration. 2009, ArXiv e-prints

Kino, M., Ito, H., Kawakatu, N., & Nagai, H. 2009, MNRAS, 395, L43

Kniffen, D. A., & Fichtel, C. E. 1981, ApJ, 250, 389

Koyama, K., Maeda, Y., Sonobe, T., Takeshima, T., Tanaka, Y., & Yamauchi, S. 1996, PASJ, 48, 249

Kraushaar, W. L., Clark, G. W., Garmire, G. P., Borken, R., Higbie, P., Leong, V., & Thorsos, T. 1972, ApJ, 177, 341

Kulsrud, R., & Pearce, W. P. 1969, ApJ, 156, 445

Lacki, B. C., Thompson, T. A., Quataert, E., Loeb, A., & Waxman, E. 2010, ArXiv e-prints

Lang, M., Holley-Bockelmann, K., Bogdanovic, T., Amaro-Seoane, P., & Sesana, A. 2011, ArXiv e-prints

Large, M. I., Quigley, M. J. S., & Haslam, C. G. T. 1962, MNRAS, 124, 405

LaRosa, T. N., Nord, M. E., Lazio, T. J. W., & Kassim, N. E. 2004, ApJ, 607, 302

Law, C. J. 2010, ApJ, 708, 474

Lazarian, A., & Opher, M. 2009, ApJ, 703, 8

Lerche, I., & Schlickeiser, R. 1982, A&A, 107, 148

Lin, T., Finkbeiner, D. P., & Dobler, G. 2010, Phys. Rev. D, 82, 023518

Linden, T., Profumo, S., & Anderson, B. 2010, Phys. Rev. D, 82, 063529

Linford, J. D., Taylor, G. B., Romani, R. W., Helmboldt, J. F., Readhead, A. C. S., Reeves, R., & Richards, J. L. 2011, ArXiv e-prints

Lu, Y., Zhang, F., & Yu, Q. 2010, ApJ, 709, 1356

Machida, M., et al. 2009, PASJ, 61, 411

Malyshev, D., Cholis, I., & Gelfand, J. D. 2010, ApJ, 722, 1939

Markoff, S. 2010, Proceedings of the National Academy of Science, 107, 7196

Markoff, S., Bower, G. C., & Falcke, H. 2007, MNRAS, 379, 1519

McCarthy, P. J., van Breugel, W., & Heckman, T. 1987, AJ, 93, 264

McNamara, B. R., & Nulsen, P. E. J. 2007, ARA&A, 45, 117

McNamara, B. R., Nulsen, P. E. J., Wise, M. W., Rafferty, D. A., Carilli, C., Sarazin, C. L., & Blanton, E. L. 2005, Nature, 433, 45

McQuinn, M., & Zaldarriaga, M. 2010, ArXiv e-prints

Mertsch, P., & Sarkar, S. 2011, ArXiv e-prints

Middelberg, E., Agudo, I., Roy, A. L., & Krichbaum, T. P. 2007, MNRAS, 377, 731

Morris, M., Ghez, A. M., & Becklin, E. E. 1999, Advances in Space Research, 23, 959

Morris, M., & Serabyn, E. 1996, ARA&A, 34, 645

Muno, M. P., Baganoff, F. K., Brandt, W. N., Morris, M. R., & Starck, J. 2008, ApJ, 673, 251

Muno, M. P., Baganoff, F. K., Brandt, W. N., Park, S., & Morris, M. R. 2007, ApJ, 656, L69

Muno, M. P., et al. 2003, ApJ, 589, 225

—. 2004, ApJ, 613, 326

Narayan, R., & Yi, I. 1994, ApJ, 428, L13

Narayan, R., Yi, I., & Mahadevan, R. 1995, Nature, 374, 623

Nobukawa, M., et al. 2008, PASJ, 60, 191

Page, L., et al. 2007, Astrophys. J. Suppl., 170, 335

Paumard, T., et al. 2006, ApJ, 643, 1011

Ponti, G., Terrier, R., Goldwurm, A., Belanger, G., & Trap, G. 2010, ApJ, 714, 732

Porter, T. A., Moskalenko, I. V., Strong, A. W., Orlando, E., & Bouchet, L. 2008, ApJ, 682, 400

Porter, T. A., & Strong, A. W. 2005, 4, 77

Prantzos, N., & Diehl, R. 1996, Phys. Rep., 267, 1

Quillen, A. C., Bland-Hawthorn, J., Brookes, M. H., Werner, M. W., Smith, J. D., Stern, D., Keene, J., & Lawrence, C. R. 2006, ApJ, 641, L29

Rees, M. J. 1988, Nature, 333, 523

Revnivtsev, M., Sazonov, S., Churazov, E., Forman, W., Vikhlinin, A., & Sunyaev, R. 2009, Nature, 458, 1142

Revnivtsev, M. G., et al. 2004, A&A, 425, L49

Rosner, R., & Bodo, G. 1996, ApJ, 470, L49+

Scheuer, P. A. G. 1974, MNRAS, 166, 513

Schlegel, D. J., Finkbeiner, D. P., & Davis, M. 1998, Astrophys. J., 500, 525

Schödel, R., et al. 2002, Nature, 419, 694

Scoville, N. Z. 1972, ApJ, 175, L127+

Shakura, N. I., & Sunyaev, R. A. 1973, A&A, 24, 337

Sharp, R. G., & Bland-Hawthorn, J. 2010, ApJ, 711, 818

Smialkowski, A., Wolfendale, A. W., & Zhang, L. 1997, Astroparticle Physics, 7, 21

Snowden, S. L. 2009, Space Sci. Rev., 143, 253

Snowden, S. L., et al. 1997, ApJ, 485, 125

Socrates, A., Davis, S. W., & Ramirez-Ruiz, E. 2008, ApJ, 687, 202

Sofue, Y. 2000a, ApJ, 540, 224

—. 2000b, ApJ, 540, 224

Soltan, A. 1982, MNRAS, 200, 115

Sommer-Larsen, J. 2006, ApJ, 644, L1

Stark, A. A., Martin, C. L., Walsh, W. M., Xiao, K., Lane, A. P., & Walker, C. K. 2004, ApJ, 614, L41

Sternberg, A., & Soker, N. 2008, MNRAS, 389, L13

Strickland, D. K., & Heckman, T. M. 2007, ApJ, 658, 258

Strickland, D. K., & Stevens, I. R. 2000, MNRAS, 314, 511

Strong, A. W. 1984, Advances in Space Research, 3, 87

Strong, A. W., Mayer-Hasselwander, H. A., Bloemen, J. B. G. M., Hermsen, W., & Lebrun, F. 1987, A&AS, 67, 283

Strong, A. W., & Moskalenko, I. V. 1999, 4, 255

Strong, A. W., Moskalenko, I. V., Porter, T. A., Jóhannesson, G., Orlando, E., & Digel, S. W. 2009, ArXiv e-prints

Strong, A. W., Moskalenko, I. V., & Ptuskin, V. S. 2007, Annual Review of Nuclear and Particle Science, 57, 285

Strong, A. W., Porter, T. A., Digel, S. W., Johannesson, G., Martin, P., Moskalenko, I. V., & Murphy, E. J. 2010, ArXiv e-prints

Su, M., Slatyer, T. R., & Finkbeiner, D. P. 2010, ApJ, 724, 1044

Su, M., Yadav, A. P. S., McQuinn, M., Yoo, J., & Zaldarriaga, M. 2011a, ArXiv e-prints

Su, M., Yadav, A. P. S., Shimon, M., & Keating, B. G. 2011b, Phys. Rev. D, 83, 103007

Su, M., Yadav, A. P. S., & Zaldarriaga, M. 2009, Phys. Rev. D, 79, 123002

Sun, X. H., Reich, W., Waelkens, A., & Enßlin, T. A. 2008, A&A, 477, 573

Sunyaev, R., & Churazov, E. 1998, MNRAS, 297, 1279

Sunyaev, R. A., Markevitch, M., & Pavlinsky, M. 1993, ApJ, 407, 606

The Fermi-LAT Collaboration. 2011a, ArXiv e-prints

—. 2011b, ArXiv e-prints

The Fermi LAT Collaboration. 2011, ArXiv e-prints

Thompson, T. A., Quataert, E., & Waxman, E. 2007, ApJ, 654, 219

Thompson, T. A., Quataert, E., Waxman, E., Murray, N., & Martin, C. L. 2006, ApJ, 645, 186

Totani, T. 2006, PASJ, 58, 965

Veilleux, S., Cecil, G., & Bland-Hawthorn, J. 2005, ARA&A, 43, 769

Veilleux, S., Rupke, D. S. N., & Swaters, R. 2009, ApJ, 700, L149

Wang, J., & Hu, C. 2005, ApJ, 630, L125

Weidenspointner, G., et al. 2008, New Astronomy Review, 52, 454

Westmoquette, M. S., Smith, L. J., Gallagher, J. S., Trancho, G., Bastian, N., & Konstantopoulos, I. S. 2009, ApJ, 696, 192

Yadav, A. P. S., Biswas, R., Su, M., & Zaldarriaga, M. 2009, Phys. Rev. D, 79, 123009

Yadav, A. P. S., Su, M., & Zaldarriaga, M. 2010, Phys. Rev. D, 81, 063512

Yu, Q., & Tremaine, S. 2003, ApJ, 599, 1129

Yuan, F., Markoff, S., & Falcke, H. 2002, A&A, 383, 854

Yuan, F., Quataert, E., & Narayan, R. 2003, ApJ, 598, 301

Yusef-Zadeh, F., Hewitt, J. W., & Cotton, W. 2004, ApJS, 155, 421

Yusef-Zadeh, F., & Königl, A. 2004, in Astronomical Society of the Pacific Conference Series, Vol. 322, The Formation and Evolution of Massive Young Star Clusters, ed. H. J. G. L. M. Lamers, L. J. Smith, & A. Nota, 201–+

Yusef-Zadeh, F., et al. 2006, ApJ, 644, 198

Zauderer, B. A., et al. 2011, Nature, 476, 425

Zhang, J., et al. 2009, Phys. Rev., D80, 023007

Zubovas, K., King, A. R., & Nayakshin, S. 2011, ArXiv e-prints

Zubovas, K., & Nayakshin, S. 2012, ArXiv e-prints